TESIS DE LA UNIVERSIDAD DE ZARAGOZA

2023

85

Amelia Domínguez Celorrio

On-surface synthesis of functional organic nanostructures

Director/es

Serrate Donoso, David

Langlais, Véronique

ISSN 2254-7606

Prensas de la Universidad Universidad Zaragoza

ISSN 2254-7606

Universidad Zaragoza
1542

Tesis Doctoral

ON-SURFACE SYNTHESIS OF FUNCTIONAL ORGANIC NANOSTRUCTURES

Autor

Amelia Domínguez Celorrio

Director/es

Serrate Donoso, David
Langlais, Véronique

UNIVERSIDAD DE ZARAGOZA
Escuela de Doctorado

Programa de Doctorado en Física

2022

On-surface synthesis of functional organic nanostructures

Doctoral thesis

Amelia Domínguez-Celorrio

Supervisors:

Dr. David Serrate Donoso
Dr. Véronique Langlais

December 2021

Iré no a donde me envíen mis jefes,
sino a donde me guíen.
Séneca.

Abstract

The improvement of electronic device efficiency is currently based on the miniaturization of existing electronic devices. The manufacturing costs of reducing the size of silicon based circuits below 10 nm is unfeasible for companies. To overcome this limitation, other materials are currently being developed to fabricate equivalent electronic circuits with smaller dimensions. In this context, on-surface synthesis (OSS) is a bottom-up manufacturing technique based on the reaction of molecules to achieve a well-defined organic structure. The atomic precision of OSS allows to create functional organic molecules for molecular electronic devices. Scanning probe microscopy techniques are the most common microscopy techniques used to analyze on-surface synthesized structures. In this thesis, we present the synthesis by OSS and characterization by scanning tunneling microscopy (STM) and spectroscopy (STS) techniques of functional nanostructures. The manganese phthalocyanine (MnPc) synthesized includes in the phthalocyanine ring four diarylethylene moieties (DAE). The DAE moiety is an optically active group. This organo-metallic complex with optically active groups and the Mn in its structure could work as a magneto-optical transducer. We have successfully induced reversible switches with the STM tip between the assigned open and closed configurations of the DAE moiety. The other organic structures synthesized by OSS studied in this thesis are chiral graphene nanoribbons (ch-GNRs) on Ag(001). Combining STM and STS techniques we have studied the evolution of the electronic structure of ch-GNRs depending on their width and length. Finally, we have evaluated the suitability of the ch-GNR/MgO monolayer/Ag(001) system as a molecular spin polarized transistor.

Contents

Abreviations

0D	Zero-dimensional
1D	One-dimensional
2D	Two-dimensional
AC	Alternating current
AFM	Atomic force microscopy
a-GNR	Armchair GNR
BL	Bilayer
BR-STM	Bond resolved STM
BZ	Brillouin zone
CB	Conduction band
CDH	Cyclodehydrogenation/cyclodehydrogenated
ch-GNR	Chiral GNR
CNT	Carbon nanotube
DAE	Diarylethylene
DC	Direct current
DFT	Density functional theory
$\mathbf{E}_F$	Fermi level/energy
EBH	Electron beam heaters
FC	Franck-Condon
FD-STS	Feature detection STS
FER	Field emission resonances
FWHM	Full width at a half maximum
GNR	Graphene nanoribbon

HOMO	Highest occupied molecular orbital
UR	Hindered rotational
HT	Hindered translation
$\mathbf{I}_T$	Tunneling current
IETS	Inelastic electron tunneling spectroscopy
JT-STM	Joule Thomson STM
KPFM	Kelvin probe force microscopy
LDOS	Local density of states
LEED	Low energy electron diffraction
LT-STM	Low temperature STM
LUMO	Lowest unoccupied molecular orbital
ML	Monolayer
MnPc	Manganese phthalocyanine(s)
OSS	On-surface synthesis
PDOS	Projected density of states
PIB	Particle in a box
QMB	Quartz micro balance
SOMO	Singly occupied molecular orbital
SP	Set point
SPM	Scanning probe microscopy/microscope
SP-STM	Spin polarized STM
STM	Scanning tunneling microscopy/microscope
STS	Scanning tunneling spectroscopy
SUMO	Singly unoccupied molecular orbital
TB	Tight binding

TM	Transition metal
UC	Ullmann coupling reaction
UHV	Ultra-high vacuum
UV	Ultra violet
VB	Valence band
z-GNR	Zig-zag GNR

Chapter 1

Introduction

This first chapter starts with a brief review of the most relevant points about electronic devices at the nanoscale. Then, we introduce the manufacturing bottom-up technique used to grow the organic nanostructures this thesis is based on. After that, we present the essential electronic properties of graphene nanoribbons, highlighting their potential as active circuit elements at the single-molecule level.

1.1 Nanoscale electronics

Silicon based integrated circuits have dominated the electronic revolution since their invention in the late 1950s. The growth of this research field is based in the miniaturization of the circuits and the development of new production methods. The miniaturization has been following the predicted Moore's law for several years. We can easily find examples as the change from the first home computers with 1 m^2 in size and 1 KB of memory, to the latest smartphones whose memories easily reach the 256 GB in less than 0.01 m^2. However, it seems that the limit of this technology will be met within the next decade due to technical barriers. Take as an example that, the manufacturing costs to scale down to the range of 10 nm are currently unprofitable for the industry. To overcome this limitation, there are two different approaches. The first one consists on expanding the silicon based integrated circuits into three dimension structures [1]. The second one propose the use of the smallest structures (atoms or molecules) to create equivalent circuits architectures to ones used in the semiconductor industry.

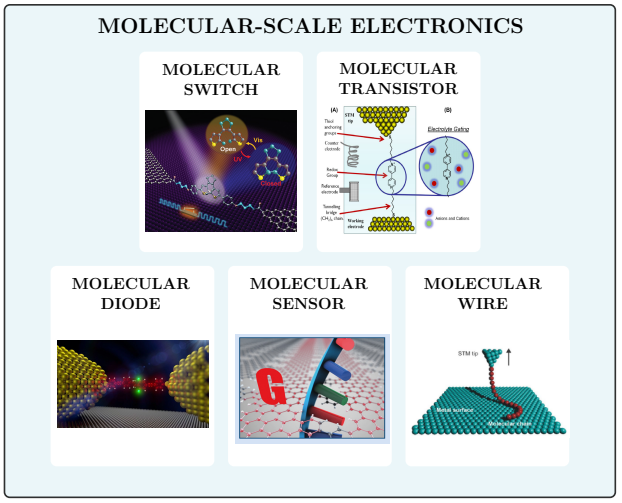

Figure 1.1: Molecular-scale electronics. Molecular switch: graphene-diarylethene-graphene junction from ref. [2]. Molecular transistor: Electrochemical single molecule gating from ref. [3]. Molecular diode: mechanical controllable break junction from ref. [4]. Molecular sensor: nanoporous graphene from ref. [5]. Molecular wire: conjugated chain lifted with the STM tip from ref. [6].

The creation of functional electrical circuits based on the properties of individual or assembled molecules is the basis of molecular-scale electronics. The principal advantages, compared to traditional silicon-based electronic devices, are the reduced size, the diversity that chemical designs gives to molecular structures, and the potential of massive synthesis with low-cost manufacturing processes. The experimental and theoretical progress in electrical circuits based on single molecules includes five types of functional devices: diodes, transistors, switches, wires and sensors. Some reported examples of these devices are included in Figure 1.1.

A significant step forward in the characterization of molecular-scale electronics occurred with the development of scanning probe microscopy (SPM) in 1982. Even though many SPM techniques are still limited to lab experimental level, during the past decades they have produced more and more knowledge about electronic transport at the single-molecule level. Among others, SPM techniques permit to study topics such as optoelectronics, quantum interference, spin transistors and electron-transport.

The research field of molecular devices has also stimulated the synthesis of molecules with specific capabilities at the single-molecule level. In this context, the molecules are required to be atomically perfect and the devices need to be

manufactured in extremely clean conditions. Consequently, readiness level of this technology is currently at the laboratory is currently at the laboratory level. Notwithstanding this fact, in 2013 it was demonstrated the possibility to build a tiny one-bit computer made from carbon nanotubes (CNTs) [7], which later on upgraded to a 16-bit microprocessor in 2019 [8]. This example gives hope to the message that we are currently working at the lab level with promising functional devices.

1.2 On-surface synthesis: A bottom-up strategy for the manufacture of nanodevices

Challenges in the production of nanostructured materials can be overcome by two different strategies which allow one to obtain controlled structures: the top-down and the bottom-up manufacturing strategies. The top-down strategy is referred to the nanostructure fabrication approach where a bulk material is sliced or cut successively until reaching the nanoscale. On the contrary, the bottom-up strategy refers to the building up of a nanostructure from smaller blocks such as atoms or molecules.

The scale limit of top-down approaches depends on the scale limit of the employed tools. Nanolithography-based in solution techniques can nowadays reach a lateral resolution of 10 nm. This precision in the final structure is adequate for certain devices and the short times of lithography techniques currently allow one the series production of semiconductor based micro- and nanochips. On the other hand, building the nanostructure starting with small molecules, allows us to reach atomic scale the precision (below the nm). For this purpose, it is required to chose the correct precursors, a clean environment and a proper supporting substrate to grow the nanostructure.

In this thesis, we will focus on the bottom-up strategy known as on-surface synthesis (OSS). To obtain atomically perfect molecules in a clean environment, OSS has proved to be one of the most promising tools. The OSS is based on the reaction between molecular precursors to grow a structure on top of a supporting surface. The growth of low-dimensional surface-supported organic nanostructures is a field of research that emerged a couple of decades ago [9, 10] and has experienced a significant growth since then. As stated above, in bottom-up approaches the building blocks define the final structure. The flexibility of organic chemistry to synthesized predesigned precursor enables then the growth of different organic nanostructures to meet specific demands. The

design of the molecule precursor is crucial to determine the chemical composition and the geometry of the final structure. As occurs in traditional chemical synthesis, certain functional groups are more capable to react than others. The commonly used dehalogenation and C-C coupling in OSS is known as Ullmann coupling reaction, but we should remark here that although the precursors are similar to the ones used in the solution reaction (aromatic molecules including halogen atoms), the reaction on the surface does not always follow the same mechanism [11]. Figure 1.2 shows schemes and SPM images of successful examples of 0D, 1D and 2D structures growth by OSS to point out how the reactivity, the number and the position of functional groups in the precursor molecules affect the growth directions of the final structure.

The phthalocyanine derivative shown in Figure 1.2 as example of 0D structure, is obtained by cyclotetramerization of eight cyano groups (two -CN per molecule). The position of these -CN groups in adjacent carbons (*orto-* position) is trivial to obtain the 0D structure. If -CN groups were located at *para-* or *meta-* carbons of the aromatic ring in the precursor structure, the cyclotetramerization does not occur, and hence, different structures could be obtained, such as extended networks [12]. To grow 1D chains, the precursor structure should include two reactive points (functional groups) and their position determines the geometry of the ribbon. As example of graphene based 1D chains, in Figure 1.2, we show two precursors whose reactivity on Au(111) surface lead to graphene nanoribbons with different topology, edge and widths [13]. Finally, the example of 2D molecular network shown in Figure 1.2 is obtained after Ullmann coupling reaction of a porphyrin derivative whose structure includes four bromine atoms. In ref. [9] Grill *et al.* demonstrate that the number and position of Br atoms in the porphyrin precursor determines the topology of the structure.

Among all other structures, during the last decades graphene nanoribbons have drawn the attention. This is explained by two reasons: their synthesis directly on a metallic substrate is easy (Ullmann coupling reaction followed by cyclodehydrogenation), and more importantly, the variability of predicted electronic properties of graphene nanoribbons depends on their precise atomic structure, which is only achieved by their OSS.

1.3 Graphene nanoribbons

Graphene nanoribbons (GNRs) can be considered as nanoscale carbon based π-conjugated electronic systems confined by edges. The electronic structure

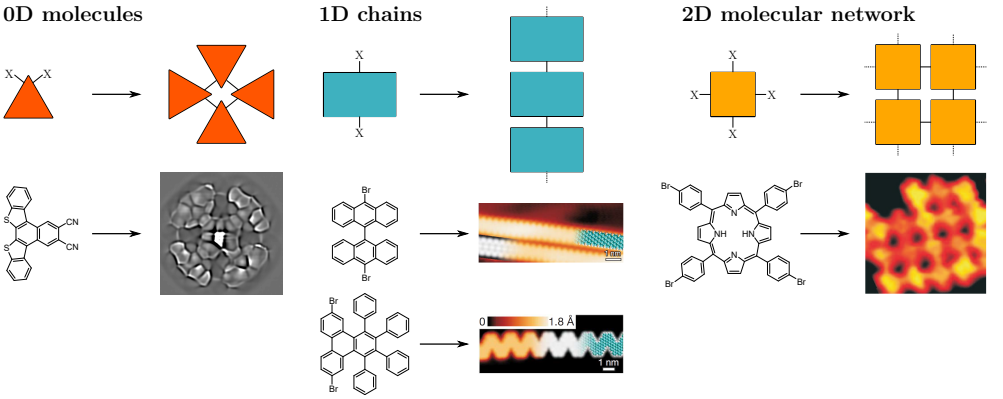

Figure 1.2: Examples of OSS structures. The SPM images correspond to π-MnPc from Chapter 3 (0D molecules), and refs. [13] (1D chains) and [9] (2D molecular network).

and magnetic ground state of GNRs depends on their width and edge shape. In this section, we review the most important properties of GNRs and its dependence on the edge geometry.

1.3.1 Band gap

For a start, we should first define the term band gap to better understand its use throughout the thesis. In solid state physics, a band gap refers to the energy difference between the top of the valence band (VB) and the bottom of the conduction band (CB). For finite crystals, the valence and conduction bands become discrete energy levels and the band gap is then defined as the energy difference between the allowed energies emerging from the VB and CB. For electronic applications, it is important to remark here that in-gap states can be originated at the surface of the crystal, but these states are localized and do not modify the band gap. In a similar way, in the case of a molecule, the band gap is defined as the energy difference between the lowest unoccupied molecular orbital (LUMO) and the highest occupied molecular orbital (HOMO). For GNRs, we consider them as 1D graphene crystals and we will talk about the band gap or the HOMO-LUMO gap to point out the difference between infinitely long GNRs and GNRs of finite size respectively.

When we cut a graphene sheet in straight lines following one of its crystallographic directions ($\vec{z_1}$, $\vec{z_2}$ in Figure 1.3) or perpendicularly to them, we obtain the two basic graphene edge geometries known as armchair and zig-zag edge respectively. The 1D structure confined by a pair of parallel armchair or

zig-zag edges gives rise to armchair graphene nanoribbons (a-GNRs) or zig-zag graphene nanoribbons (z-GNRs) respectively. In Figure 1.3 it can be appreciated that armchair and zig-zag directions form an angle difference of 30°.

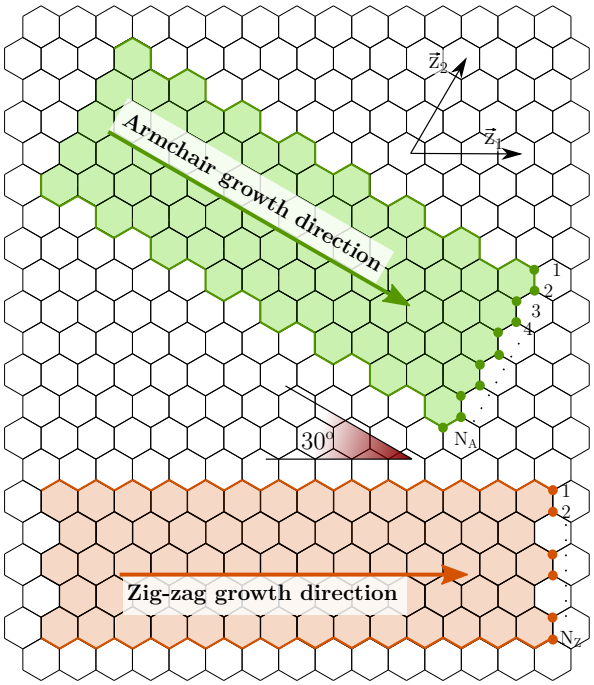

Figure 1.3: Growth directions for GNRs with purely armchair edges (green) and zig-zag edges (orange). N_A and N_Z denote the width of the a-GNRs and z-GNRs respectively.

To better understand the electronic differences between a-GNRs and z-GNRs, we shall start describing the band structure of a graphene sheet. In the tight-binding (TB) approximation, all the graphene carbons are in a honey-comb lattice separated by ≈0.142 nm from the three nearest neighbors, and the Hamiltonian reads

$$\hat{\mathscr{H}} = -t \sum_{\langle i,j \rangle} \hat{c}_j^\dagger \hat{c}_i + \hat{c}_i^\dagger \hat{c}_j \tag{1.1}$$

where t is the hopping integral between nearest-neighbor sites i and j and $\hat{c}_i^\dagger, \hat{c}_j$ refer to electron creation and annihilation operators at sites i and j. For the honey-comb lattice of graphene, for which the unit cell shown in Figure 1.4 has a periodicity of $a_0 = 0.246$ nm and contains two carbon atoms, the

Hamiltonian yields the dispersion

$$E(k) = \pm t\sqrt{3 + 2cos(\sqrt{3}k_x) + 4cos(\sqrt{3}k_x/2)cos(3k_y/2)} \tag{1.2}$$

where $\vec{k} = (k_x, k_y)$ is given in π/a_0 units. The calculated band structure $E(k)$ of graphene is shown in Figure 1.4a. The VB (below Fermi energy) and the CB (above Fermi energy) of graphene are degenerated at the high symmetry points K and K' of the Brillouin zone (BZ), which are so-called Dirac points. At each Dirac point, the electronic bands $E(k)$ show a linear dispersion relation. The real and reciprocal spaces of graphene are shown in Figure 1.4b and 1.4c respectively. The vector $\vec{a}$ ($\vec{z}$) denotes the armchair (zig-zag) growth direction and the longer (shorter) side of the rectangular cell.

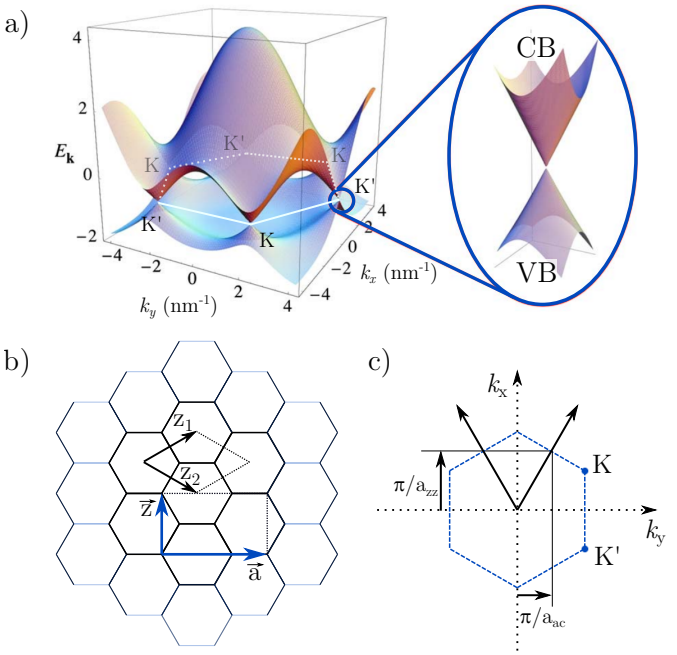

Figure 1.4: a) Graphene electronic band structure calculated and a zoom in of the band structure close to one of the degeneracy points where the valence and conduction bands make contact (Dirac point). b) and c) Unit cells of graphene in real space and in reciprocal space. The vectors $\vec{a}$ ($\vec{z}$) represent armchair (zig-zag) growth directions in real.

The eigenstates of an a-GNR embedded into a virtual graphene lattice as in Figure 1.3 are defined by a linear combination of graphene eigenstates projected onto the lattice sites of the a-GNR. The approximate shape of the

band structure of a-GNRs can then be obtained by projecting the graphene band structure onto the a direction (Figure 1.4c). More precisely, assuming an infinite energy barrier outside the ribbon's edge, the allowed crystal wave vectors have the form

$$\vec{k}^{\pm} = (\pm r\frac{2\pi}{2w}, k_y) \qquad \text{where} \qquad r \,\epsilon\, \{1, ..., N_A\} \tag{1.3}$$

N_A is defined in Figure 1.3 and w represents the width of the a-GNR (in units of a_0) given by

$$w = \frac{\sqrt{3}}{2}(N_A + 1) \tag{1.4}$$

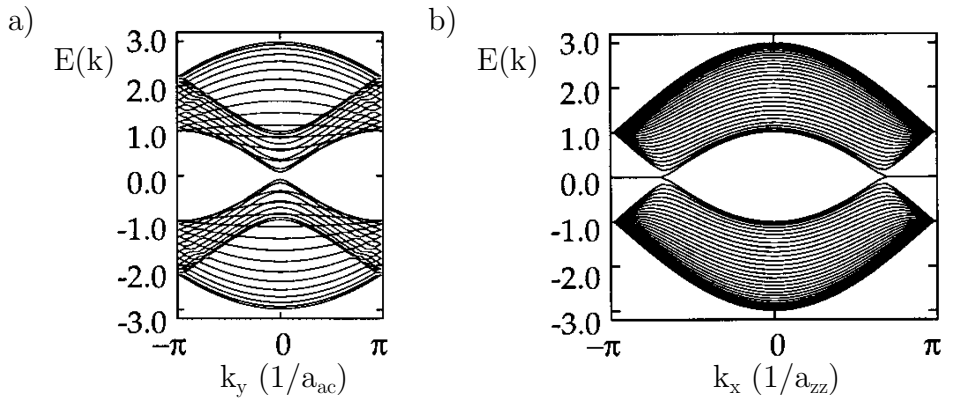

Figure 1.5: a) Calculated band structure of an armchair ribbon of $N_A = 30$. b) Calculated band structure of a zig-zag ribbon of $N_Z = 30$. Adapted from [14].

The electronic band structure of an a-GNR of N_A= 30 is shown in Figure 1.5a [14] and it is obtained by inserting $\vec{k}^{\pm}$ into equation 1.2, which corresponds to cutting the graphene dispersion along N_A parallel lines of constant k_x. The top of the valence band and the bottom of the conduction band are located at $k = 0$. It is important to note that the ribbon width controls whether the system is metallic or insulating. We can distinguish between three families of a-GNR band gaps:

$$\Delta E_{N_A} = \begin{cases} -2t[1 + 2cos(\frac{r_g}{N_A+1}\pi)], & N_A = 3p \qquad r_g = 2p+1, \\ +2t[1 + 2cos(\frac{r_g}{N_A+1}\pi)], & N_A = 3p+1 \quad r_g = 2p+1, \\ 0 \quad , & N_A = 3p+2 \quad r_g = 2p+2 \end{cases} \tag{1.5}$$

where $p \,\epsilon\, \mathbb{N}$, and r_g is the index of the band closest to Fermi level. The TB model predicts for a-GNRs with $N_A = 3p + 2$ to be gapless, since at least one

of the projected cuts crosses the K point, and predicts smaller band gaps for a-GNRs $N_A = 3p$ or $N_A = 3p + 1$ than the values derived directly from the linear dispersion relation of graphene near the Fermi level.

For z-GNRs, the 1-D projected electronic band structure exhibits a degeneration of the highest valence band state and the lowest conduction band state at $k = \pi$ (Figure 1.5b), though the degeneracy is expected to appear at $k = \pm 2\pi/3$ according to the projected band structure of graphene onto z axis (the Γ direction in Figure 1.4c). As seen in Figure 1.5b, the highest valence band and the lowest conduction band approach each other near $k = \pm 2\pi/3$, approaching closer each other as N_Z increases (N_Z is defined in Figure 1.3), reproducing the electronic state at K point in graphene. The degeneracy of the center bands within the region $2\pi/3 \leq k \leq \pi$ ($-2\pi/3 \geq k \geq -\pi$) can be understood as states strongly localized at the zig-zag edge when $k = \pm\pi$ that gradually penetrate into the inner sites, reaching the extended state when $k = \pm 2\pi/3$ [14–17]. These edge states, with a divergent density of states at Fermi level, set the basis for the edge magnetization predicted for z-GNRS [18, 19].

In 1972 Clar et al. proposed a theory to better understand how the π-electrons tend to delocalize in polycylic aromatic carbon based structures [20]. A Clar sextet is the representation of six π-electrons in a six-membered ring, Figure 1.6a shows the benzene ring as example. Instead of drawing two different resonance structures with single and double bonds Clar sextets are represented by a cycle in the ring. With this simpler representation it is possible to predict qualitatively the C-C bond orders in nanographenes and their π-electron delocalization. The Clar formulas are the structures represented with the maximum number of sextets. When the Clar formula includes unpaired electrons (radicals, represented by an outter dot) is known as open-shell structure, whereas those without unpaired electrons are named closed-shell structures. In the case of graphene nanoribbons, Clar's theory reveals how the differences at the edges impact the π-electron distribution along the ribbon. We can obtain these differences by representing the Clar formulas of the ribbon. Infinite graphene has the structure with the maximally dense network of sextets (Figure 1.6b). It is important to note that the sextets represented in Figure 1.6b can be shifted between three equivalent positions and the dense network of sextets is not affected.

The Clar formulas represented in Figure 1.6c-e for a-GNRs illustrate the predicted differences in the band gap for different widths (N_A). For $N_A = 3p$ (c) and $N_A = 3p + 1$ (d), the Clar formulas exclude certain rings from hosting

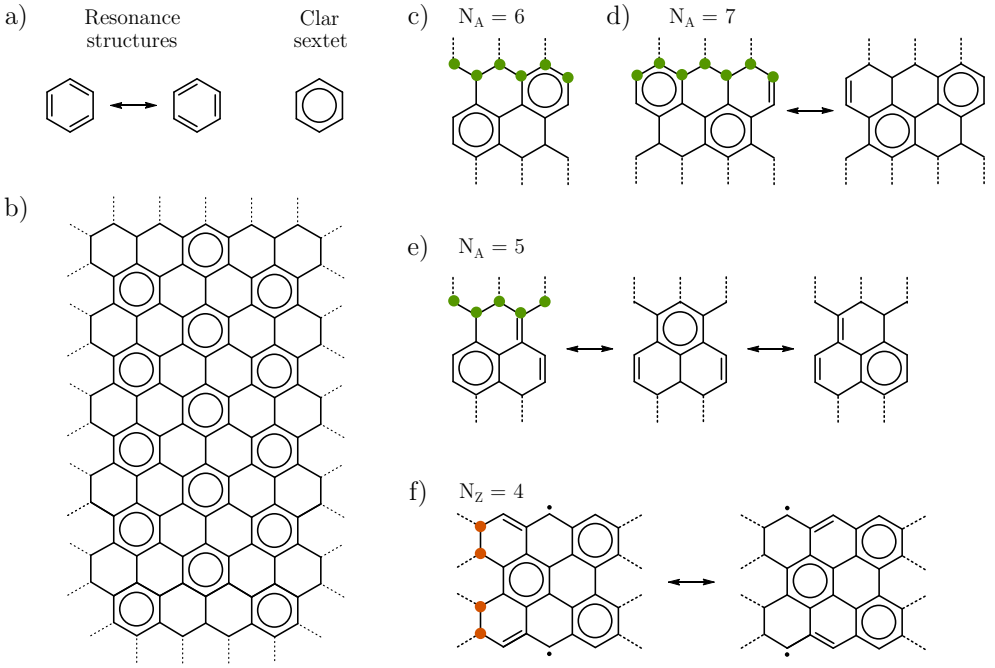

Figure 1.6: a) Representation of the resonance structures of a benzene ring and the Clar sextet representation. b) Graphene represented with maximally dense network of Clar sextets. (c-e) Clar formulas for infinite a-GNRs of $N_A = 3p$ (c), $N_A = 3p + 1$ (d) and $N_A = 3p + 2$ (e). f) Clar formula for infinite z-GNR of $N_Z = 4$ where one unpaired electron every three "zags" is required to maintain the graphene dense network of Clar sextets. Red and green dots denote the N_A and N_Z carbons that give the width of each ribbon.

sextets, which implies significant variations of the C-C bond order along the structures, comparing with the dense of Clar sextets in graphene. These bond differences are considered in TB model, causing the gap opening in eq. 1.5. In the Clar formulas for a-GNR of $N_A = 3p + 2$ (Figure 1.6e), the Clar sextets are propagated through the structure just like in graphene, in agreement with the gapless a-GNR structure predicted in the TB model.

For z-GNRs, the Clar formulas provide an explanation for the localized states at the zig-zag edge calculated by TB. As shown in Figure 1.6f for z-GNR of $N_Z = 4$, an unpaired electron (represented with a black dot) is required every three graphene primitive lattice vectors along the ribbon axis (commonly referred as "zags") to recover the π-electron delocalization of infinite graphene. The presence of these unpaired electrons at the zig-zag edge, fluctuating among different resonance structures, allows us to better understand the predicted edge magnetization in z-GNRs and in other open-shell structures (see section

6.1 [18, 19].

1.3.2 Edge magnetization

In sharp contrast with 2D graphene or a-GNRs, in z-GNRs exists a large density of states at the Fermi level localized in the zig-zag edges, which is responsible for the appearance of magnetic moments in the structure. The localized edge states decay quickly towards the interior of the ribbon, but in narrower z-GNRs a sizable overlap is expected, and consequently magnetic interactions between opposite edges as well. *Ab*-initio calculations including spin degrees of freedom predict, for the ground state of these interacting edge magnetizations [21], a ferromagnetic alignment of unpaired electrons in the same edge and antiferromagnetic alignment between opposite edges. Another alternative to treat the magnetism of zig-zag graphene edges is by means of a mean-field approach using an extension of the TB model that includes the electron-electron correlations [16, 18, 22]. The Hamiltonian of eq. 1.1 becomes then

$$\hat{\mathscr{H}} = -t \sum_{\langle i,j\rangle,\sigma} (\hat{c}^{\dagger}_{j\sigma}\hat{c}_{i\sigma} + \hat{c}^{\dagger}_{i\sigma}\hat{c}_{j\sigma}) + U \sum_{i} \hat{n}_{i\uparrow}\hat{n}_{i\downarrow} \tag{1.6}$$

which includes the electron spin ($\sigma \in \{\uparrow, \downarrow\}$), the spin-resolved electron density at a site i ($\hat{n}_{i\sigma} = \hat{c}^{\dagger}_{i\sigma}\hat{c}_{i\sigma}$) and the energy penalty due to on-site Coulomb repulsion (U). Coulomb repulsion plays a primary role in the energetic of wave functions with very small spatial extent. The strongly localized nature of zig-zag edge states [14, 23] makes them prone to magnetic instabilities against electron-electron correlations ($U \neq 0$). This Hamiltonian in eq. 1.6 is commonly referred to as Hubbard Hamiltonian [24]. As occurs with t, U is a model parameter that requires the fitting to experimental results to pull out its value.

1.3.3 Chiral graphene nanoribbons

Up to now, we have discussed about GNRs which grow following the 0° or 30° direction respect graphene crystallographic direction (Figure 1.3). Chiral graphene nanoribbons (ch-GNRs) are defined as graphene ribbons whose growth direction do not follow the armchair or zig-zag growth direction. There are multiple notations to describe them, for instance the angle θ formed by their axial direction with respect to the crystallographic graphene direction ($0 < \theta < 30°$), or defining the combination of armchair and zigzag edges that

results parallel to in the chiral edge. In this thesis we use a notation consisting in three numbers (n, m, c). Defining the chiral translational vector $(\vec{C}_{n,m})$ as

$$\vec{C}_{n,m} = n \cdot \vec{z_1} + m \cdot \vec{z_2} \equiv (n, m) \tag{1.7}$$

n and m represent the number of lattice vectors, and c corresponds to the number of carbon atoms across the ribbon's width (similarly to N_A for a-GNRs). In Figure 1.7 there are two examples of ch-GNR to explain how (n, m, c) are assigned to each structure.

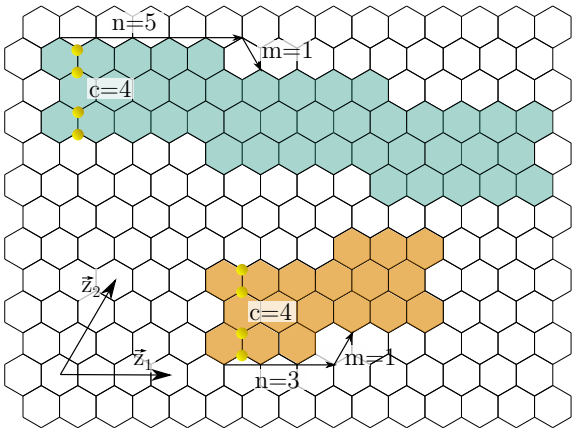

Figure 1.7: ch-GNRs with different growth directions. Their (n, m, c) notation is (5,1,4)-GNR for blue GNR, and (3,1,4)-GNR for brownish yellow GNR.

The length of a ribbon is commonly defined as the number of 1D unit cells. In the case of ch-GNRs, the length of this unit cell in a_0 units ($a_0 = 0.246$ nm) is given by

$$a = (\overline{n, m}) = a_0\sqrt{n^2 + nm + m^2} \tag{1.8}$$

The interest of ch-GNRs resides in the fact that from the theoretical point of view, the combination of armchair and zig-zag like edges, give rise to a combination of the properties of a-GNRs and z-GNRs. In Figure 1.8 we show the evolution of the TB band structure without electron-electron interactions of graphene nanoribbons with analogous $c = 24$, when its chirality changes from zig-zag (1,0) to armchair (1,1) (figure adapted from ref. [18]). The z-GNR band structure changes from the zero-energy flat band corresponding to the density of states at the edge, to the a-GNR band structure with no electronic states localized at the edges. The intermediate ch-GNR band structures are obtained by continuous rotation of the band structure of graphene. For ch-GNRs with edge orientations close to zig-zag direction, the band structure shows the flat

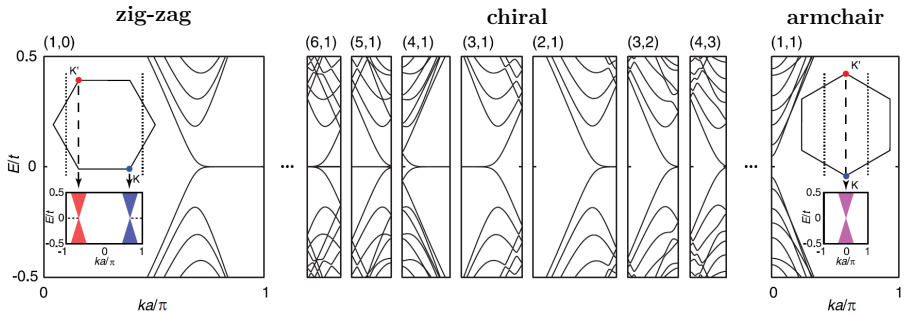

Figure 1.8: Evolution of the TB band structures of GNRs of width $c = 24$, upon zig-zag (1,0) to armchair (1,1) edge direction via the series of intermediate chiral configurations (n, m). The insets illustrate the projection of points K and K' of the 2D BZ of ideal graphene onto the 1D band structures of z-GNRs and a-GNRs. Taken from ref. [18].

edge-state band covering the whole Brillouin-zone, while for ch-GNRs with edge orientations close to armchair direction the edge-states are suppressed [18]. ch-GNR are predicted to have a width modulated semiconducting band gap and localized metallic states at the zig-zag edges that, in addition, are foreseeable candidates to host net magnetic moment. [14, 15, 18, 22, 25–27].

As the chiral edges are less reactive than the zig-zag edges, the on-surface synthesis of ch-GNRs is significantly simpler, and this advantage has stimulated their synthesis and characterization over z-GNRs. In Chapters 4, 5 and 6 we will focus in the synthesis and electronic characterization of two types of ch-GNR with $n = 3$, $m = 1$ and widths $c = 4$ and $c = 8$, on Ag(001) and MgO/Ag(001) as supporting substrates.

Chapter 2

Experimental methods

This chapter gives a brief outlook of the main experimental details and techniques used in this thesis. The chapter begins with a short introduction to the scanning tunneling microscopy, some of its operating modes and their practical implementation. Next, we show the laboratory set-up, describing in detail the parts that have played an important role during this thesis. Finally, we present a summary of the sample preparation and tip functionalization methods.

2.1 Scanning tunneling microscopy and spectroscopy

The development of scanning tunneling microscopy (STM) was presented in 1981 by G. Binning, Ch. Gerber and E. Weibel as a microscopy technique based on a physical probe to scan and analyse surfaces [28]. The potential of this technique was confirmed when Binning and Rohrer obtained the first 7×7 reconstruction of Si(111) resolved in real space by STM [29]. This contribution was awarded with the Nobel Prize in Physics in 1986 and prompted the development of scanning probe methods to observe locally physical properties of the surfaces, down to the atomic scale.

2.1.1 Quantum electron tunneling effect

The working principle of STM is based on the tunneling effect produced when a voltage is applied between a sharp tip (the probe) and the sample (the studied surface). Contrary to the expectation from classical Physics, a charge current arises due to the electrons that pass through the potential barrier before the

tip and the sample come into direct contact.

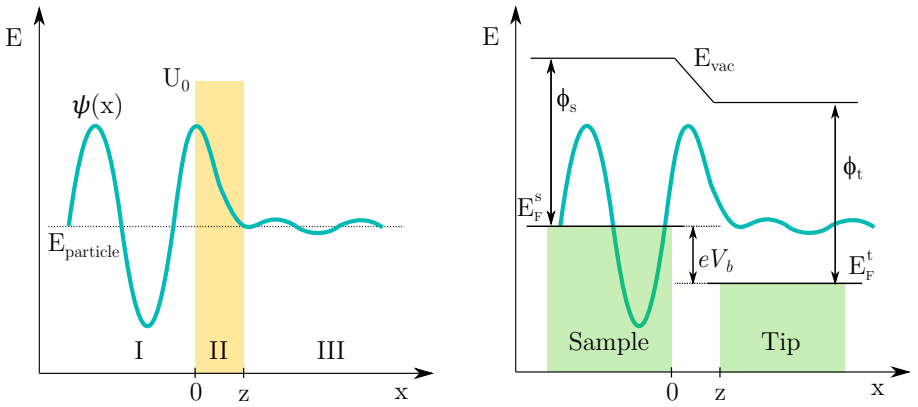

Figure 2.1: a) Schematic one-dimensional model of a potential barrier of width z and height U_0 in region II. b) Schematic representation of the trapezoidal tunnel barrier in a STM when a negative bias is applied to the sample respect to the tip, electrons from occupied sample states tunnel into unoccupied tip states.

Figure 2.1a shows the quantum mechanical behaviour of an electron in 1D that penetrates an energy barrier (region II) which is classically forbidden by the energy conservation principle. The state of the electron with energy E, is then defined by a wave function $\psi(x)$ that satisfies the time-independent Schrödinger equation given by

$$\left(-\frac{\hbar^2}{2m_e}\frac{d^2}{dx^2} + U(x)\right)\psi(x) = E\psi(x) \tag{2.1}$$

where $\hbar$ is the reduced Planck constant and m_e is the electron mass.

The STM system can be described as two ideal metal electrodes with their electron states filled up to the Fermi energy (E_F) and separated by a small gap (z). A voltage V_b applied to one of them shifts the tip and sample E_F by eV_b giving a trapezoidal tunnel barrier for the electrons (Figure 2.1b). By solving the eq. 2.1 with physical constrains imposed at the I-II and II-III boundaries, one obtains that for an electron in the sample ($x = 0$) at E_F, represented by its wave function $\psi(x)$, the probability to find it at position x is

$$|\,\psi(x)\,|^2 = |\,\psi(0)\,|^2\, e^{-2\kappa x} \quad \text{with} \quad \kappa = \sqrt{\frac{m_e}{\hbar^2}\left(\frac{\phi_t + \phi_s}{2} - eV_b\right)} \tag{2.2}$$

where ϕ_t and ϕ_s represent the work functions from the tip and the sample respectively. The tunneling current (I_T) is defined as the sum of the probabilities of all electronic states available within the tunneling window eV_b (Figure

2.1b). At zero temperature, the tunneling current over all occupied electronic states μ of the sample can then be expressed as

$$I_T(z, V_b) \propto e^{-2\kappa z} \sum_{E_\mu = E_F - eV_b}^{E_F} \mid \psi_\mu(0) \mid^2 \tag{2.3}$$

It follows from eq. 2.3 that tunneling current depends exponentially on the distance between the tip and the sample (z). For typical work function values in metals (ϕ = 4 - 5 eV), κ has a value of 1.0 Å^{-1}, which gives a decay of an order of magnitude in the tunneling current when z is increased by 1 Å. This explains the high vertical resolution of the STM, even though the 1D model is a drastic oversimplification.

The local density of states (LDOS) is the central quantity in any quantum mechanical problem. It is defined as the number of electrons per unit energy interval at a specific position

$$n_{z,E} = \sum \mid \psi_\mu(z) \mid^2 \delta(E_\mu - E) \tag{2.4}$$

and with the assumption that $n(z, E)$ is constant in the range of eV, which would be valid for small eV_b (Figure 2.1b), the tunneling current in eq. 2.3 from the tip to the sample can be expressed as

$$I_T(z, V) \propto e^{-2\kappa z} n(x = 0, E_F) eV \tag{2.5}$$

The tunneling current depends linearly on the LDOS of the sample and the applied voltage. At low bias voltage ($eV_b << \phi_t, \phi_s$) the STM probes the LDOS of the surface rather than its topography. As already mentioned, this is the simplest model for the STM system, where the contribution of the electronic structure of the tip has been neglected. To introduce the tip contribution, Bardeen established an approximation [30, 31] taking into account three considerations that are still accepted in many theoretical approaches for the interpretation of STM images:

1. The electron-electron correlations can be ignored.

2. The tip and the sample should be treated as separated subsystems, whose occupation probabilities are constant and independent of each other.

3. The tip and the sample are electrochemically stable.

This considerations reduce the calculation of the tunneling probability to the knowledge of the so-called Bardeen tunneling matrix, which is a representation of the coupling across the vacuum between all the eigenstates of the tip and the sample. Tersoff and Hamman [32, 33] proved that this matrix can be considered energy independent if the tip is modeled as a s-wave function. Assuming the atomically sharp shape of the tip, only the last atom contributes to the tunneling process and modelling it by a spherical s-like orbital, the wave function of the tip can then be overlooked. In the limit of low bias and zero temperature, the Tersoff and Hamman theory is simplified in the following expression:

$$I_T(r, eV) = \frac{16\pi^3 C^2 \hbar^3 e}{\kappa^2 m_e^2} n_t \int_0^{eV} n_s(\vec{r}, \epsilon) d\epsilon \tag{2.6}$$

where C is a constant, κ is defined as in eq. 2.2, $\vec{r}$ is the center of the outermost atom of the tip and $n_s(\vec{r}, \epsilon)$ is the density of states of the sample in the proximity of the Fermi level.

2.1.2 Imaging

As shown in the last section, the tunneling current depends exponentially on the tip-sample distance. It is important to mention now that in a STM, the tip is attached to a piezo-driver, which consists in three perpendicular piezoelectric transducers allowing to scan the surface (x and y piezos) and adjust the tip-sample distance (z piezo). The movement of the tip, in the sub-Angström scale, is then controlled by the expansion or reduction of the piezoelectric transducer upon the application of high voltages to the corresponding electrodes.

Figure 2.2 shows schematically how the STM operates when imaging a surface. The tunneling current is constantly monitored by an electrical feedback loop that adjusts the tip-sample distance to maintain a constant current value when the tip scans the surface (constant current operation mode). If the feedback loop system is disabled, the tip-sample distance is fixed (constant height operation mode) and, an image can be obtained scanning the surface and measuring the current variations. Figure 2.3 shows schematically the two imaging modes. Monitoring $\Delta z(x, y)$ or $\Delta I_T(x, y)$ we can obtain a map of the LDOS of the surface. As shown by eqs. 2.5 and 2.6, the constant height operation mode provides a quantitative representation of the sample LDOS with larger lateral resolution.

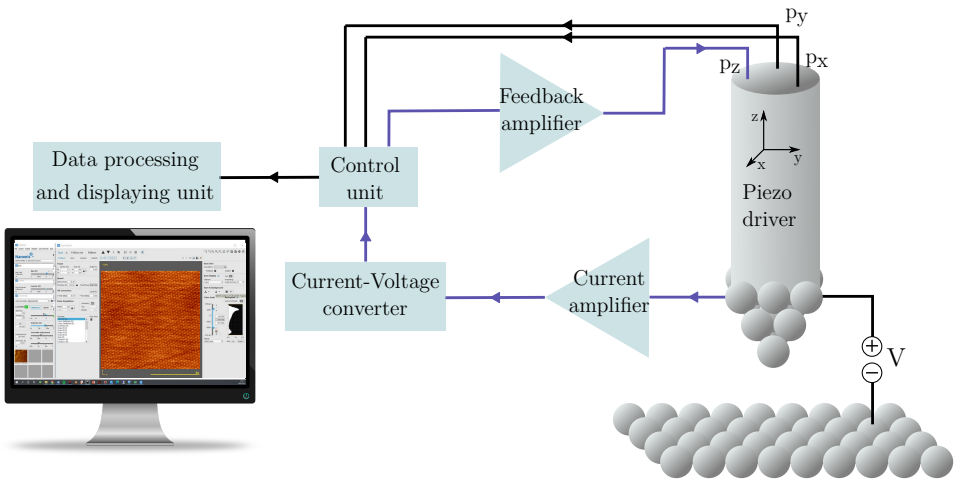

Figure 2.2: Scheme of the common design of a STM.

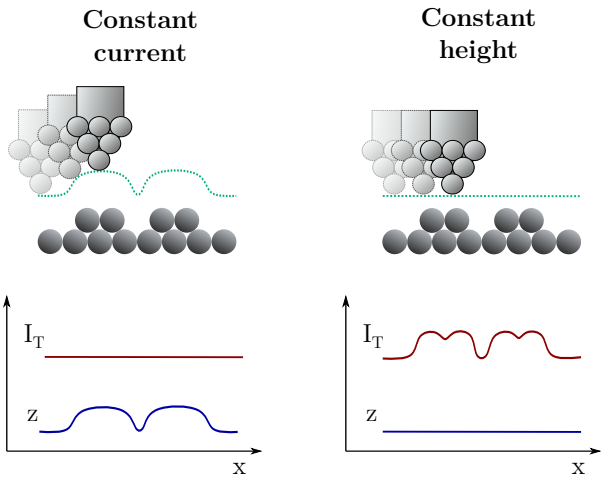

Figure 2.3: STM can be operated in constant current mode by adjusting the tip-sample distance (z) for constant I_T, or in constant height mode fixing z and measuring tunneling current (I_T) variations, which typically portrays highly resolved structural information in the case of chemically homogeneous surfaces.

2.1.3 Scanning tunneling spectroscopy

The scanning tunneling spectroscopy (STS) technique exploits the STM capability of recording spectroscopic data with lateral atomic resolution. The STS consist in measuring the tunneling differential conductance as a function of the applied bias voltage. For very low temperatures with k_bT much lesser than the width of the spectroscopic characteristics of interest, and a featureless tip density of states, the expression for the differential conductance within the Tersoff Hamann model can be simplified as

$$\left.\frac{\partial I_T}{\partial V}\right|_V \propto n_t n_s(\vec{r_0}, eV) \tag{2.7}$$

where $\vec{r_0}$ is the position of the tip apex. The mathematical derivation of eq. 2.7 is not included here (see for example [34]), but from eq. 2.6 it is easy to deduce that the derivative of the integral expression of I_T up to the limit eV, is exactly the integrand evaluated at the value of the limit. The exponential dependence explicit in eq. 2.5 is adsorbed here by the the decay of the sample density of states, n_s, into the vacuum at a distance set by $|r_0|$.

The common procedure to carry out STS measurements is in constant height conditions, and starts opening the feedback loop with the tip placed on top of the point of interest with certain voltage V and current I_T (set point, SP). It follows from eq. 2.7 that the changes in the slope of experimental $I-V$ curves give information about the LDOS of the sample at a given voltage eV. The standard way to express the relationship between the LDOS of the sample (ρ_s) and the differential conductance is

$$\rho_s(eV) \propto \frac{dI}{dV} \tag{2.8}$$

For constant current STS, the tip is positioned over the point of interest with certain current I_T as SP. Then the voltage is varied under feedback control and the tip moves vertically to maintain the I_T value constant with the new voltage applied. When the voltage increases the tip retracts away, and when the voltage decreases the tip approaches to the surface. The rate of tip motion is proportional to the tunneling probability, and the observed anomalies (peaks) in the recorded $\mathrm{d}z/\mathrm{d}V$ spectrum are associated to electronic states of the surface, giving rise to twin anomalies in the simultaneously recorded $\mathrm{d}I/\mathrm{d}V$. This method is useful to distinguish spectroscopic features in the high bias range, where bias values are comparable to the surface work function and most of the approximations in section 2.1.1 do not hold.

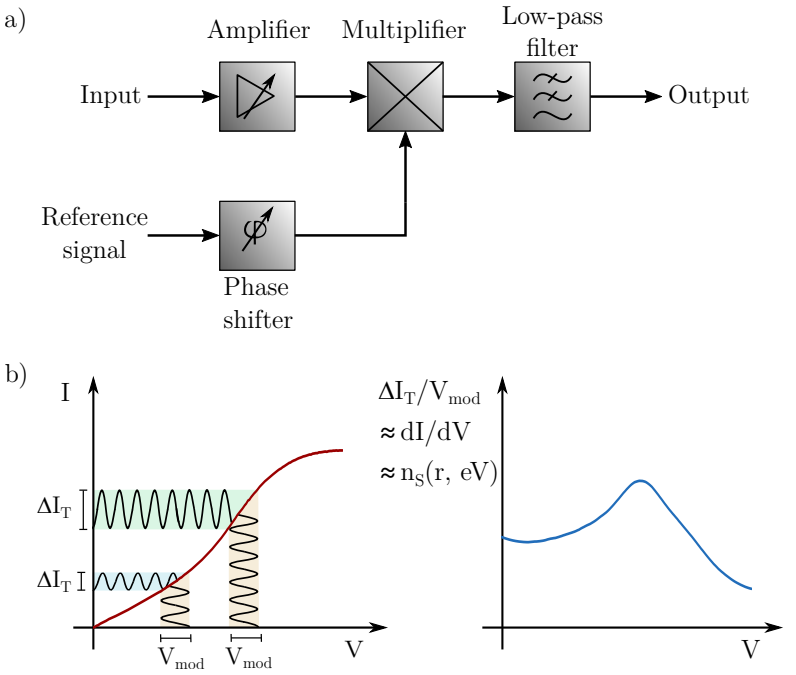

Figure 2.4: a) Schematic representation of a lock-in amplifier. b) Determination of $\mathrm{d}I/\mathrm{d}V$ with lock-in technique and corresponding experimental $\mathrm{d}I/\mathrm{d}V$ spectrum.

To improve the detected derivative I_T signal-to-noise over the simple numerical differentiation technique, we use the lock-in amplifier technique with a phase-sensitive detection method. The principle of this technique is based on the addition to the DC bias signal an AC reference signal, with known frequency and phase, that allows the lock-in to discern true physical responses of the differential conductance from the noise in the output. This technique is schematized in Figure 2.4. Only the contribution of the input signal that has the same frequency as the reference is deconvoluted. The uncorrelated phases are filtered out by the low-pass filter, and then, the output signal is linear to the modulation amplitude response of the tunneling current, extracting in this way the $\mathrm{d}I/\mathrm{d}V$ slope by electronic means. This allows us to measure the LDOS of the surface with great precision.

A combination of STS and the surface scanning is also possible and useful to obtain the distribution of the LDOS with high spatial resolution. The procedure consists of scanning the area applying a modulated constant voltage while monitoring the $\mathrm{d}I/\mathrm{d}V$ (in open feedback conditions) to get a quantitative picture of the LDOS. The LDOS can also be accessed in closed feedback conditions, but in this case the height variations due to the topography profiling can

introduce artefacts. Nevertheless, closed feedback $\mathrm{d}I/\mathrm{d}V$ mapping is a quick and broadly applied technique to find patterns and spatial modulations of the investigated wave functions, or even qualitative images of the LDOS when the spectroscopic features dominate over the topographic crosstalk. For both mapping modes it is important to have a detailed knowledge of the spectrum before choosing the imaging voltage, otherwise the map just reflects background features instead of features of the electronic states [35].

2.2 Atomic manipulation

The STM is considered as an engineering tool at the atomic scale since Eigler and Schweizer published in 1990 the writing of IBM letters on nickel(110) surface sliding Xenon atoms with the STM tip [36]. Since then, the controlled movement of atoms, clusters of atoms and molecules has made possible the investigation of artificial structures such as quantum corrals [37], Lieb lattices [38] and magnetic structures [39, 40] with high impact in condensed matter Physics.

To manipulate the matter down to the atomic scale it is important to understand the interactions present in the tunnel junction of the STM. These interactions are represented in Figure 2.5a and include the forces between tip and surface, the electrical field between tip and surface and the electron tunneling current. Using one, or a combination of them, it is possible to induce designated modifications of position or state in atoms or molecules [41]. Depending on the displacement direction of the particle at the beginning of the manipulation event (vertical or parallel to the surface), we can distinguish between vertical manipulation and lateral manipulation.

In a vertical manipulation the particle is picked up by the tip, which usually changes the properties of the tip with favourable consequences for imaging as will be discussed in section 2.6. In contrast, during the lateral atomic manipulation the particle is moved along the surface without losing the contact. The three basic lateral manipulation modes are shown schematically in Figure 2.5b. The difference between these modes lies in the interaction produced between the tip and the particle. In the pulling mode, the attractive interaction with enough in-plane force projection as to drag the adsorbate, is achieved once the tip goes over the maximum corrugation, producing the jump of the molecule below the tip and then the abrupt retraction of the tip. In the pushing mode the particle jumps due to repulsive forces before the tip reaches its maximum, causing the immediate approach of the tip to the surface (in closed feedback

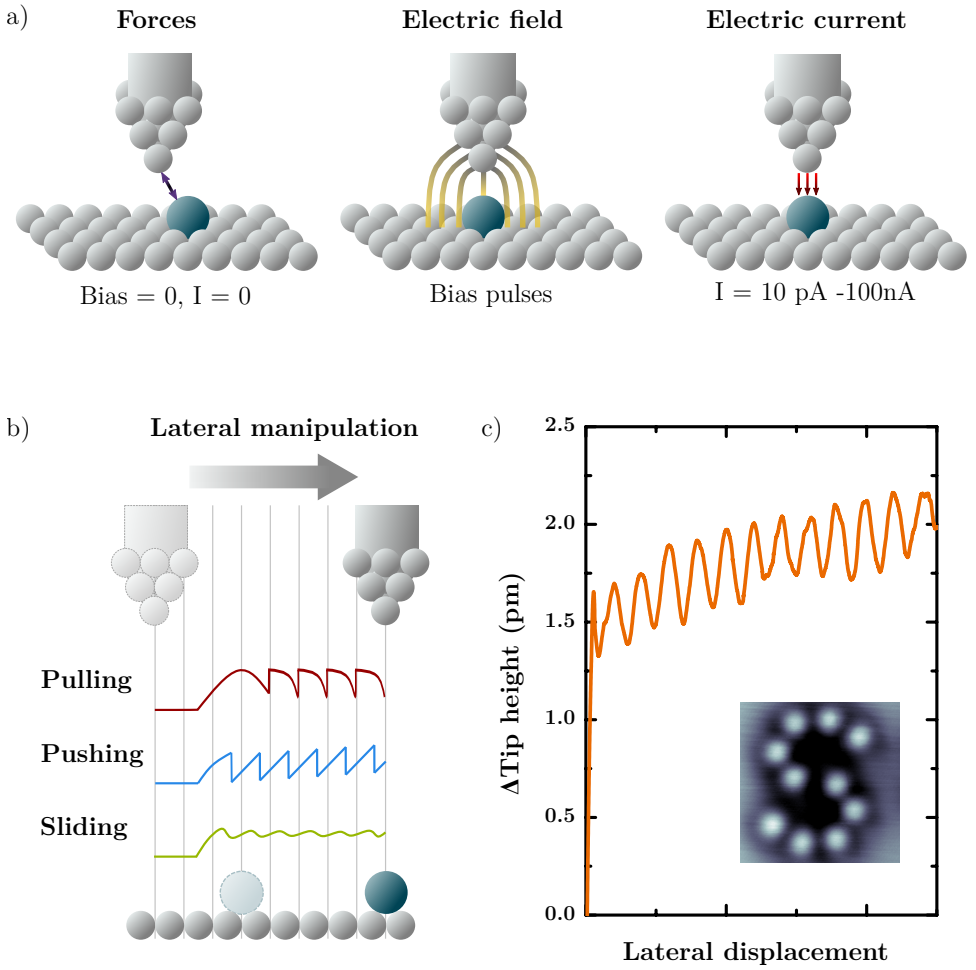

Figure 2.5: a) Interactions present in the tunnel junction of the STM which provide modifications on the surfaces. b) Traces of lateral manipulation obtained in different manipulation modes. c) Trace manipulation of a Br atom on Ag(001). The STM image shows an "S" created by the lateral manipulation of 10 Br atoms on Ag(001) (0.5 V, 100 pA, 3×3 nm^2).

conditions). The sliding mode is observed when the interaction between the tip and the particle is so strong that the particle scans the corrugation of the substrate, and moves simultaneously with the tip [42]. An example of an experimental manipulation trace of a Br atom on Ag(001) is included in Figure 2.5 with a STM image of a "S" written atom by atom with 10 bromine atoms.

The lateral atomic manipulation can be performed in constant current or in constant height mode, and the corrugation profiles (manipulation traces) are then obtained in either I_T or z channels. Successful lateral manipulation of small molecules such as CO or C_2H_2 has been performed at low temperatures [43, 44] using the sliding mode. The lower surface mobility of large molecules difficulties their manipulation and reported experimental evidences suggest the advantages of performing their manipulation in constant height mode [45–48]. Here, the tip is approached to the molecule fixing an initial distance closer than the imaging distance (to enhance the tip-molecule forces), and when the tip is displaced parallel to the surface the molecule moves also to the desired position.

For the development of this thesis, we have performed lateral atomic manipulation of manganese phthalocyanines (Chapter 3) and graphene nanoribbons (Chapter 5). The parameters and the modes employed (constant current or constant height) depend on the molecule and the aim of the displacement. Thus, all the details are included in their respective chapters.

2.3 Work function and electric polarization of surfaces

The work function is classically described as the amount of energy required to remove an electron away from the solid to a distance larger than the lattice parameter. Wigner and Bardeen [49] proposed that the work function is given by

$$\phi = -\mu + D \tag{2.9}$$

where the first term μ is the chemical potential of the electrons, and D corresponds to the energy required to penetrate the dipole barrier at the surface. D energy is formed by the redistribution of the electron density when the crystalline lattice terminates abruptly, and depends on the position of ion cores, meaning that the work function of an element is different depending on the surface plane studied. The origin of the work function defined with eq. 2.9 is included in detail in ref. [50]. However, in the case of a surface with an

ultra-thin coating or with individual adsorbates, the calculation of the work function requires more elaborated theoretical approaches [51].

When an ultra-thin film is deposited on a metal, the work function of the metal is strongly shifted. The induced work function shifts are attributed to three different mechanisms: the charge transfer between the deposited film and the substrate ($\Delta\phi^{CT}$), the surface relaxation by interface bond formation ($\Delta\phi^{SR}$) and the electrostatic compression effect ($\Delta\phi^{EC}$) which is also called as pillow-effect, because it arises from the Pauli repulsion between the adsorbate's and substrate's electron densities when they are brought in close proximity. Depending on the nature of the deposited material, any one of these mechanisms can dominate the work function shifts. The compression of the metal electronic density upon film deposition is the main mechanism governing the strong reduction of the metal work function upon deposition of highly ionic materials such as NaCl or MgO [52, 53].

In a similar way, when a molecule is adsorbed on a surface, its electronic properties change depending on the charge transfer and binding energies at the molecule/surface interface. As mentioned above, the work function value is affected by all these parameters. Considering the work function of a substrate, the orbital level alignment of the molecule respect to the Fermi level can be modify, which renders the molecule to be semiconducting or metallic depending on the selected supporting surface [54–56]. In Chapters 4 and 5 we study and discuss the differences in the electronic properties of chiral graphene nanoribbons adsorbed on Ag(001) and on a monoatomic layer of MgO.

2.3.1 Local work function measurements

Photoemission spectroscopy and low-energy electron microscopy are usual techniques to directly measure the work function of a surface. SPM techniques such as Kelvin Probe Force Microscopy (KPFM), the recording of *I(z)* curves, or measuring Field Emission Resonances (FER) are alternative methods with lateral resolution below the nanometer scale, which allow us to obtain information about the local work function. These methods give a work function value which is influenced by both, the work function of the tip ϕ_t and the work function of the sample ϕ_s. Since the value of ϕ_t is unknown but assumed to be constant for a given tip, with these techniques we obtain the value of the local work function shifts ($\Delta\phi$) with large spatial resolution.

When the STM is operated in the field emission regime at voltage bias values comparable to the work function energy [57], electronic standing waves

are formed in the vacuum gap between the tip and the sample. These states manifest as resonances of the differential conductance $\mathrm{d}I/\mathrm{d}V$ whose energy spacing depends on the local work function. This resonances are the so-called field emission resonances (FER). Assuming a 1D potential between tip and sample, the FER energies are given by [58, 59]

$$eV_n = \phi + \left(\frac{3\pi\hbar e}{2\sqrt{2m}}\right)^{2/3} E^{2/3} n^{2/3} \tag{2.10}$$

where n is the resonance index, V_n is the voltage at which the n^{th} maximum in the constant current conductance (or $\mathrm{d}z/\mathrm{d}V$) occurs while retracting the tip, e is the electron charge, ϕ is the work function of the surface and E is the electric field normal to the surface.

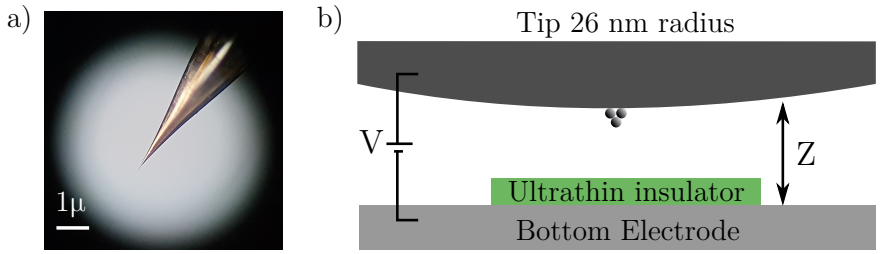

Figure 2.6: a) STM tip observed by an optical microscope. b) Sketch of the STM tunnel junction preserving the real scale of the tip curvature radius (typically obtained by electrochemically etching of a metal wire) and tip-sample distance (z).

This approximation might seem at odds with the customary idea that the STM tip is atomically sharp. Let us remind that STM high lateral resolution comes from the tunneling current, which is dominated by the last atom of the tip apex (with position r_0 in eq. 2.7). But at the nanoscale, the STM tip shape is not a pyramid of atoms. Instead, a more realistic sketch of a STM tip is shown in Figure 2.6b, where it becomes clear that the 1D model of parallel plate capacitor is appropriate to calculate the electric field E in the junction. When a voltage gradient V is applied between the tip and the sample, the electric field is given by the expression

$$E = \frac{V}{z} = \frac{V}{z_0 + \Delta z} \tag{2.11}$$

where z_0 is a reference tip-sample distance, typically the SP value when the experiment starts. It follows from eq. 2.11 that it is possible to induce variations of the electric field changing the bias (V), but also, by modifying the tip sample distance (Δz) [60].

Recording STS at constant current mode in the field emission regime, the plot of the FER voltages (V_n) versus $n^{2/3}$ can be fitted to a line whose intersection with the ordinate axis (y) is the value of the work function (ϕ) (see eq. 2.10). For the first lowest bias resonances (obtained in constant current mode) the tip is still too close and out of the field emission regime for equation 2.11 to hold accurately. As a consequence, atomistic details of tip and surface can contribute significantly there, and then the first two resonances are commonly neglected from the fitting to obtain consistent ϕ values [59, 61]. In this thesis, we have experimentally obtained the shift of the Ag(001) work function when an ultra-thin MgO film is deposited, by measuring the FER resonances on both materials (Chapter 5).

2.3.2 Controlling the surface electric polarization

From eq. 2.9 it follows that the electric polarization of a surface determines its work function, and then it can be treated as a fundamental element in tunneling and charge transfer processes (ϕ^{CT}) between the substrate and the adsorbate. In the case of ferroelectric [60] and piezoelectric [62] substrates, even in absence of charge transfer, the electrostatic energy of the adsorbates is modified by controlling the electric polarization of the substrate. In the chapter 6 of this thesis, we investigate the use of an electric field (eq. 2.11) to induce effective gating in the electronic structure of graphene nanoribbons adsorbed on a monoatomic layer of MgO.

There is another way to tune the surface electric polarization. This is by introducing defect point charges that induce local perturbations of the electrostatic energy landscape [63]. The point charges are spontaneously created in defect sites of ionic insulators due to uncompensated charges at a precise point [60], but also in highly pure metals when impurities with localized electronic states are present [64, 65]. When the charged state of these defects have a long enough life-time, their presence can be identified by $\mathrm{d}I/\mathrm{d}V$ maps showing sharp rings (oval shaped) centered at the point defect, whose size depends on the tip-sample distance [64, 66]. In chapter 6, we image charging rings in $\mathrm{d}I/\mathrm{d}V$ maps around point defects in MgO ML, which happen to gate the electronic states of GNRs depending on their relative distance.

2.4 Experimental set-up

For the preparation of macromolecular structures by direct synthesis on metallic substrates (OSS), it is required to ensure a clean environment such as the one that ultra-high vacuum (UHV) provides. The UHV systems used for the experiments of this thesis are operated in the range of the low 10^{-10} mbar. This ensures a clean environment free of adsorbates and impurities during the preparation and characterization of the samples. The characterization of the samples require atomic resolution, and the physical interaction between the molecules and the surface requires low temperatures to immobilize them at some extent, as well as to enhance the performance of SPM techniques. The low temperature STM (LT-STM) working at temperatures below 5K are the perfect equipment for electronic characterization with atomic resolution of conducting systems, including the synthesized tructures studied in this thesis. For the experimental measurements, different systems hosted by the Advanced Microscopy Laboratory (LMA) at University of Zaragoza (Spain) and the Center for Materials Elaboration and Structural Studies (CEMES) in Toulouse (France) were used. These systems include three microscopes: a Joule Thomson STM (JT-STM) commercialized by SPECS GmbH (Figure 2.7) and two Low-Temperature STM (LT-STM) manufactured by Omicron Nanotechnlogy GmbH (Figure 2.8).

2.4.1 SPECS Joule-Thomson STM

The SPECS JT-STM is a microscope featured by a Joule-Thomson refrigerator to work at low temperatures, in the range of 4.9 to 1.1 K [67]. The JT-STM includes three cooling stages of which the first and the second are bath cryostats containing liquid N_2 and liquid ^{4}He respectively. The last stage consist of a Joule-Thomson refrigerator that reaches the lowest available temperature. At 1.1 K, the instrumental energy resolution in $\mathrm{d}I/\mathrm{d}V$ mode is 0.15 meV. All the experiments in this thesis have been performed within this temperature range, and when the temperature of 1.1 K plays a relevant role, the information is included in the corresponding caption. The JT-STM is integrated in a UHV multichamber system consisting of the load-lock chamber, two sample preparation chambers and the microscope chamber (Figure 2.7). In the UHV system we can find a total of 3 electron beam heaters (EBH), 3 sputtering ion guns, 10 metal evaporators, 3 organic sublimation evaporators, 7 independent gas dosing valves, a LEED/Auger unit and a mass spectrometer. All these accessories make of this UHV facility a powerful and versatile system for sample

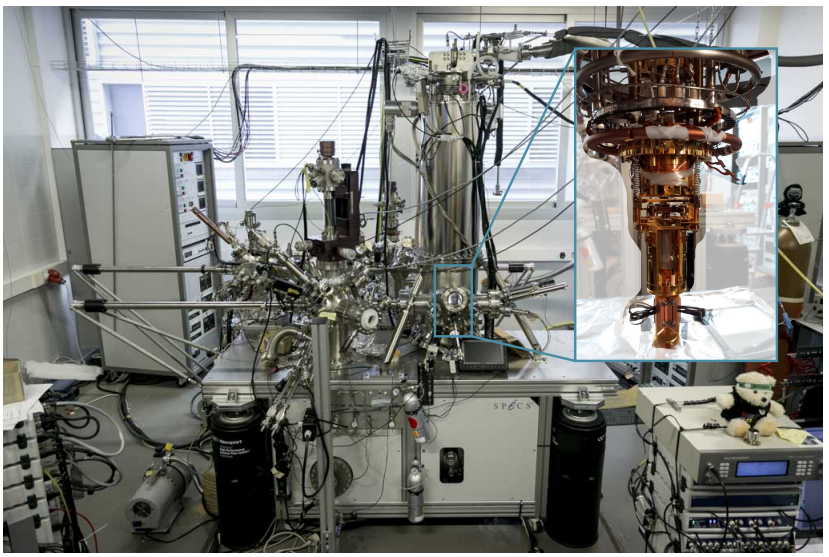

Figure 2.7: UHV system including the JT-STM at the LMA. The inset shows the STM body attached to the Joule-Thomson cryostat.

preparation and subsequent characterization in the microscope. The preparation and characterization of the samples showed in Chapters 4, 5 and 6 were carried out in this system.

2.4.2 Omicron LT-STM

The Omicron LT systems operate at 4.3K in UHV, with a base pressure lower than 1×10^{-10} mbar (Figure 2.8). The Omicron microscope combines the techniques of atomic force microscopy (AFM) and STM by means of a qPlus tunning fork sensor [68]. The UHV system at the LMA consists of the preparation, the load-lock and the STM chambers. The system includes a combined resistive heating and LN_2 cooling manipulator (temperature range 100 – 1100 K), 2 sputter ion guns, 4 gas dosing valves, 2 metal evaporators, an organic sublimation evaporator, a LEED and a mass spectrometer for sample preparation before the characterization in the LT-STM. The experiments shown in Chapter 3 were carried out in this system.

The UHV system at the CEMES is similar the one at the LMA and it consists on the same three chambers: the preparation, the load-lock and the STM chambers. For sample preparation it includes a resistive heating manipulator, a sputter ion gun, a gas dosing valve, a couple of ports for metal evaporators and a total of 6 heating stages. This instrument played an important role at

the optimization process of certain samples included in Chapter 4.

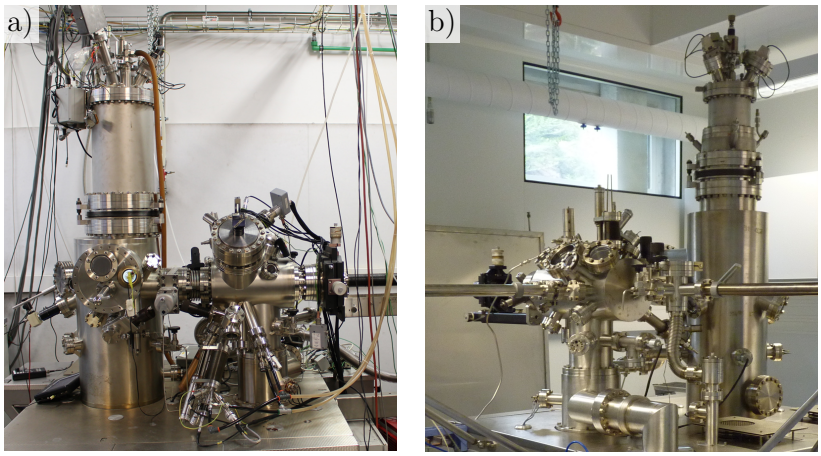

Figure 2.8: UHV systems including the Omicron LT-STM at the LMA (a) and at the CEMES facilities (b).

2.5 Sample preparation methods

The experimental work of this thesis was mainly carried out on three supporting surfaces, Ag(111), Ag(001) and MgO/Ag(001) on which we evaporated precursor molecules and/or individual metal atoms.

2.5.1 Crystal cleaning

The metal single crystals used in this thesis were cleaned by combination of sputtering and annealing cycles to ensure the good quality of the required atomically clean surfaces. For the sputtering, argon gas (Ar) is injected into the preparation chamber up to a pressure in the range of 10^{-6} mbar, then it is subsequently ionized to Ar^+ and finally focused with a high voltage gradient to produce an ion beam of $\sim$ 1 keV that collides with the sample surface to remove all the impurities and previous deposits (mechanical ion milling). The resulted irregular surface after the Ar^+ bombardment is then flattened and recrystallized with a thermal annealing process in the range of 400 to 800 °C, depending on the surface used.

2.5.2 Growth of thin MgO films on Ag(001)

The deposition of MgO on Ag(001) was optimized to obtain MgO monolayer (ML) islands embedded on the metal surface (section 5.1). We use a commercial Knudsen cell manufactured by CreaTec loaded with high purity rods of Mg to evaporate it in a O_2 atmosphere with a partial oxygen pressure of 10^{-6} mbar and deposition rates around 0.1 ML/min onto the clean Ag(001) crystal held at 360 °C. In order to obtain flatter MgO islands, a post-annealing of the sample is performed in UHV at the deposition temperature.

2.5.3 Molecule sublimation

In this thesis, organic molecules are sublimated in order to create larger structures synthesized directly on the surfaces. For such purpose, we have used two types of home-built molecular evaporators that we name as fixed-evaporators (Figure 2.9a) and mini UHV evaporator (Figure 2.9b). The design and manufacture of these evaporators are two examples of the successful technological innovations developed with the financial support of the TNSI project (INTERREG V-A Spain-France-Andorra program).

The fixed-evaporator consist of a Knudsen quartz cell mounted on a CF40 flange with four electrical connections compatible with UHV. The crucible is rolled with a tungsten (W) wire with 0.5 mm of diameter. While passing a current through the wire the crucible is heated. The temperature can be monitored by a thermocouple and the rate of molecule evaporation by positioning a quartz micro balance (QMB) in front of the evaporation beam. The distance between the crucible and the QMB is as short as it permits control deposition rates in the order of 3 ML/h.

The mini UHV evaporator is a home made resistive evaporator mounted on a sample holder compatible with the sample parking compartment inside the UHV system. The resistive heating stage is a boron nitride mini button heater commercialized by HeatWave Labs Inc. The mini UHV evaporators are placed in front of a QMB to measure the evaporation rate and include a thermocouple to monitor the crucible temperature during evaporation. The robust design of the mini UHV evaporator allows us to obtain reproducible samples with optimized parameters. The main advantage of this design is that several mini UHV evaporators can be stored in the UHV system, and thus, this permits faster exchanges of the precursor molecules that we want to sublimate. Also reloading the evaporators with different precursor molecules can be done through the load-lock port, making unnecessary to vent UHV parts of the

chambers and hence avoiding all the associated baking processes.

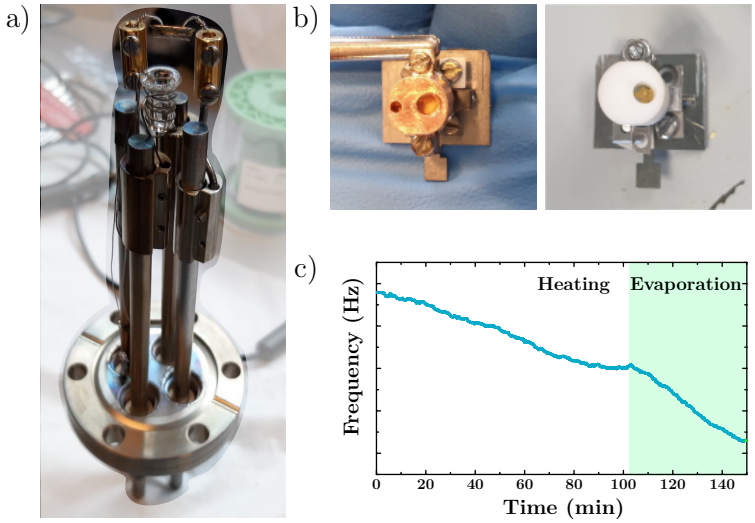

Figure 2.9: Photographs of the home-built molecule evaporators used in this thesis. a) Fixed-evaporator. b) Mini UHV-evaporators with crucibles made of copper (left) and alumina (right). c) Frequency shift variations during heating and molecule evaporation with a mini UHV evaporator. The constant slope (green shadow) allows us to know when the precursor evaporation takes place and to regulate its rate by tuning the externally supplied power.

2.6 Tip functionalization

In 2005, Jasch Repp *et al.* [69] reported an outstanding resolution enhancement in STM images when a pentacene molecule was located on the apex of the STM tip. Afterwards, different studies have been demonstrated that atoms (Xe, Cl) or molecules (H_2, CO, CH_4) picked up by the tip in a controlled fashion (controlled vertical manipulation) can be used to resolve in detail the bond structure of organic molecules [41, 70]. In this bond-resolved STM (BR-STM) imaging mode, the atom or molecule at the apex works as a transducer, sensing the repulsive forces that induce the compression or relaxation of its bonds (vibrational modes), which in turn causes a readable response in the tunneling current [71]. In essence, the picked adsorbate can be seen as an atomic scale AFM cantilever.

We have functionalized the tip picking up CO molecules from Ag(111) (Chapter 3) and Ag(001) (Chapters 4 and 5) surfaces. The protocol consists

in placing the tip above the CO molecule with a set point of 5 mV and 100 pA, open the feedback to fix the tip-sample distance and then observe the tunneling current while approaching the tip in 10 pm steps. When the CO molecule is transferred to the tip apex an abrupt reduction of the tunneling current is observed and the tip can then be retracted to the initial tip-sample distance to close the feedback. The presence of the CO at the tip apex can be confirmed by three approaches: (i) imaging the same area already measured with the metallic tip, (ii) imaging another CO or (iii) by recording inelastic electron tunneling spectroscopy (IETS) of a clean metallic surface.

Scanning the same area before and after picking up a CO tip shows an improvement of the resolution. Atomic resolution of the surface or intramolecular structures are easily obtained while imaging with sensitivity to the CO-hindered translational vibration [72]. A standard metal tip images the CO adsorbed on Ag(111) and Ag(001) as a depression, but a CO tip shows it as a protrusion, whose symmetry depends on the position of the CO molecule at the tip [73, 74]. By recording a IETS spectrum on the clean metallic surface it is possible to recognize the vibrational modes of the CO molecule at the tip apex.

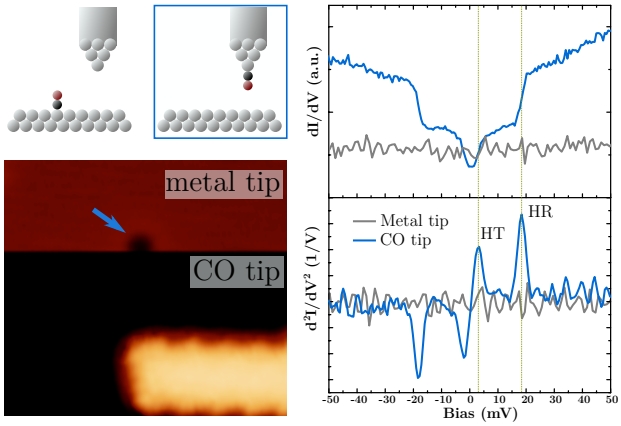

Figure 2.10: Schematic CO tip preparation, STM image (down scan) of a zone before and after transferring a CO molecule (marked by blue arrow) to the tip (50 mV, 50 pA, 6×6 nm^2) and experimental IETS spectra obtained before (grey) and after (blue) picking up a CO molecule from Ag(001) substrate (T = 1.15 K, SP: 50 mV, 200 pA; $V_{mod,\,Ag\,tip}$ = 1 mV, $V_{mod,\,CO\,tip}$ = 0.4 mV).

Figure 2.10 shows the picking up of a CO molecule on Ag(001). In the STM image (down scan) the CO on the metallic surface (blue arrow) is imaged as a

dark depression, and after picking it up, the tip approaches to the surface by about 1 Å, which is a typical consequence of adding a molecule to the tip apex, whose density of states is much lower than the previous metallic termination. The experimental IETS recorded on the metallic surface with metallic and CO tips are also shown in Figure 2.10. The obtained hindered translational (HT) and rotational (HR) modes appear at characteristics energies of 3.2 and 18.5 mV respectively [72], which corroborate tip functionalization.

Chapter 3

Coupling of magnetic atoms to organic optical switches

The development of electronic devices based on organic materials is becoming more popular due to the high efficiency, low cost and great diversity in the pool of organic molecules [75–77]. The molecular electronic devices are the ultimate downscaled electronic devices consisting on a functional individual molecule. The main requirement for the molecule is to have different electronic states that are responsive to external stimuli, preferably in a bistable manner. These perturbations can be magnetic field, electric field or light. When bistable switching between molecular states is achieved, it should be reversible and give rise to readable responses. The diversity of molecular structures enables the emergence of new functionalities, which are inaccessible in bulkier materials.

In this chapter we show the design and fabrication process of individual manganese phthalocyanines with four optically active moieties. We demonstrate the presence of two stable and distinguishable configurations of these moieties by STM and STS techniques, and we prove the reversibility of their switching on the surface. The electronic differences depending on the configuration, render our designed metal-organic complex as a promising candidate for its application in electronic or opto-electronic devices.

3.1 Design of a functional metal-organic complex

The most important factor to take into account for the design of a functional molecule is its stability. Phthalocyanines and porphyrines are well-known or-

ganic molecules that can be linked with most of the metals to form stable metal-organic complexes [78]. Their stability has stimulated their study for technological applications with particular attention in organic photovoltaic devices [79–81], sensor systems [82] and heterogeneous catalysis [83–85]. Since the first time STM was used to study individual porphyrines [86], a great research effort has been devoted to understand structural properties of adsorbed porphyrins and phthalocyanines. In metal- porphyrins and phthalocyanines complexes, the planarity of the macrocyclic aromatic ligand results in strong interactions with the substrate when the complexes are adsorbed on surfaces. This interaction results in chemical, electronic or magnetic state modifications of the central metal ion. The complexes containing first-row transition metal (TM) centers are of high interest because of the possibility to tune their spin state by modifying the complex-substrate interactions. Most of the work to control the spin state of TM complexes has dealt with the sensitivity to adsorption sites on the substrate [87–90], dehydrogenation of the macrocyclic ligand [91, 92] and coordination of axial ligands [93–96], with the subsequent recognition of different and controllable spin states by STM techniques. However, these approximations are not optimal for molecular spintronics because the adsorption site of the complex cannot be easily changed, the dehydrogenation of the ligand is not reversible and the gas injection required to coordinate a new axial ligand is not molecule specific, which would be desirable features in a molecular scale spintronic device.

We propose to integrate moieties with optical response in a manganese phthalocyanine (MnPc), to produce structural changes at the macrocyclic ligand and investigate the coupling of such changes with the Mn spin state. Several molecular switches adsorbed on different surfaces have confirmed to be reversibly interconverted by electric field [97], electrons [98–100] or photons [101, 102]. We decided to use diarylethene (DAE) derivatives, which have been proven to be easily switched on the surface [103, 104], to link them to the phthalocyanine ring. The designed molecular structure of the proposed functional manganese phthalocyanine is shown in Figure 3.1, hereinafter H-MnPc. The branches of the ligand enclose four DAE moieties as branches, which are intended to switch between open and closed configuration in response to external perturbations.

We use manganese as central metal ion in our complex because MnPc have been proven to host robust spin moments adsorbed on the surface, together with a tendency to exhibit underscreened Kondo effect [105–107]. The differences in Kondo excitations, which can be read by STS, might constitute a good candidate to play the role of an output signal sensitive to the structural

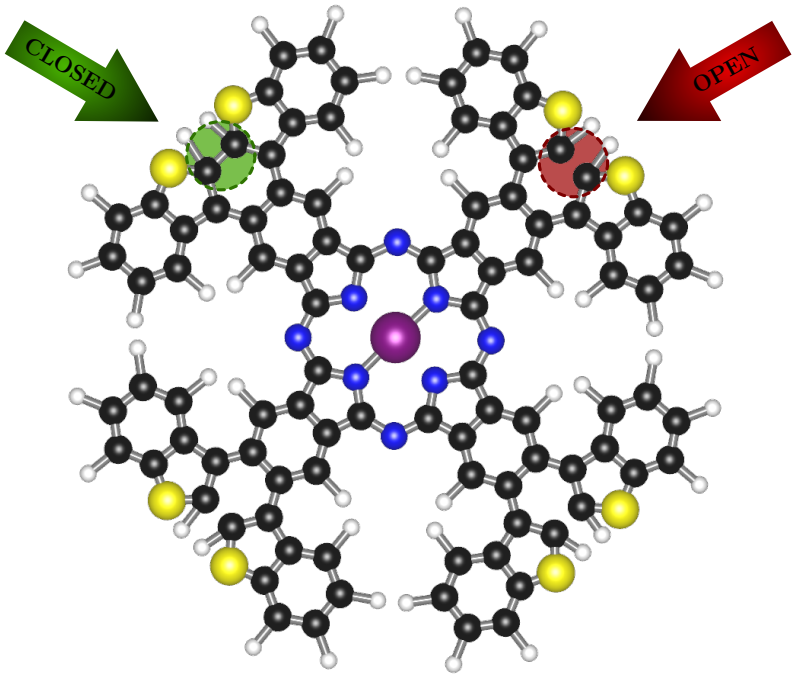

Figure 3.1: Molecular structure of the designed MnPc. The carbon atoms are coloured black, the nitrogen atoms blue, the hydrogen atoms white, the sulfur atoms yellow and the manganese atom violet. Structure representation performed with VESTA [108].

changes at the organic macrocyclic.

3.2 Fabrication of functional MnPc on Ag(111)

The complexity of the designed phthalocyanine makes OSS specially suitable for its synthesis. The precursor molecule, 4,5-bis(benzo[*b*]thiophen-3-yl)phthalonitrile hereafter compound **1a** (see its chemical structure in Figure 3.2), was synthesized by our collaborators Sabela Quiroga-Fernández and Diego Peña from Universidad de Santiago de Compostela. The structure of **1a** includes two benzothiophene groups forming the DAE moiety. In solution, **1a** shows a reversible light-induced transformation represented in Figure 3.2. When UV light of 365 nm wavelength irradiates a solution of **1a** in CH_2Cl_2, the photochemically induced electrocyclic reaction takes place producing a change of the solution color from transparent to blue. According to the Woodward-Hoffman rules, the cyclation is conrotatory giving the *trans*-closed isomer.

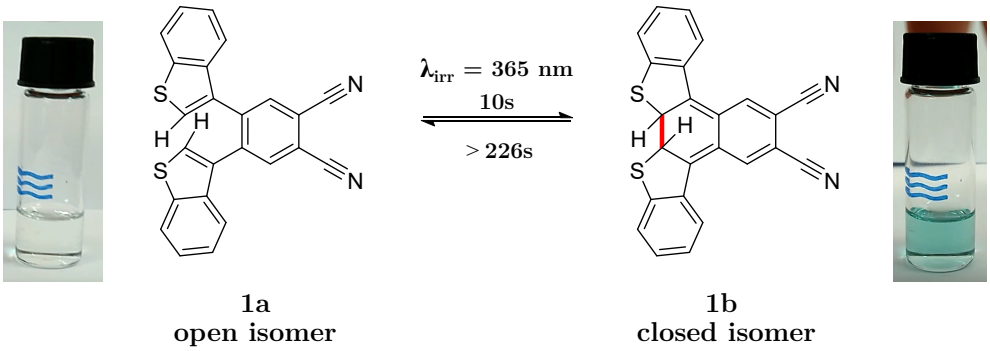

1a
open isomer

1b
closed isomer

Figure 3.2: Scheme of the reversible reaction between **1a** and **1b** that takes place in solution after irradiation with UV light (λ = 365 nm). Real pictures of the solution taken before and just after irradiation are include beside their respective structure.

1a includes two cyano (CN) groups in adjacent carbons that are expected to cyclotetramerize leading the phthalocyanine ring around the Mn ion in the designed complex (H-MnPc). Up to now, OSS of metal-phthalocyanines has been reported using tetracyanobenzene molecules, a much smaller precursor molecule [109, 110]. To ensure the viability of OSS pathway shown in Figure 3.3, with our larger precursor molecule, a fully conjugated molecule with the same carbon skeleton, from now on compound **2**, was used to synthesized another Mn phthalocyanine with planar branches, hereinafter π-MnPc (see Fig. 3.3). The precursor molecules and the two target MnPc are represented in Figure 3.3. Both MnPc have a common phthalocyanine ring (yellow shadow) but differ in the peripheral thioacene moieties (blue shadow) whose structures should depend on the precursor molecule. The main difference between H-MnPc and π-MnPc is the absence of hydrogen atoms in the conjugated species.

The MnPc were synthesized in a two steps reaction [109]. First, we co-evaporate the precursor molecules (Fig. 3.3) with Mn atoms onto a clean Ag(111) surface, and then, we post-anneal them to cyclotetramerize the cyano groups around the metal atom.

The co-evaporation of **2** and Mn atoms results in the coordination of four precursor molecules with a Mn atom. Figure 3.4a shows a representative survey of the samples obtained after co-evaporation onto the clean Ag(111) surface held at 50 °C. We distinguish individual coordinated units spread along the surface. The coordinated units show fourfold symmetry consisting in four identical molecules around each Mn atom (Figure 3.4b). Figure 3.4c shows the molecular model proposed for Mn + four ligands where cyano bonds of **2** point toward the Mn atom.

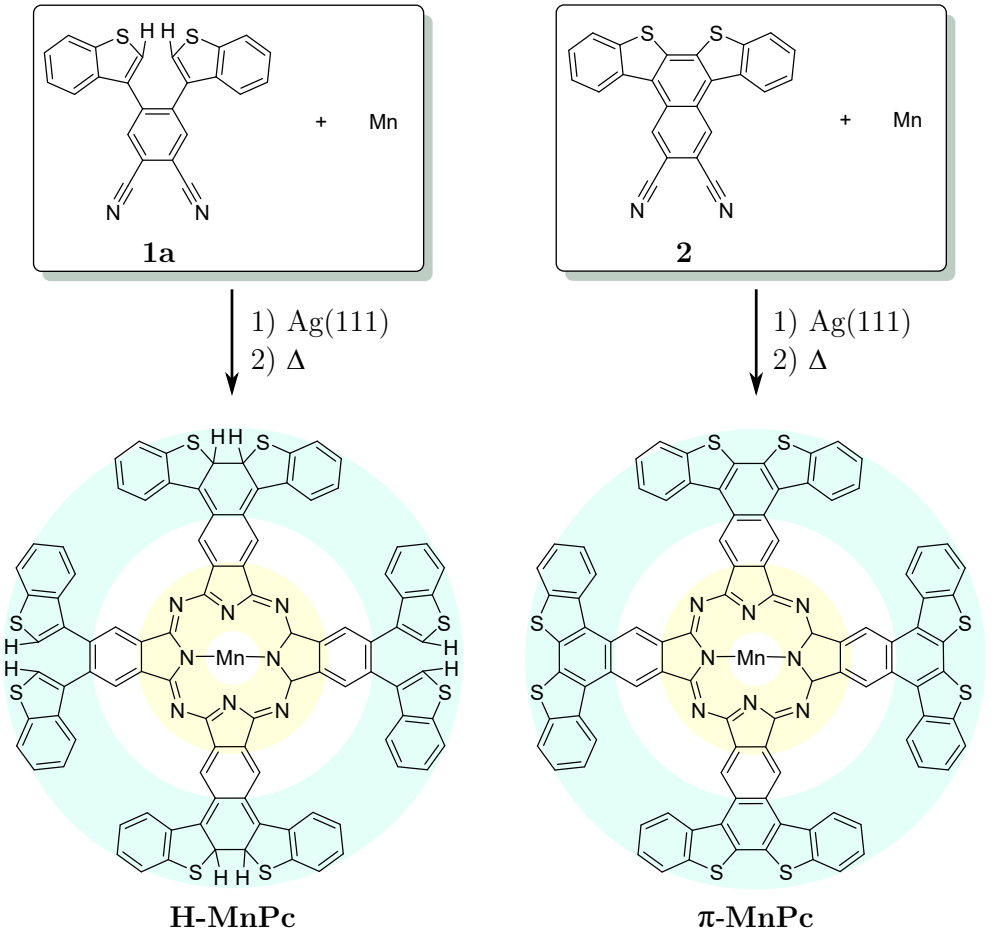

Figure 3.3: Schematic synthesis of the MnPc followed in this thesis. The structure on the yellow shadow corresponds to the common phtalocyanine ring for both MnPc, and the blue shadow shows the thioacene moieties whose structures depend on the chemical structure of the precursor molecule employed for the synthesis.

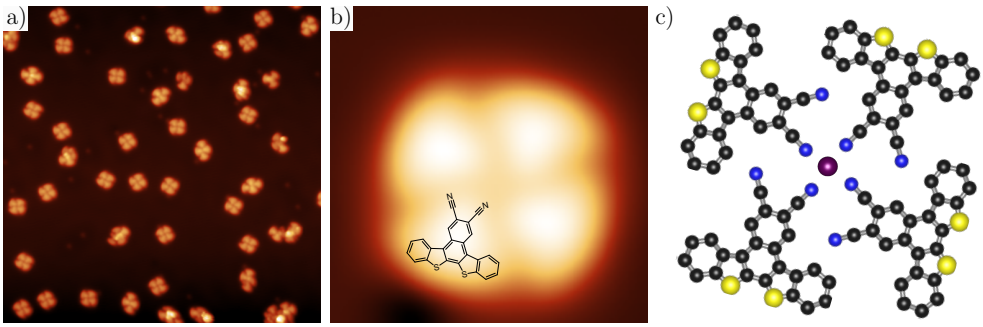

Figure 3.4: STM images of samples obtained after co-evaporation of Mn atoms and molecule **2** on Ag(111). a) Survey of coordinated units of Mn + four **2** ligands. SP: -1 V, 0.1 nA (50×50 nm^2). b) Mn + four **2** ligands with the chemical structure of **2** superimposed. SP: 0.7 V, 0.1 nA (3.5×3.5 nm^2). c) Proposed molecular model for coordinated units.

After post-annealing the sample up to 350 °C for 30 minutes, individual π-MnPc are obtained on the surface (Figure 3.5a). The presence of subphthalocyanines and defective ligands around the Mn atoms suggests that the optimal temperature to cyclotetramerize **2** is below 350 °C. The planar shape of π-MnPc molecules allows us to obtain bond resolved STM (BR-STM) images recorded in constant height mode with CO-functionalized tips. Figure 3.5c shows the BR-STM image of a π-MnPc whose chemical structure is recognizable. This confirms that the space between the branches of the macrocyclic ligand permits the cyclotetramerization of the precursor molecules without major structural distortions.

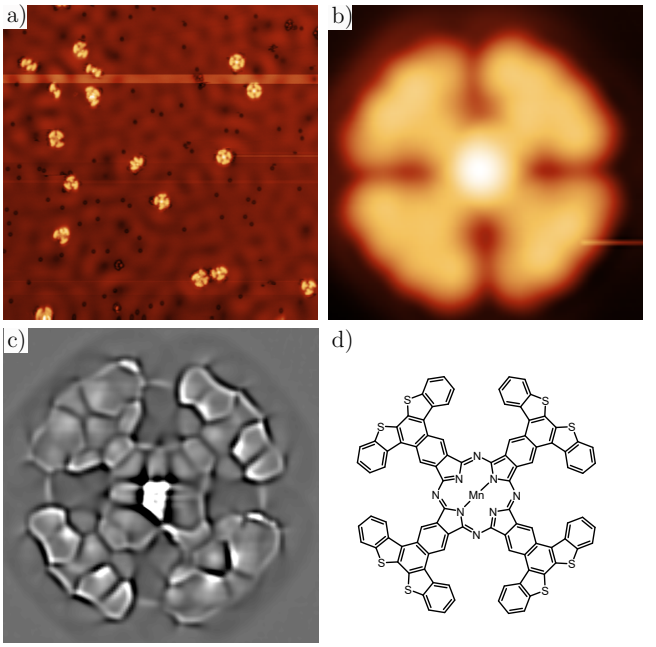

Figure 3.5: STM images of the samples obtained after post-annealing of the samples shown in Figure 3.4 at 350 °C for 30 minutes. a) Representative surveys of π-MnPc. SP: 10 mV, 5 pA, (50 × 50 nm^2). b) Zoom in an individual π-MnPc. SP: 0.5 V, 100 pA, (2.8 × 2.8 nm^2). c) Laplace filtered BR-STM image of a MnPc recorded with a CO-tip. SP: 3 mV, (2.8 × 2.8 nm^2). d) π-MnPc chemical structure fitting the image in (c).

On the other hand, when **1a** is co-evaporated with Mn atoms onto Ag(111) held at 50 °C, coordinated units are also obtained, but the presence of hydrogen atoms at the labile bonds of the DAE moieties leads to the self-assembly of the units in ordered islands with squared unit cell. A representative survey of the samples obtained is shown in Figure 3.6a. To better visualize the position of the ligands and Mn atoms, an individual tetramer was dragged out of the island by lateral atomic manipulation (section 2.2). Figure 3.6b shows the island and the unit extracted by atomic manipulation and Figure 3.6c shows a zoom in the individual coordinated unit. The fact that tip extracts with mild parameters (open feedback SP: -5 mV, 500 pA) undamaged units from the island, illustrates the weakness of the intermolecular forces between them in the island (as it is expected for H-bonding [111]) compared with the coordination bond between Mn and N atoms.

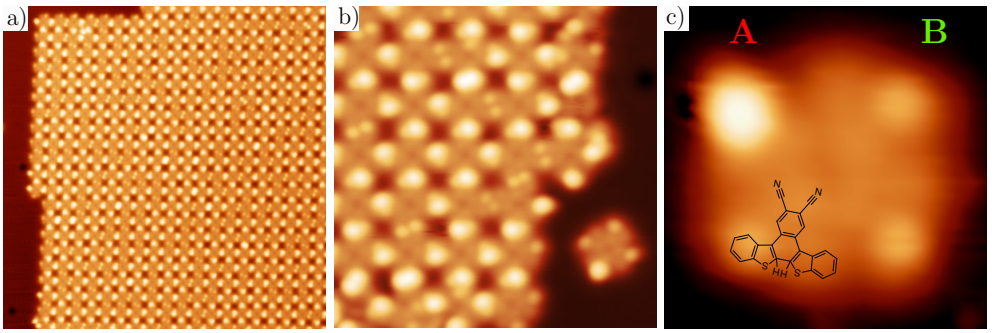

Figure 3.6: STM images recorded on the samples obtained after co-evaporation of Mn atoms and precursor molecule **1a** on Ag(111). a) Island of self-assembled coordinated units of Mn + four **1**. SP: 0.6 V, 100 pA, (50 × 50 nm^2). b) Zoom in the island. SP: 0.5 V, 50 pA, (20 × 20 nm^2). c)Individual coordinated unit extracted from the SA island. SP: 0.6 V, 0.6 nA, (3.5 × 3.5 nm^2).

In the islands and in the individual units it is possible to distinguish ligands with two different apparent shapes. In Figure 3.6c these ligands are labelled depending on their apparent heights as A configuration (with brighter lobe) and B configuration. As explained in section 3.1, the DAE moiety in **1** can switch between different isomeric forms in solution (Figure 3.2). The topography differences observed in the STM images of the ligands around the Mn suggest the presence of two isomeric configurations when **1a** is deposited on the surface. The interaction between A and B configuration does not play any role in the structure of the island (Figure 3.6b), appearing at equivalent lattice sites indistinctly of their shape. This suggests that the corresponding configurations must have a very similar molecular structure, as would be the case of the *open-* and *closed-* isomers of **1** (**1a** and **1b** in Figure 3.2). The statistical analysis elaborated out of 452 ligands reveals an A/B configuration abundance ratio of 0.72. The total energies obtained from DFT calculations by the group of Daniel Sánchez at CFM for open (**1a**) and closed (**1b**) configurations on Ag(111) are included in Table 3.1. The calculation yields the open isomer as the most stable configuration, closely followed by the *trans*-closed isomer, which is in good agreement with the observation of two configurations in the coordinated units. Besides, the lack of mirror symmetry of A and B ligands allows us to rule out the presence of the more energetic *cis*-closed configuration in the coordinated units.

Isomeric configuration	Total energy (eV)
Open (reference)	0
trans-Closed	0.05
cis-Closed	0.19

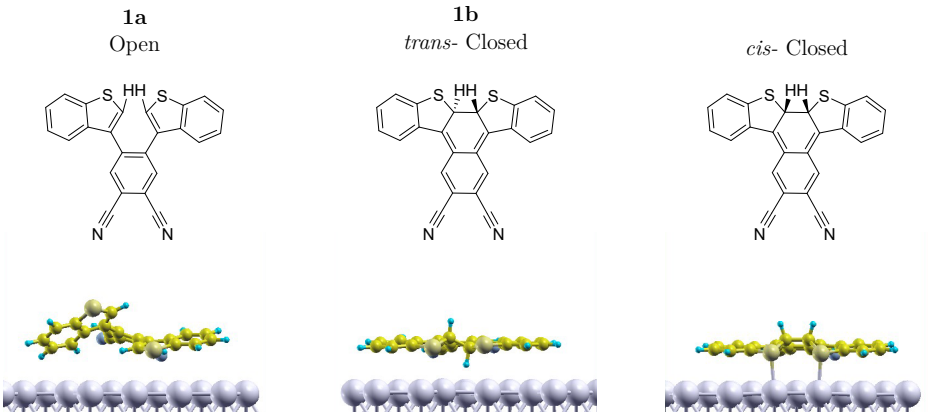

Table 3.1: Calculated parameters for open (**1a**), *trans*-closed (**1b**) and *cis*-closed configurations of **1** adsorbed on Ag(111). These calculations were carried out by C. García-Fernandez and D. Sánchez-Portal from CFM (UPV/EHU-CSIC).

The optimal post-annealing to achieve cyclotetramerization of **1** is 300 °C for 30 minutes. In sharp contrast again with monodispersed π-MnPc, H-MnPc are packed in islands with squared unit cell (Figures 3.7a-b), which are stabilized by H-bonding. The intermolecular interactions leading to the same square lattice arrangement as in the coordinated sample confirm thereby the preservation of the hydrogen atoms at the DAE moieties of the phtalocyanines. As occurred with coordinated units, H-MnPc are easily extracted from the islands by atomic manipulation. In Figure 3.7c two different apparent shapes of branches are distinguishable in an intact H-MnPc extracted from the island. Following the nomenclature for the ligand configurations observed in the coordinated units, we label the branch configurations with higher and lower apparent height as A and B respectively.

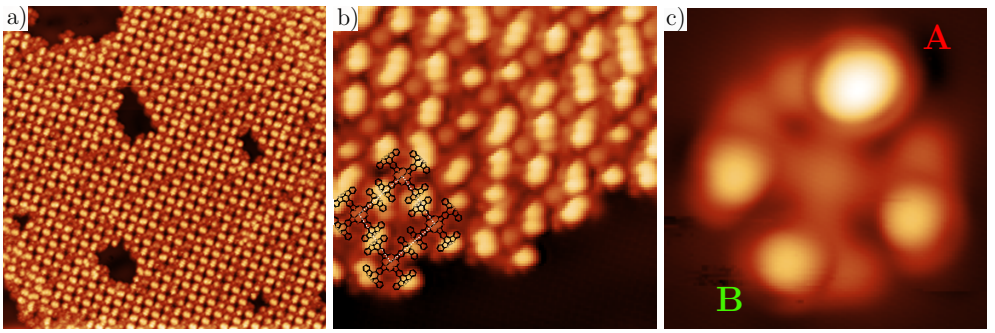

Figure 3.7: STM images recorded on the samples shown in Figure 3.6 after post-annealing at 300 °C for 30 minutes. a) Representative survey of H-MnPc. SP: 10 mV, 5 pA, (50 × 50 nm^2). b) Zoom in the lateral of the island. SP: -0.1 V, 10 pA, (12 × 12 nm^2) with a tentative model of the H-MnPc squared unit cell is overlapped. c) STM image of an individual phthalocyanine extracted from the island by lateral atomic manipulation. SP: 0.5 V, 100 pA, (3.5 × 3.5 nm^2).

To better understand and unveil the nature of both configurations, we addressed individual H-MnPc with two purposes. First, to achieve a more definitive assignment of experimental observed A and B branch configurations. And second, to verify the adequacy of H-MnPc for molecular electronics. As H-MnPc are found self-assembled, individual complexes can be obtained only by atomic manipulation. Several phthalocyanines were repositioned out of the island by lateral atomic manipulation (see section 2.2) for detailed characterization and to study the switching between the A and B configurations, which we tentatively assigned to open and closed configurations. The manipulation was carried out at constant height using low negative bias and currents between 0.5 and 1 nA as initial set point. A sequence of STM images during manipulations of H-MnPc is shown in Figures 3.8a-c. The manipulation trace shown in Figure 3.8d has a periodicity of 2.8 Å, which corresponds to the motion of the complex along a closed-packed crystallographic direction of the Ag(111).

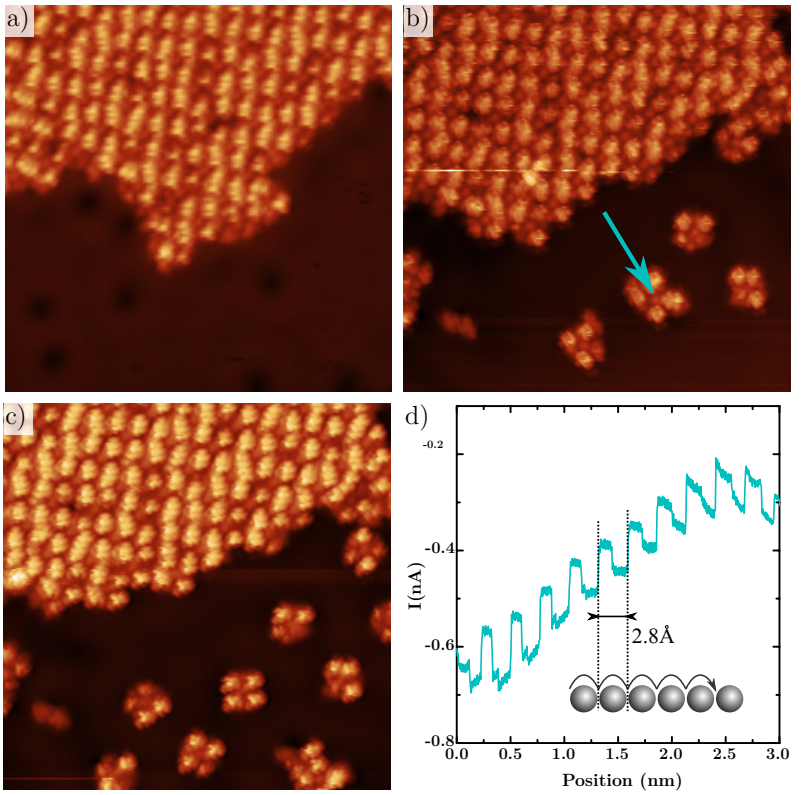

Figure 3.8: a-c) Sequence of STM images recorded during lateral atomic manipulation of H-MnPc. d) Trace of manipulation of an phthalocyanine along a closed-packed crystallographic direction of the surface. The blue arrow in b represents the direction of the manipulation trace in d.

3.3 Characterization of switchable MnPc

3.3.1 Structural characterization of H-MnPc

As described in section 2.6, the functionalization of the tip with a CO molecule enables the resolution of intramolecular structures. However, the height differences between A and B configurations in H-MnPc branches impede scanning the whole complex in constant height mode with intramolecular resolution, and then, the BR-STM images recorded on H-MnPc are partial. To obtain the complete image shown in the Figure 3.9a, a combination of two BR-STM images recorded at a tip-sample distances difference of 0.23 nm is required.

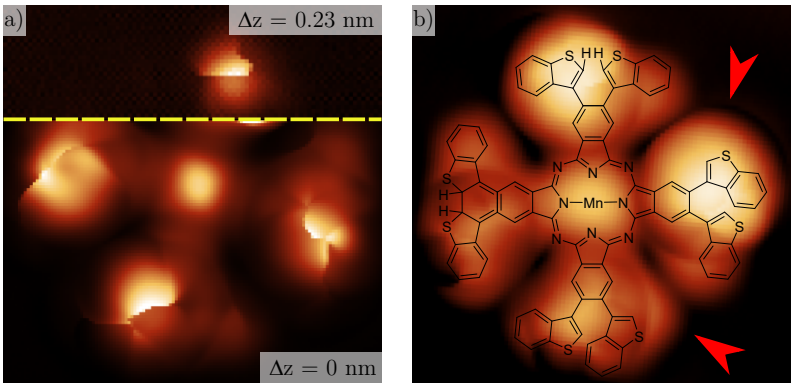

Figure 3.9: a) Combination of BR-STM images recorded on the phthalocyanine with a CO-tip. SP: 3 mV, (3.5×3.5 nm^2). The yellow dotted line shows the limit between the image recorded at z position (bottom) and the recorded at $z + 0.23$ nm (top). b) High resolution STM image of another H-MnPc with a molecular model superimposed that includes the three DFT identified branch configurations (see Table 3.2).

This is in agreement with the 0.15 nm height difference of the branches retrieved from DFT calculations of adsorbed H-MnPc on Ag(111). In Table 3.2 an overview of the relaxed H-MnPc structures with identical branches in open, *rot*-open and *trans*-closed configuration is shown. Each molecular scheme represents the phthalocyanine ring with one branch identical to the other three, which cis the molecular model used in the calculations. The lateral view of each H-MnPc structure is shown in the bottom row, highlighting the height differences (Δh_{max}). The calculations include a new isomeric configuration (*rot*-open) where a σ-bond between thioacene moieties is rotated and both sulphur atoms point to the surface, which gives rise to a significant decrease of the adsorption energy. Even if the total energy of H-MnPc with *rot*-open branches is lower than the energy of *trans*-closed phthalocyanine, we can discard the for-

mation of the *rot*-open configuration during the post-annealing process because its planar projection cannot be overlapped with the two naturally occurring configurations A and B in the individual H-MnPc (Figure 3.9b). Then, the experimental differences in apparent height compares well to calculated height of the branches if A and B configurations correspond to the open and closed ring configurations of DAE moiety respectively.

H-MnPc	**Total energy (eV)**	**Total magnetic moment (μ_B)**	Δz_{Mn} **(Å)**	Δh_{max} **(Å)**
Open (reference)	0	1.91	0.00	0.00
rot-Open	0.02	1.95	0.01	0.90
trans-Closed	0.67	1.89	-0.04	-1.50

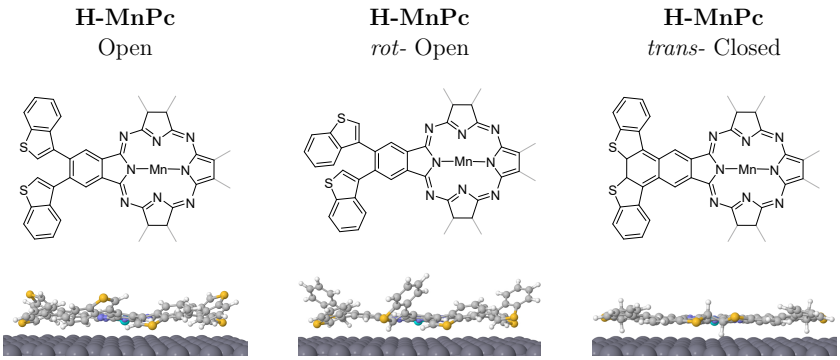

Table 3.2: Calculated parameters for H-MnPc with four identical branches in open, *rot*-open and *trans*-closed configurations adsorbed on Ag(111). Δz_{Mn} is the Mn ion distance to the last Ag slab of the surface (relative to the open configuration) and Δh_{max} indicates the maximum vertical height discarding the hydrogen atoms, also relative to the open configuration. These calculations were carried out by C. García-Fernandez and D. Sánchez-Portal from CFM (UPV/EHU-CSIC).

3.3.2 Electronic characterization of H-MnPc

The electronic structure of H-MnPc has been characterized by STS, measuring $\mathrm{d}I/\mathrm{d}V$ point spectra and constant current $\mathrm{d}I/\mathrm{d}V$ maps at various bias voltages. The $\mathrm{d}I/\mathrm{d}V$ point spectra were taken over the the Mn ions and along the ligands for self-assembled H-MnPc inside the island, as well as for individual complexes extracted from the islands. Regardless of whether the H-MnPc are (inside or outside the island), significant differences between A and B configu-

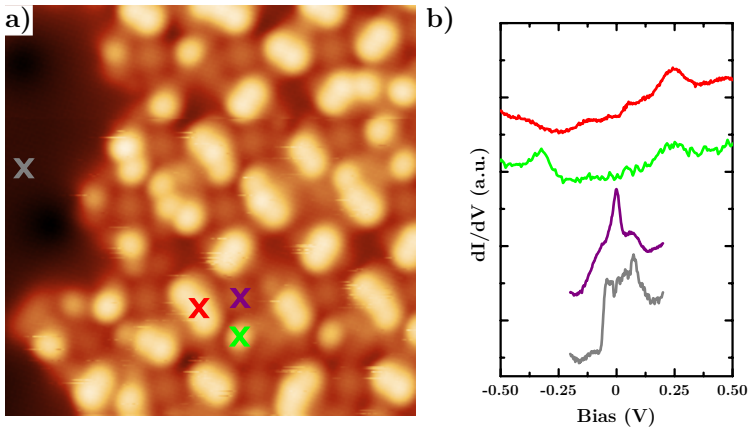

Figure 3.10: a) STM image of a self-assembled island of H-MnPc. b) Conductance dI/dV spectra recorded on branches with open (red) and closed configuration (green), manganese ions (violet) and the reference of the silver substrate (grey). The crosses in a) represent the equivalent positions along the island where the dI/dV spectra were recorded.

rations branches are observed. Hereafter the named configurations A and B are referred as open and closed following the conclusions of the previous section.

When the H-MnPc are packed inside the island it is difficult to distinguish the branches that correspond to each phthalocyanine. However, the topography differences between open and closed configurations are clear enough to record dI/dV spectra at their respective positions. Figure 3.10 shows a zoom in a self-assembled island of H-MnPc and the dI/dV spectra recorded on branches with open (red) and closed configuration (green), manganese ions (violet) and the Ag(111) substrate (grey). We show averaged dI/dV point spectra recorded on equivalent positions throughout the island, as the ones indicated by the crosses in Figure 3.10a.

To study individual H-MnPc, several of them (15 in total) were extracted from the island by lateral atomic manipulation (see section 3.2, Figure 3.8). Figure 3.11 shows a STM image of six individual complexes and the averaged dI/dV spectra recorded on branches with open (red) and closed configuration (green), manganese ions (violet) and silver substrate (grey). Similarities with STS spectra recorded in the packed island are observable and demonstrate that lateral atomic manipulation do not alter the structure of the H-MnPc. The sharp Mn peak crossing the Fermi level persists in individual H-MnPc and the conductance spectra recorded on closed configuration branches shows

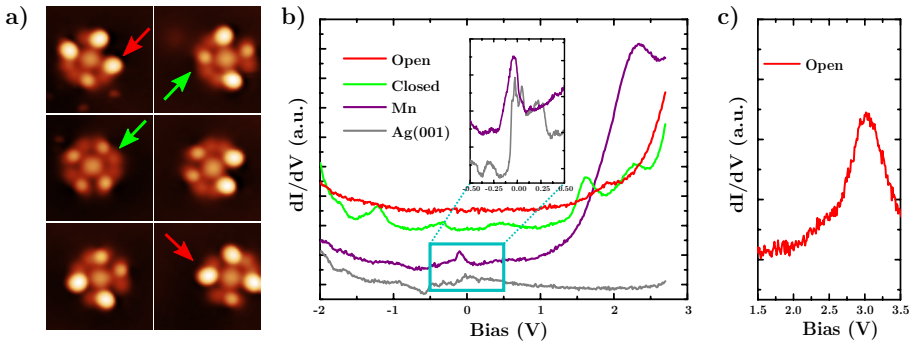

Figure 3.11: a) STM images of six phthalocyanines dragged out of the island. SP: -50 mV, 20 pA, (5×5 nm^2). Red arrows point to open configuration branches and green arrows point to closed configurations. b) STS spectra recorded open feedback on the branches with open (red) and closed configuration (green), manganese ion (violet) and silver substrate (grey). V_{mod} = 10 mV, SP: -1 V, 20 pA. The inset shows the high resolution STS recorded on manganese ion and silver. V_{mod} = 10 mV, SP: -0.5 V, 300 pA). c) STS spectrum recorded on an open branch under closed feedback conditions. V_{mod} = 10 mV, SP: 1 V, 100 pA).

the resonance at -0.3 V. The closed configuration presents other peaks at -1.20, 0.45 and 1.60 V, which is in contrast with the flat spectra obtained for open configuration in the same energy range. The dI/dV spectra recorded in constant current mode grants us access to see the range above 3 V where open branches show a peak at 3.1 V. We associate these electronic fingerprints with the molecular orbitals. For a fully conjugated configuration (as the closed configuration one) it is expected to obtain smaller gaps than for non-conjugated configurations, which is in agreement with the suggested designation of open configuration for A and closed configuration for B.

In Figure 3.12 we show a STM image and dI/dV map recorded in an individual H-MnPc with three open (1-3) and one closed (4) configurations of the branches at the energy of the molecular state observed in the green spectrum in Figure 3.11b. The calculated local density of states (LDOS) in the energy window (-1, -0.5) eV corresponding to the highest fully occupied molecular orbital of a H-MnPc with three open and one *trans*-closed configuration branches is displayed in Figure 3.11c. As expected from the previous assignment of A and B type branches, the theoretical LDOS of the occupied energy region is in good agreement with the dI/dV map recorded at -1.3 V (see Fig. 3.11b). For the closed branch (4) the highest intensity is closer to the thioacene moiety, whereas for the open branches (1-3) it is concentrated at the phthalocyanine

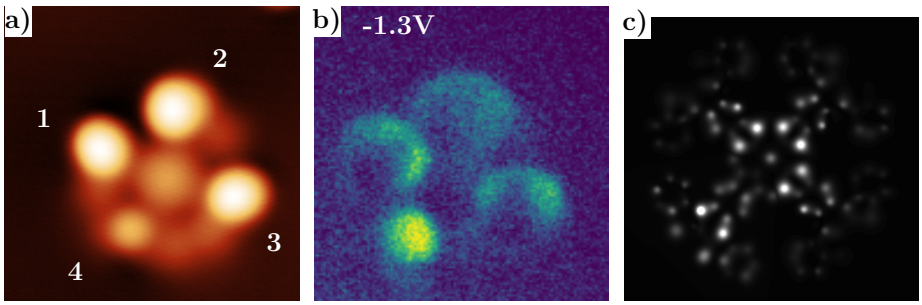

Figure 3.12: a) STM image of a H-MnPc with open (1-3) and closed (4) configurations at the branches. SP: -50 mV, 20 pA. b) dI/dV map at the energy of the molecular states observed in the dI/dV spectra shown in Figure 3.11b. V_{mod} = 10 mV, SP: -1.3 V, 100 pA. c) Calculated LDOS of a H-MnPc with the same branches configuration as the one in a) and b) obtained by integrating over the energy interval from -1 to 0.5 V.

ring.

The violet spectra showed in the Figures 3.10b and 3.11b correspond to the average of all the STS point spectra measured on Mn ions. For Mn ions in both, individual complexes or complexes inside the islands, STS spectra show this peak that cross the Fermi level (E_F). We investigated this feature by high energy resolution dI/dV spectra and attributed it to a Kondo resonance already observed for other MnPc on several substrates [105–107]. The Kondo resonance at zero bias is convoluted with another contribution at about -50 mV ascribed to $d_{xz/yz}$ orbitals, which are characteristic of D_{4h} squared planar symmetry group of the local Mn environment. In Figure 3.13a-c we show spectra recorded on manganese ions of individual H-MnPc with different branch configurations. Different combinations of open and closed branches around the Mn reproduce at low energy the same feature. Figure 3.13d shows the averaged spectra of those in Figure 3.13a-c fitted by the superposition of Fano (orange) and Gaussian (green) functions representing the Kondo resonance and d orbital states respectively (blue). The insensitivity of the Kondo resonance can be explained by the fact that the Mn d_{z^2} orbital, whose hybridization with the substrate's Fermi states is the leading term for the formation of the Kondo state, remains intact against structural changes of the surrounding branches. This result is in agreement with the predicted similarities of the magnetic moment and Mn-Ag distance obtained by DFT calculations (Table 3.2), and with the similar projected density of states calculations onto Mn d orbitals (Figure 3.13e).

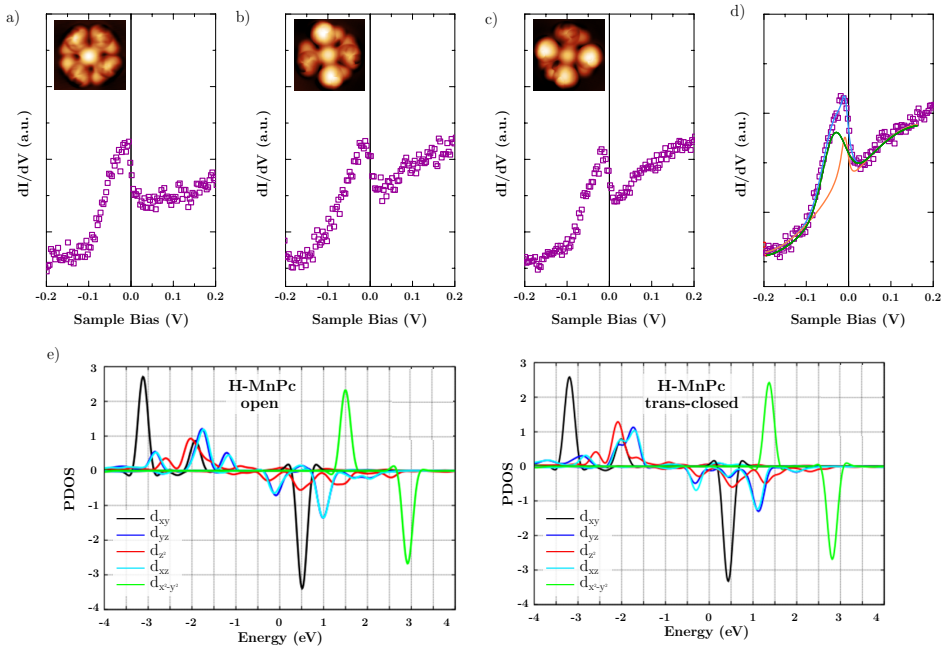

Figure 3.13: a-c) STS spectra recorded on Mn ions of H-MnPc (insets) with different branches configurations. V_{mod} = 1 mV, SP: -1 V, 20 pA. d) Averaged STS spectra recorded on Mn ions a-c (violet) fitted to a function (blue) which includes the Fano (orange) and Gaussian (green) functions representing the Kondo resonance and the orbital state respectively. e-f) PDOS calculations onto Mn *d* orbitals for H-MnPc with four open (e) and four *trans*-closed branches (f).

The electronic fingerprints of open and closed configurations can be summarized as follows. They posses different gaps and spatial density distributions of unoccupied states. Closed configuration shows a smaller gap and its spatial density of occupied states is distributed along the carbons of the thioacene moiety. In contrast, the open configuration was found to have a gap larger than 3 V (see Figs. 3.11b-s) and a spatial density of occupied states concentrated at the carbons of the phthalocyanine ring. These electronic fingerprints allowed us to distinguish between open and closed configurations during the study of the switchability of the DAE labile bond presented in the next section. The near Fermi level feature resolved over Mn ions, the DFT and PDOS calculations reveal a promising route to achieve the targeted optoelectronic response: to produce readable changes at the magnetic ground state of the Mn ion we require abrupt changes in Mn-Ag distance, which can be realized by controlling the relative height of the complexes, for example including bulky

functional groups at the branches.

3.4 Reversible switches on the surface

To study the switchability of our H-MnPc on Ag(111) we first tried with controlled bias ramps over the branches based on previously reported ring-closing reactions with DAE derivatives [112, 113]. The tip was located on top of the branch (SP: 1 V, 0.1 nA) and holding a constant tip-sample distance, the bias was ramped from 1 to 4 V. After this, the ligands changed and adopted new apparent shapes. An example is shown in Figure 3.14. The bias ramp recorded on the right branch (1) of the H-MnPc in the inset, produces three different changes in the complex. The bottom branch (3) changes from closed to open configuration, which can be considered as a switch. The right branch (1) changes into a double lobe configuration whose apparent shape and electronic characterization do not correspond neither to the open nor to the closed configuration. The open branch on the left (2) changes to a planar shape, which corresponds to the planar structure expected upon dehydrogenation of the labile bond (as it is the case in the π-MnPc in Fig. 3.5b). The changes in the branches (1, 2) were the most frequently obtained by ramping positive bias voltages. Furthermore, the ramping in the opposite bias sign did not produce the reverse change.

As an alternative method, we examined the possibility to induce the open-closing ring reactions making use of the intermolecular forces between tip and molecule. Approaching and passing the tip over the branches with low positive bias (5 mV) and high currents (15-50 nA), we observe switching events between open and closed configurations. In most of the cases, these tip-molecule forces also produce rotation or displacement of the molecule making difficult to follow the switching sequences. The apparent topographic shapes, and the spectroscopic characterization of the switched branches, correspond with the expected ones for open or closed configurations.

Figure 3.15 shows three sequences of STM images with clear switches between open and closed configurations. In Figure 3.15a the top branch switches from open to closed without rotation or lateral movement of the molecule, demonstrating that switching events are not related with adsorption site changes. In the sequence shown in Figure 3.15b, the interaction between the tip and the molecule produced not only the switching of one of the branches from open to closed, but also lateral displacement and rotation of the molecule. Figure 3.15c shows a sequence where two open configurations switch to closed

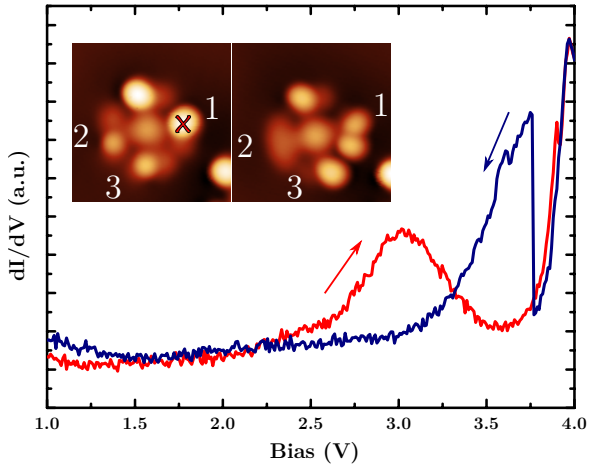

Figure 3.14: STM topographies before and after the bias ramp at the marked position by the red cross (-50 mV, 20 pA, 4 × 4 nm^2). Evolution of the conductance as a function of the bias during the bias ramp with positive voltage. It is possible to distinguish a jump in the backward of the ramp (blue line) when the switch took place.

configurations and after, one of the switched branches reversibly switches to open configuration. As described in the section 3.3.2, the electronic fingerprint of the Mn ions in the H-MnPc is independent of the surrounding branch configurations (see Fig. 3.13) and no readable response is obtained, at least within our experimental uncertainty.

Our data demonstrate that ring-closing reactions at the DAE labile bond of the synthesized H-MnPc take place on the surface. The reversibility of the switch and the stability of both configurations make these molecules promising candidates for electronic and opto-electronic applications.

3.5 Conclusions and outlook

In this chapter we have reported the design and successful fabrication of switchable manganese phthalocyanines on Ag(111) by combining on surface synthesis and atomic manipulation techniques. We have identified and characterized two different configurations of the functional phthalocyanine branches by scanning tunneling microscopy and spectroscopy techniques. The electronic characterization and DFT calculations allow us to assign these configurations to the open and closed ring forms of the DAE moiety.

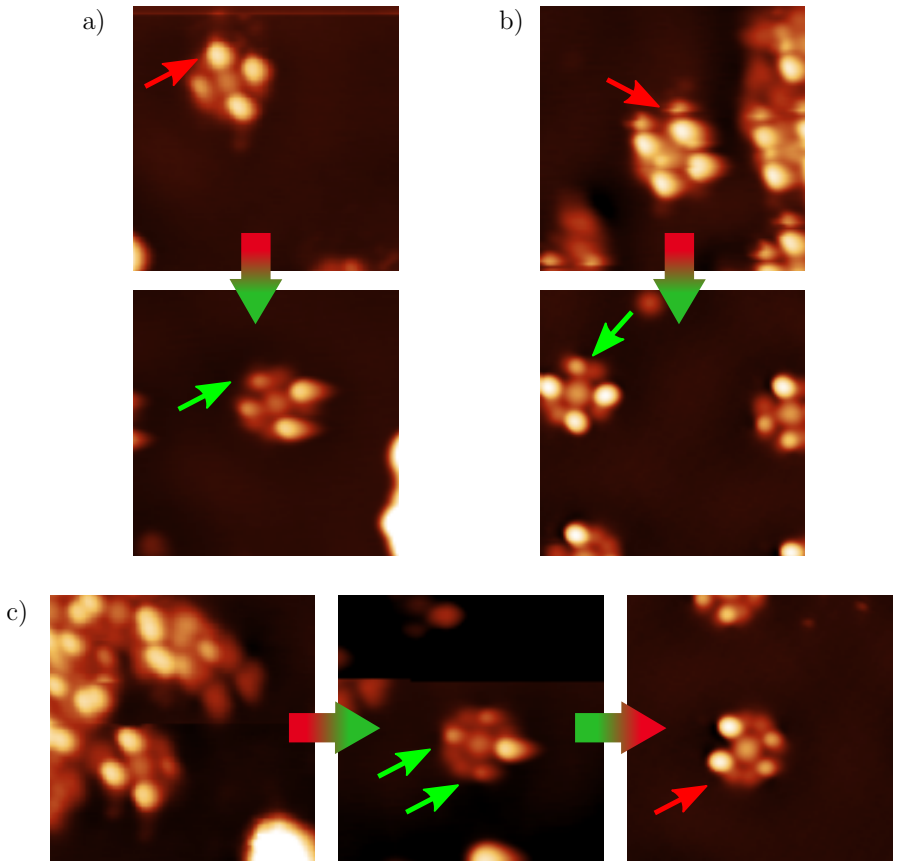

Figure 3.15: STM topographies before and after controlled switches (-100 mV, 50 pA, 8.75 × 8.75 nm^2). The arrows point to the switched branches. In the case of a) and b) the switches are from open to closed configuration, and the sequence in c) shows a reversible switch.

Our experiments reveal that reversible switching events between open and closed forms can be induced by tip-sample forces when the tip is driven across the branches with low bias and currents in the range of 15-50 nA. The reversibility of the switching on the surface and the electronic differences found between both configurations render the designed metal-organic complex a promising candidate for its application in molecular electronic and opto-electronic devices.

This work opens a new pathway for the fabrication of functional metal-organic complexes for molecular scale electronics. As detailed in section 3.1, the design of the complex can be modified to meet designated properties. To upgrade the design of our switchable MnPc we suggest to use different DAE

precursor molecules with bulky functional groups linked at the thioacene moiety in order to increase the difference in Mn-Ag distance while switching between configurations. Their incorporation at the carbons of the labile bond could also help to avoid self-assembly and subsequently atomic manipulation of the complex, simplifying their fabrication. A second approach would be to replace the central Mn ion with a different metal such us Fe or Co, whose adsorbed metal-organic complexes have been also reported to have two different readable spin states [91, 92].

Chapter 4

Semiconducting chiral graphene nanoribbons with tunable gap

Following the bottom-up methodology developed by Cai and coworkers in 2010 to synthesize an atomically perfect ribbon of graphene on a metallic substrate [13], we have synthesized graphene nanoribbons (GNRs) with chiral edges [27] on Ag(001) surface using chiral molecular precursors. The first section of this chapter is dedicated to discuss the remarkable impact of the chiral edges of GNRs in their electronic properties. Then, we present key synthetic aspects of the on-surface synthesis (OSS) of chiral GNRs (ch-GNR), to focus in the following sections on the electronic structure of ch-GNRs of different widths and lengths.

4.1 Chiral graphene nanoribbons

As discussed in section 1.3, the electronic properties of graphene nanoribbons are rooted in the electronic properties of graphene. The reduction of the graphene sheet into a 1D structure, the graphene nanoribbon (GNR), induces a gap due to electron confinement, which overcome what is probably the main handicap of graphene to be implemented in the standard architecture of devices based on semiconducting materials.

Since the synthesis of the first atomically perfect GNR [13], a large variety of armchair edges GNRs (a-GNRs) have been produced by OSS methods [114–121], which is in contrast with the limited number of reported zig-zag [23, 122] and chiral edge GNRs [123–128] (z-GNRs and ch-GNRs respectively). The

highly reactive zig-zag edges show a pronounced interaction with the substrate which could explain the difficulty of growing defect free z-GNRs. On the other hand, the number of reports based on ch-GNRs is currently on the rise, not only due to their easier synthesis compared with pure z-GNRs, but also because theoretical calculations predict for ch-GNRs a combined electronic structure of a-GNRs and z-GNRs, showing the semiconducting band gap of a-GNRs and the metallic localized edge states of z-GNRs (see section 1.3, Figure 1.8) [14, 15, 18, 22, 25, 26].

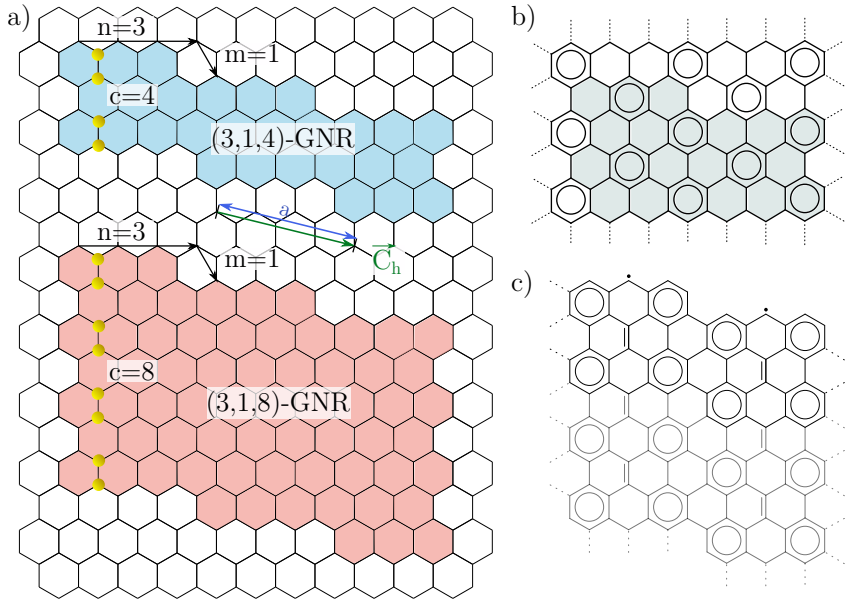

Figure 4.1: a) Notation for (3,1,4) and (3,1,8)-GNR. b) Graphene dense network of Clar sextets with (3,1) edge structure coloured in grey. c) Clar formula for (3,1) graphene edge structures.

Following the notation (n, m, c) for ch-GNR proposed in section 1.3, in this chapter we will focus on the (3,1,4)- and (3,1,8)-GNRs (Figure 4.1a). These two GNR structures have a common chiral translational vector $\vec{C_h}$ (represented with a green arrow in Figure 4.1a, see eq. 1.7) defined as

$$\vec{C_h} \equiv (3, 1) \tag{4.1}$$

but differ in the width of the ribbon. We adopt the number of carbon atoms across the ribbon (c) to measure the width of the ribbon. To describe the length we will refer to the number of precursor units (N), which in nanometers is equivalent to the distance between two monomers in the direction of $\vec{C_h}$, hereafter $a = c_{(3,1)} = 0.887$ nm (see eq. 1.8, blue arrow in Figure 4.1a). Based

on Clar's theory we can qualitatively predict the electronic structure for (3,1) edges (see section 1.3). Figure 4.1b,c shows how a ribbon with (3,1) edges requires to have unpaired electrons along the chiral edges to recover the graphene dense network of Clar sextets. As occurs for pure zig-zag edge structures (Figure 1.6f in section 1.3), the presence of these radicals underpins the edge states at the edge and suggests that (3,1)-GNRs will show spin polarization.

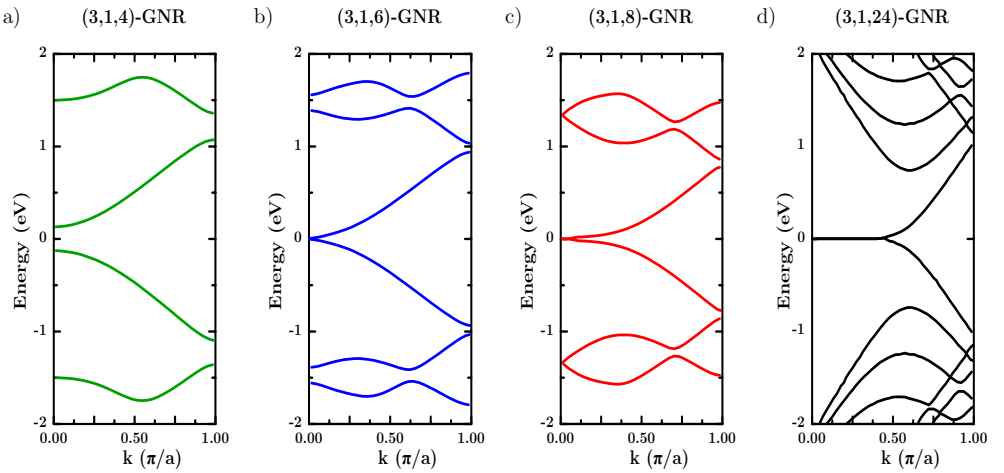

Figure 4.2: Electronic band structure for (3,1)-GNR of widths $c = 4$ (a), $c = 6$ (b), $c = 8$ (c) and $c = 24$ (d). Adapted from refs. [27] (a-c) and [18] (d).

The tight-binding (TB) electronic structure of infinitely long (3,1)-GNRs has been reported for ribbons of different widths (c). This theoretical method is briefly explained in section 1.3 for the simplest possible parametrization. In Figure 4.2 we show the published TB band structures calculated for (3,1)-GNRs with c values between 4 and 24 [18, 27, 126]. We should remark here that both, conduction and valence band (CB and VB), display dispersive behaviour, and that the zero-energy metallic edge state (around $k = 0$) becomes gapped for narrow (3,1)-GNRs. The band gap opening appears due to the interactions between its edges in narrow (3,1)-GNRs (between $c = 6$ and $c =8$) and becomes negligible when the ribbon is wide enough [14, 27, 129, 130]. TB calculations take these interactions into account through the hopping integral term, t (see eq. 1.1 and 1.2), which is defined as the overlap between electronic orbitals of neighboring atoms. The hopping integral strongly depends on the bonding distances among carbons, which may differ as a function of the atom environment, bond order, etcetera. These differences are found, for example, between edge carbons passivated by hydrogen atoms and bulk-like carbons in the middle of the GNR [126]. To obtain better approximations, TB calcula-

tions might include different hopping parameters along the edges and between longer range neighboring carbons [21].

The calculated TB band structures shown in Figure 4.2 correspond to infinitely long (3,1)-GNRs (with optimized hopping integrals between different carbon pairs), and appear as a result of the electron confinement of graphene in the dimension perpendicular to $\vec{C_h}$. The study of real finite GNRs can be qualitatively understood with the idea of a subsequent confinement effect, this time along the direction of $\vec{C_h}$, i.e., the ribbon axis. This confinement will affect the energy states at the chiral edges, which are highly localized there due to the high density of zig-zag sections [15, 17, 126, 131]. To describe the electronic structures of the edge states in finite size ch-GNRs, the particle in a box (PIB) model seems like a good approximation. The GNR is described in this model as a 1D electron system and the shorter terminal edges of the ribbon as the walls of the box. Applying the PIB model to the calculated TB band structures with dispersion relations $E(k)$ (Figure 4.2), one obtains PIB energies ($E(k_j)$) and associated wave functions $\psi_j(x)$ compatible with the boundary condition of having nodal points at the walls. Consequently, they are naturally dependent on the length of the ribbon ($L = N \cdot a$) as

$$\psi_j(x) = A_j e^{ik_j x} \quad \text{where} \quad k_j = \frac{j}{N}\left(\frac{\pi}{a}\right) \tag{4.2}$$

where x is measured along the direction of $\vec{C_h}$.

While the dispersion of (3,1)-GNRs electronic bands has been studied both theoretically and experimentally as a function of the width [27], the effect of finite lengths has not been systematically addressed. In this chapter, we try to bridge the gap between the studies of infinite and finite (real) (3,1)-GNRs electronic structures. In the following section, we first show the OSS procedure to obtain (3,1)-GNRs of widths $c = 4$ and $c = 8$ on Ag(001). Then, in sections 4.3.1 and 4.3.2 we determine the electronic structure of (3,1,4)- and (3,1,8)-GNRs with N between 2 and 16 to test their viability for organic electronic nano-devices, and assess the validity of prevailing theoretical models to predict the electronic properties of real GNRs.

4.2 Synthesis of chiral graphene nanoribbons

For the synthesis of atomically perfect GNRs it is important to understand and control the factors that steer any OSS process: the design of the precursor geometry, the substrate catalytic effect, the kinetics of the reaction and the influence of external species. The geometry of the precursor is clearly the primary factor, while the others can be tuned during the optimization of the samples and will be discussed later for each GNR.

As mentioned above, we synthesized ch-GNR with the axial growth direction following the vector $\vec{C_h}$ = (3, 1) (see Fig. 1.7 in section 1.3 and Fig. 4.1). With this purpose, the design of the precursor molecule should agree with certain requirements. In order to obtain GNRs with $n = 3$, the precursor molecules should have one anthracene in length, whilst the number of linked anthracene units will determine the width of the GNR (c). To obtain the chiral edges, the geometry of the precursor needs to be chiral. In order to have $m = 1$ GNRs, the C-C coupling should be between *meta* carbons, which fixes the sites of the halogens required for the Ullmann coupling reaction [13]. Considering these requirements, the designed precursor molecules to grow (3,1)-GNRs are 2,2'-dibromo-9,9'-bianthracene (precursor 1) and 2",3'-dibromo-9,9':10',9":10",9"'-quateranthracene (precursor 2), whose chemical structures are presented in Figure 4.3. Both precursor molecules were synthesized and purified by in solution techniques by the research group of Diego Peña at the University of Santiago de Compostela.

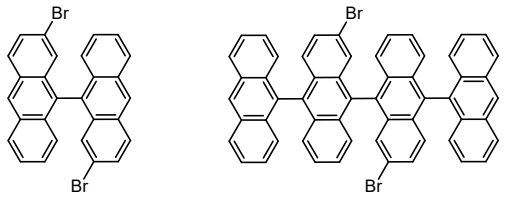

Precursor 1 Precursor 2

Figure 4.3: Precursor molecules for the synthesis of (3,1,4)-GNRs (precursor 1) and (3,1,8)-GNRs (precursor 2).

4.2.1 Synthesis of (3,1,4)-GNR

We use 2,2'-dibromo-9,9'-bianthracene, hereinafter precursor 1 (Fig. 4.3) as molecular precursor to synthesize (3,1,4)-GNRs on Ag(001). Figure 4.4a summarizes the steps of the synthetic pathway followed.

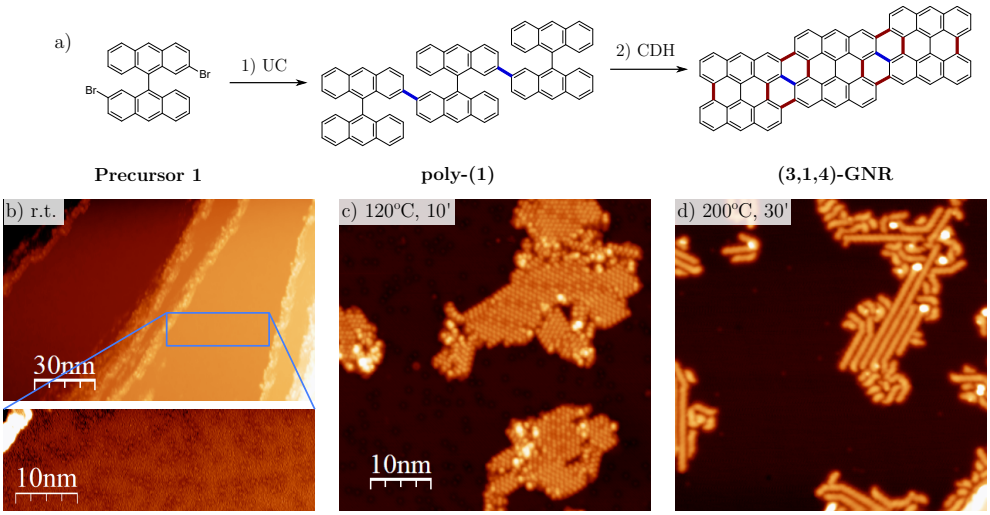

Figure 4.4: a) Synthesis pathway of (3,1,4)-GNR: polymerization of precursor 1 by UC and cyclodehydrogenation (CDH) to obtain the (3,1,4)-GNR. New C-C bonds are represented in blue (UC) and red (CDH). Representative surveys of the samples obtained after evaporation of precursor 1 on Ag(001) held at room temperature (0.5 V, 10 pA) (b), after annealing at 120 °C for 10 minutes (0.5 V, 10 pA) (c) and after annealing at 200 °C for 30 minutes (0.3 V, 10 pA)(d).

First, precursor 1 is sublimated from a home-made mini-UHV evaporator (see section 2.5.3) onto a clean Ag(001) single crystal held at room temperature. When the molecules reach the metallic surface, the bromine atoms dissociate from the molecule (Fig. 4.4b) and the radical precursor molecules tend to cluster at the edges of silver terraces. Then, the Ullmann coupling reaction (UC) is induced by annealing the sample at 120 °C for 10 minutes. After this time, we distinguish islands of self-assembled chains of precursor 1 (Fig. 4.4c).

A closer look into the chains of precursor 1 is presented in Figure 4.5 together with a height profile taken along the chain axis. The zig-zag protrusions observed have an average value of periodicity of 8.6 ± 0.1 Å, which is in agreement with the periodicity values reported for the covalent polymer (poly-(1) in Fig. 4.4a) [123]. From this observation we know that metal-organic intermediates are unstable on Ag(001) at 120 °C, and the UC directly leads to the polymer.

The (3,1,4)-GNRs fully cyclodehydrogenated are obtained after annealing the sample at 220 °C for at least 30 minutes (Figure 4.4c). As shown in Figure 4.5d-e, with shorter annealing times at the same temperature, we obtain poly-(1) chains partially dehydrogenated.

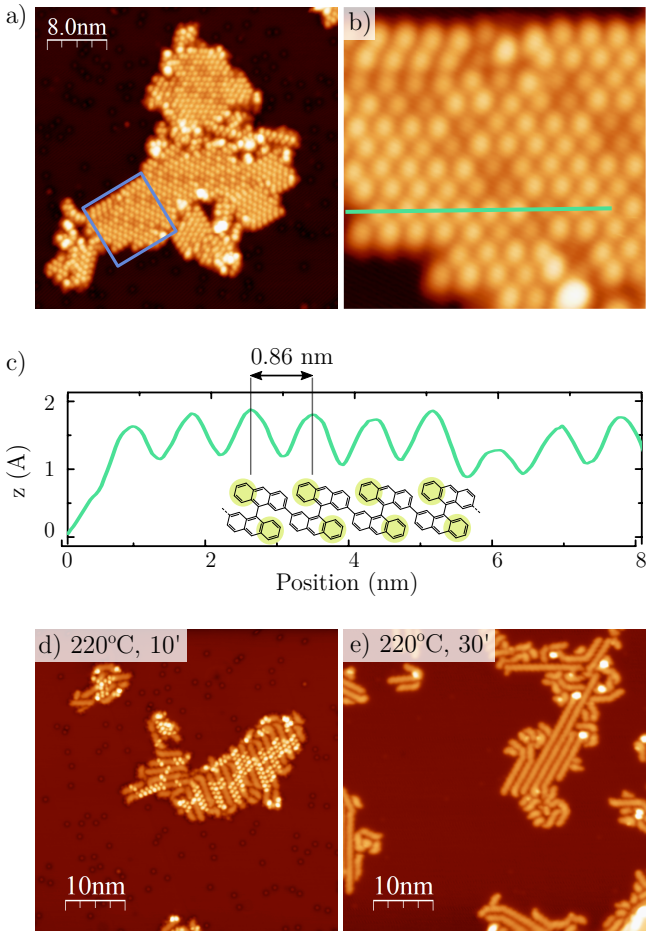

Figure 4.5: a) STM topography image of an island of poly-(1) chains on Ag(001) (0.5 V, 1 pA). b) Zoom in on the poly-(1) chains inside the blue square shown in a (0.5 V, 1 pA). c) Topography profile of the poly-(1) marked with a green line in b. In the schematic model of poly-(1) included in c, the protruding rings observed in b are highlighted in green. d) Poly-(1) chains partially cyclodehydrogenated obtained after 10 minutes of annealing (0.5 V, 100 pA). e) (3,1,4)-GNRs on Ag(001) obtained after annealing for 30 minutes (0.5 V, 100 pA).

4.2.2 Synthesis of (3,1,8)-GNR

To synthesize (3,1,8)-GNRs on Ag(001) substrate, we use compound 2 (Figure 4.3) as molecular precursor. In Figure 4.6a we show the scheme of the synthesis pathway as well as representative surveys of the samples obtained during the preparation of (3,1,8)-GNRs on Ag(001).

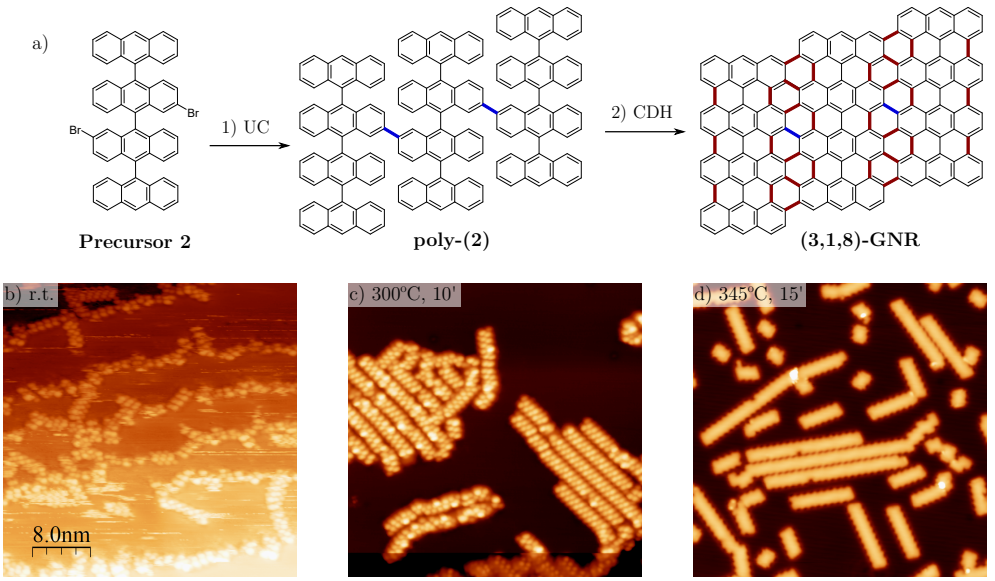

Figure 4.6: a) Synthesis pathway of (3,1,8)-GNRs: polymerization of precursor 2 by UC reaction and CDH to obtain the final GNR. New C-C bonds are represented in blue (UC) and red (CDH). Representative surveys of the samples obtained after evaporation of precursor 2 on Ag(001) (image recorded at room temperature, 1 V, 60 pA) (b), after annealing at 300 °C for 10 minutes (0.5 V, 50 pA) (c) and after annealing the sample at 345 °C for 15 minutes (0.3 V, 10 pA) (d).

Precursor 2 is first sublimated from a mini-UHV evaporator (see section 2.5.3) onto a clean Ag(001) crystal held at room temperature. When precursor 2 reaches the surface, the UC takes place right away and the samples show short chains, known as oligomers, close to the edges of silver terraces (Figure 4.6b). Upon annealing to 300 °C (Figure 4.6c), we distinguish a clear change in the morphology of the sample with longer and ordered chains in islands. Measuring the distance between the protrusions shown in Figure 4.7, we obtain an an average periodicity value of 8.2 ± 0.1 Å, which corresponds with the expected periodicity of poly-(2) chains [123].

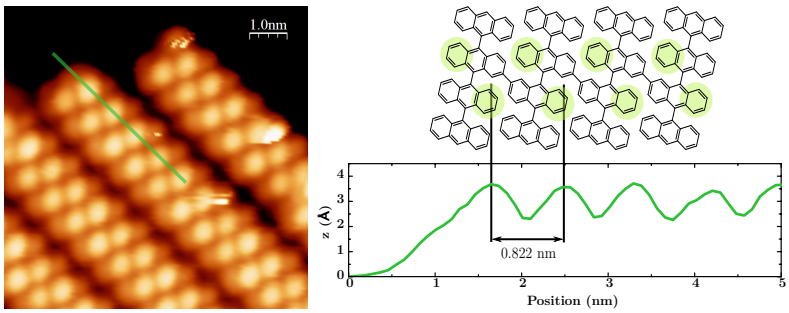

Figure 4.7: a) STM topography image of an island of poly-2 chains on Ag(001) obtained after annealing the sample at 300 °C for 10 minutes (0.5 V, 50 pA). b) Topography profile of poly-(2) marked with a green line in a. c) Schematic model of poly-(2) represented with the high parts observed in a highlighted in green.

As in the case of (3,1,4)-GNRs, soft annealing processes of poly-(2) samples lead to partial cyclodehydrogenation (CDH) of the polymeric chains, but annealing above certain temperature the fully planarized (3,1,8)-GNRs form. In Figure 4.8 we show STM images of the samples obtained after different annealing processes of a poly-(2) sample until (3,1,8)-GNRs are fully planarized.

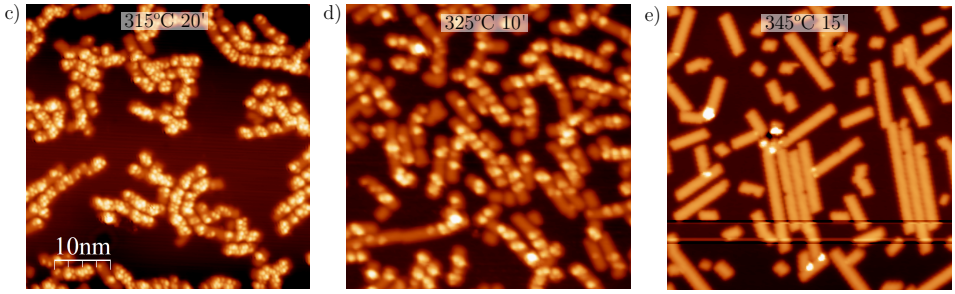

Figure 4.8: STM topography images of representative samples obtained during the preparation of (3,1,8)-GNRs on Ag(001). Chains of poly-(2) partially cyclodehydrogenated after heating the sample up to 315 °C for 20 minutes (a) and 325 °C for 10 minutes (b). c) (3,1,8)-GNRs obtained after complete cyclodehydrogenation at 345 °C for 20 minutes.

4.2.3 Structural characterization of ch-GNRs

To confirm that the (3,1,4)- and (3,1,8)-GNRs structures are free of defects, we acquired high resolution STM images. The images recorded with sharp metal tips or CO tips allow us to distinguish bites or protrusions in the GNRs, which are related with atomic defects in the otherwise nominal graphene backbone. In the STM images recorded in constant current mode with a CO tip, an intramolecular structure is resolved, although the honeycomb structure of the GNRs cannot be clearly visualized. In Figure 4.9 we include examples of high resolution STM images recorded using sharp metal and CO tips to show the difference between defective and defect free ch-GNR structures.

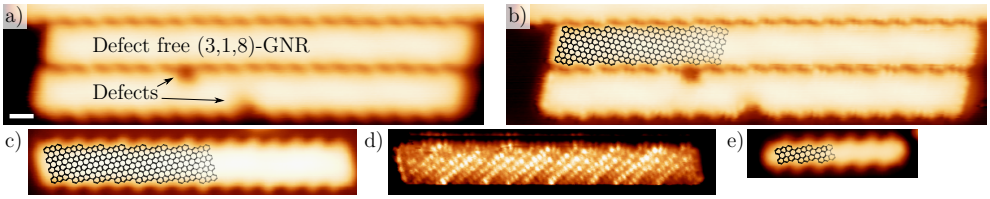

Figure 4.9: High resolution STM images of synthesized ch-GNRs. Constant current images recorded with a metal tip (a) and CO-tip (b) of a pair of N = 19 (3,1,8)-GNRs with and without bites at the chiral edges (SP: 0.1 V, 100 pA). c) Constant current STM image of a defect free N = 14 (3,1,8)-GNR recorded with a metal tip, SP: 50 mV, 50 pA. d) Constant height STM image of the same GNR as c recorded with CO tip, SP: 2 mV. e) Constant current STM image of a defect free N = 6 (3,1,4)-GNR, SP: 0.5 V, 100 pA. Scale bar in a: 1 nm.

4.3 Electronic structure of chiral GNRs

The synthesized ch-GNRs on Ag(001) have been characterized by STS point spectra along the ribbon and recording conductance maps at the relevant bias voltages to extract the spatial distribution of the Local Density of States (LDOS). To get rid of the artificial tip contributions to the dI/dV spectra, we show in all the graphs the resulting STS spectra once the background of the bare Ag(001) surface nearby is subtracted, taking special care that additional spectroscopic features are not introduced by this treatment.

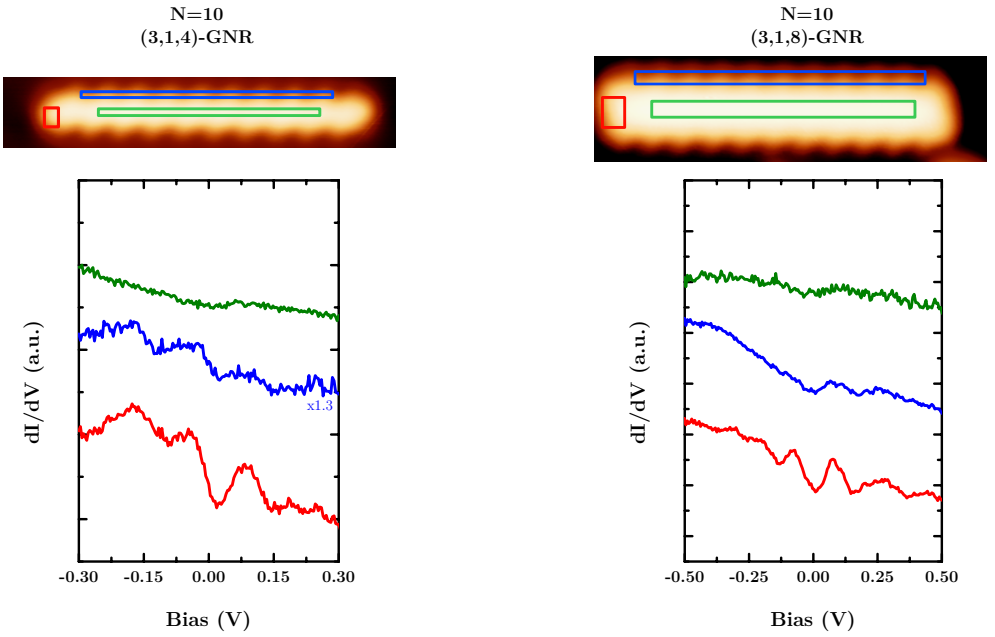

Figure 4.10: STM images of (3,1,4)- and (3,1,8)-GNRs with N = 10 (SP: 0.5 V, 100 pA) and STS spectra recorded on them. The squares indicate the zone where the spectra were recorded: on the armchair edges (red), along the chiral edges (blue) and in the middle of the ribbons (green). STS SP: 0.5 V, 100 pA; V_{mod}= 4 mV.

The STS spectra of both (3,1,4) and (3,1,8)-GNRs exhibit certain similarities, presumably attributed to the common edge structure. For both widths, we observe that the spectra recorded in the middle of the ribbon do not show any feature, in contrast with clear peaks recorded in the spectra taken over the edges. HOMO (*H1*) and LUMO (*L1*) discrete states display the same periodicity but their patterns occupy precursors in an interleaved manner. This is in agreement with the localization effects produced by the presence of edges, giving rise to the strongest fingerprints of discretized states at these positions [118,

132]. In Figure 4.10 we show the average of STS spectra recorded on (3,1,4)- and (3,1,8)-GNRs with N = 10 as representative examples. The squares included in the topography images denote the zones where the point spectra were recorded: on the armchair edges (red), along the chiral edges (blue) and in the middle of the ribbons (green).

The LDOS spatial distribution becomes more evident when we record linear grids of STS point spectra along the GNRs. In Figure 4.11 we show a stack plot of $\mathrm{d}I/\mathrm{d}V$ versus position recorded on the previously shown (3,1,4) and (3,1,8)-GNRs with N = 10. These plots capture the main features of the peak intensity distribution throughout the ribbon:

1. They are unnoticeable at the central part of the ribbon.
2. At the armchair edges, the most distinct and intense peaks are those around the Fermi level.
3. The same features are recovered at some particular positions of the phenolic kinks of the chiral edges, although they are strongly suppressed with respect to the armchair edge.

In the following sections, we will present a detailed electronic characterization of ch-GNRs as a function of the length of the ribbon (N).

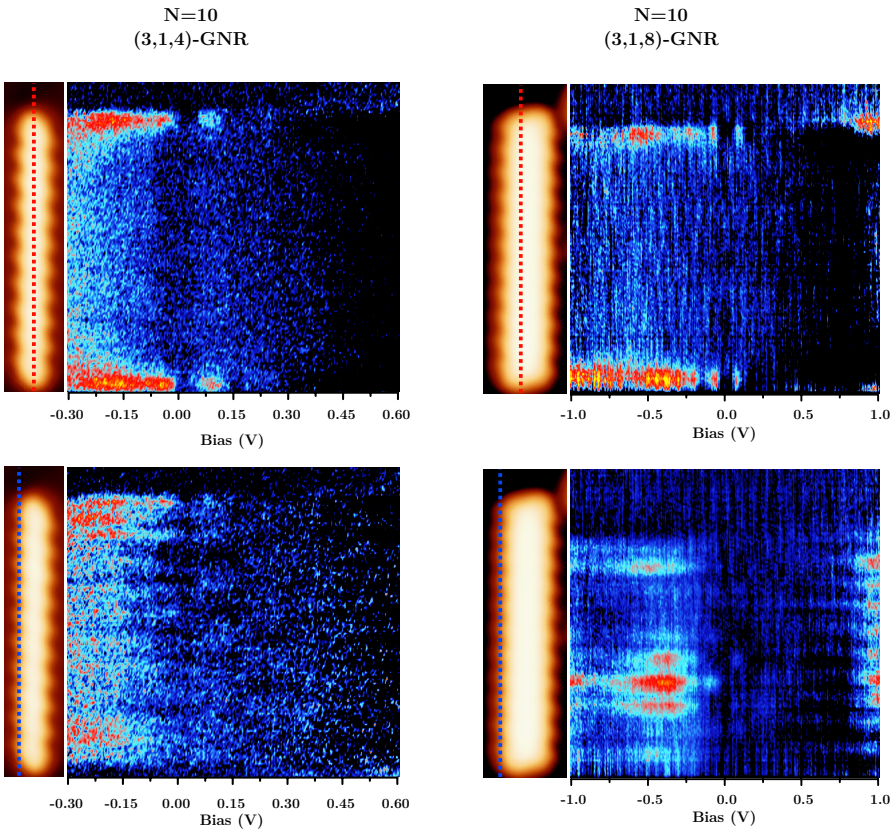

Figure 4.11: Stack plots of STS spectra versus position recorded on (3,1,4)- and (3,1,8)-GNRs on Ag(001) with N = 10 along the dotted lines shown in the STM topography images included at the left of each plot (SP: 0.5 V, 100 pA). STS SP: 0.5 V, 100 pA; V_{mod}= 4 mV.

4.3.1 Electronic structure of (3,1,4)-GNRs

We have characterized the electronic properties of (3,1,4)-GNRs with varying N by point spectra STS and dI/dV maps at the bias voltages of interest.

The dI/dV point spectra shown in Figure 4.12 were acquired over defect free (3,1,4)-GNRs with lengths between N = 2 and N = 13. All STS spectra show a characteristic pattern of three peaks that we named as *L1*, *L2* and *L3* and whose corresponding energies are listed in Table 4.1. The position of these peaks is observed to shift as a function of the length, being lower the energy differences ΔE_{L12} (defined as $|E_{L2} - E_{L1}|$) and ΔE_{L23} ($|E_{L3} - E_{L2}|$) as the length of the GNR increases.

N p.u.	**Energy (eV)**			Δ_{L12}	Δ_{L23}
	L1	*L2*	*L3*	(eV)	(eV)
2	-0.88	-0.34	0.00	0.53	0.34
3	-0.20	0.11	0.43	0.31	0.30
4	-0.17	0.03	0.23	0.20	0.21
5	-0.12	0.16	0.36	0.28	0.20
6	-0.10	0.06	0.27	0.16	0.21
8	-0.08	0.07	0.22	0.15	0.16
9	-0.13	0.00	0.15	0.13	0.15
10	-0.05	0.09	0.23	0.14	0.14
12	0.00	0.12	0.22	0.12	0.10
13	-0.03	0.07	0.20	0.10	0.13

Table 4.1: Peak energies of the states observed in STS spectra of Figure 4.12a and energy differences between them designated as Δ_{L12} and Δ_{L23} gaps (see text). The choice of *L2* peak to compose this table is based on the identification of its characteristic spatial distribution (see below), or by its central position in individual spectra in the case where dI/dV maps were not retrieved.

To obtain the spatial distribution of the corresponding molecular states, we recorded dI/dV maps of each (3,1,4)-GNR at representative energy values. In Figure 4.12b and 4.12c we show the dI/dV maps recorded on the N = 10 and N = 12 (3,1,4)-GNRs to illustrate the experimental LDOS distribution. The brightness at the armchair edges dominates over the rest of the molecule and along the chiral edge of the ribbons it is possible to distinguish a modulation of the intensity with a period different from the structural one. These features are also recognizable in calculated conductance maps of LUMO states obtained for a free standing N = 6 (3,1,4)-GNR shown in Figure 4.13 [126]. In this figure,

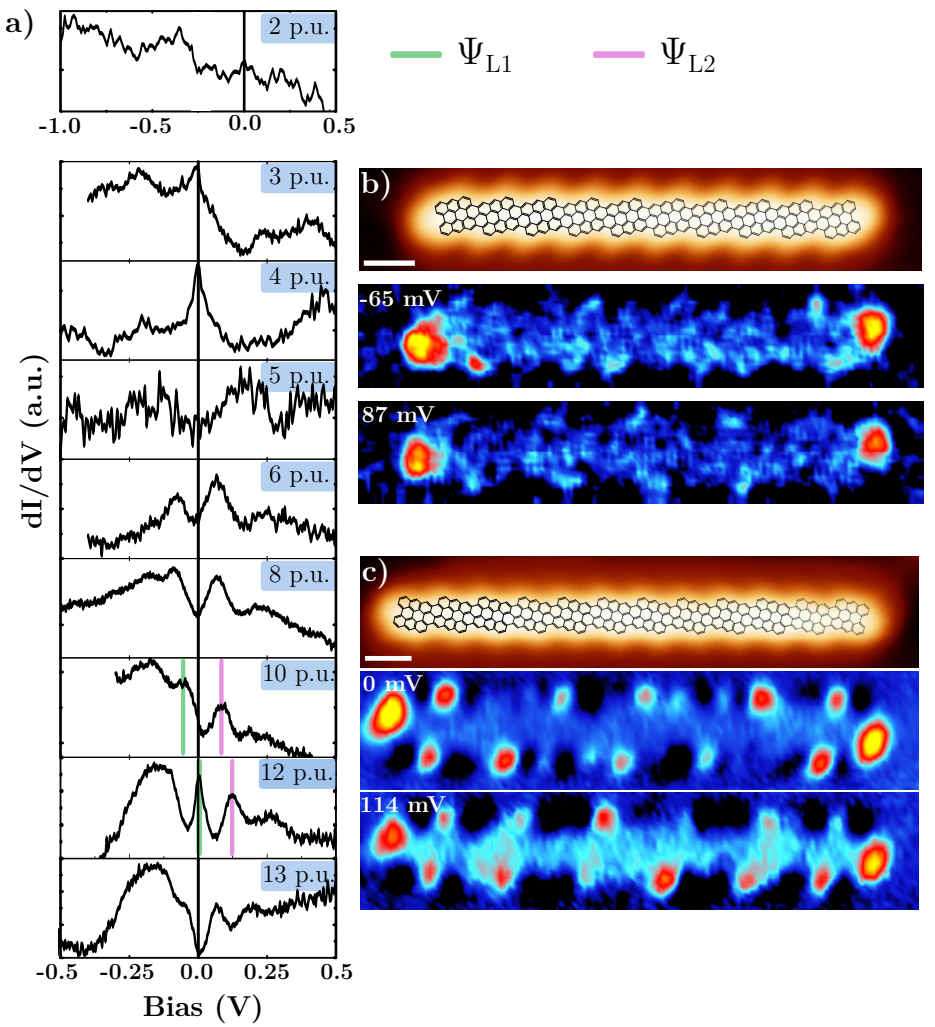

Figure 4.12: Electronic characterization of (3,1,4)-GNRs. a) Representative STS point spectra recorded on the edges of (3,1,4)-GNRs of lengths between N = 2 and N = 13. STM topography images of N = 10 (b) and N = 12 (c) (3,1,4)-GNRs and their associated differential conductance maps recorded at the bias voltages for which STS point spectroscopy peaks were found (colored lines in a). STS and STM images set point: 0.5 V, 100 pA; V_{mod}= 4 mV. White scale bars: 1 nm.

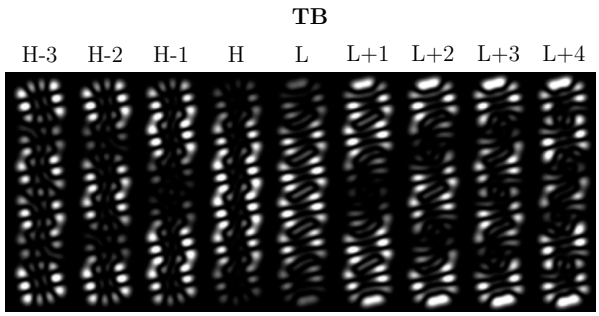

Figure 4.13: TB simulated differential conductance maps of the states from HOMO-3 to LUMO+4 of a N = 6 (3,1,4)-GNR. Copied from ref. [126].

the theoretical maps of the LUMO to LUMO+4 states exhibit a localization of the intensity at chiral edges with periodic valleys, nodes and cusps along the ribbon longitudinal axis. Furthermore, these LUMOs display the most intense brightness at the armchair edges, in agreement with our experimental data, and that it is completely absent in the HOMO and lower energy states. This comparison suggests that the states we access by STS correspond to the LUMO or higher energy states of the charge neutral (3,1,4)-GNRs. For that reason we chose the notation *L1*, *L2* and *L3*.

The observation of unoccupied states of (3,1,4)-GNRs below the Fermi energy implies the existence of an electron transfer from the Ag(001) surface, which is in agreement with the results published for (3,1,6)-GNRs on Ag(111) curved crystal at the {100}-oriented microfacet [54]. The lower work function of the Ag(001) surface (see section 5.4) compared to the Au(111) surface, favours the electron transfer from the substrate to the GNRs. It is worth mentioning that conduction band states of long (3,1,4)-GNRs are not yet described in the literature due to the difficulties to access them in finite GNRs synthesized on Au(111). In our case, the electron transfer from the Ag(001) substrate produces the shift of the conduction band below the Fermi level, facilitating the access to these unoccupied states and allowing us to study them in detail.

N p.u.	**5**	**6**	**8**	**10**
Ψ_{L2} p_{exp} (a)	1.96	2.04	2.04	1.99
Ψ_{L1} p_{exp} (a)	3.06	2.94	2.93	2.91

Table 4.2: Intensity periodicities extracted from $\mathrm{d}I/\mathrm{d}V$ maps recorded at corresponding Ψ_{L1} and Ψ_{L2} energy values obtained in STS point spectra (Figure 4.12). Estimated error $\pm$ 0.03 a.

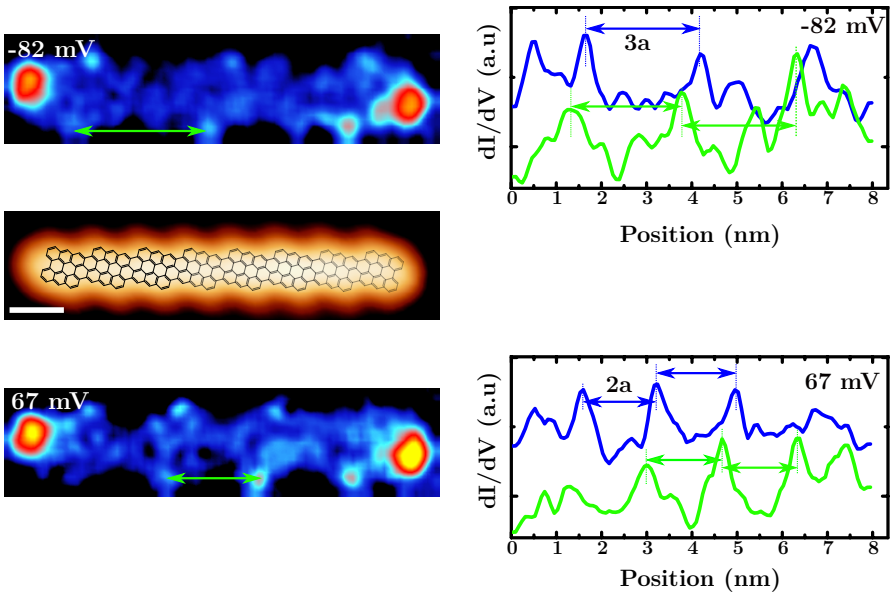

Figure 4.14: Differential conductance maps recorded on a N = 8 (3,1,4)-GNR with their corresponding height profiles along the bottom (green) and top (blue) chiral edges.

Since all the states that we access are apparently empty states of the charge neutral ribbon, transforming the real space periodicities along the ribbon into k-space, one would obtain the allowed k values of the discretized (3,1,4)-GNR conduction band, as for instance the ones predicted by the PIB model (eq. 4.2). In principle, from the set of E and k pairs, it is possible to extract the dispersion relation of the conduction band of (3,1,4)-GNRs. When the ribbon is long enough as to accommodate two or more nodes, we can clearly retrieve a periodicity (see Figs. 4.12b-c), but this is not possible for shortest ribbons or $\mathrm{d}I/\mathrm{d}V$ maps with poor contrast. In Figure 4.14 we show two additional examples of $\mathrm{d}I/\mathrm{d}V$ maps recorded on a N = 8 (3,1,4)-GNR, with the corresponding profiles taken at both chiral edges where the periodicities are visible. The prevailing periodicities obtained from $\mathrm{d}I/\mathrm{d}V$ maps in all of our studied ribbons are summarized in Table 4.2. The experimental values yield the striking conclusion that boundary conditions imposed by the finite length of the GNRs restrict the eigenstates to have periodicities satisfying $p_n = n \cdot a$ (being $a = c_{(3,1)}$ the lattice constant of the chiral edge). These periodicities correspond to $k_{exp} = \pi/p_{exp}$. They are thus independent of the ribbon's length, in sharp contrast to the behaviour of k_j expected for the conventional PIB approximation (eq. 4.2).

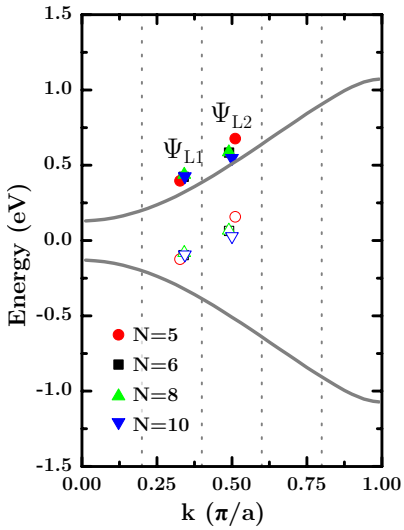

Figure 4.15: Experimental E(k_{exp}) with energy values obtained from STS and k_{exp} values from the intensity periodicity observed in the dI/dV maps (open symbols). Grey lines are TB calculations of valence and conduction bands obtained from ref. [27] and dotted vertical lines represent the expected k_j values for a N = 5 (3,1,4)-GNR (see Eq. 4.2). Filled symbols represent the $E(k_{exp})$ values increased by 0.52 eV.

In Table 4.2 it is readily seen that the occupied peak nearest to Fermi level ($L1$) exhibits a wave form (Ψ_{L1}) with strong $k = (1/3)(\pi/a)$ contribution, whereas for the next peak ($L2$), which coincides with the central peak in our point spectra) its Ψ_{L2} is $k = (1/2)(\pi/a)$. In Figure 4.15 we present the obtained $E(k_{exp})$ values (open symbols) together with the VB and CB (grey lines) from previously mentioned TB calculation of an infinitely long (3,1,4)-GNRs (Figure 4.2a [27]). The deviation of $E(k_{exp})$ from the theoretical range of energy of the CB is close to 0.5 eV, which agrees with the 0.52 eV value recently reported for charge transfer processes found from silver surfaces to (3,1,6)-GNRs [54]. The filled symbols in Figure 4.15 represent the $E(k_{exp})$ values increased by 0.52 eV, whose energy range and slope fits better now with the TB calculations [27]. Finally, the vertical dotted lines included in Figure 4.15 represent the k_j values for a N = 5 (3,1,4)-GNR. As pointed out above, the discrepancy between expected k_j's in the PIB model and the k_{exp} values evidence the failure of the PIB model to predict the eigenstates and eigenenergies of finite size (3,1,4)-GNRs.

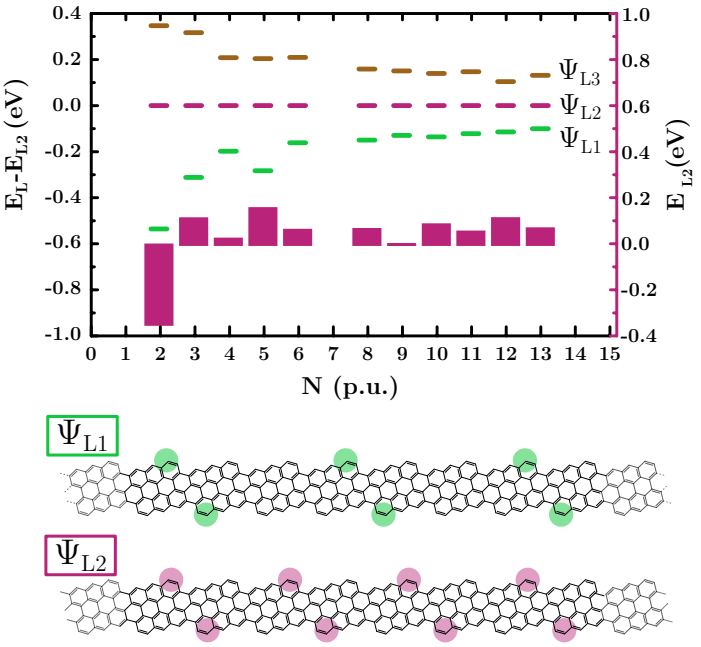

Figure 4.16: Energies of the Ψ_{L1-3} states respect to Ψ_{L2} as a function of the (3,1,4)-GNRs length and the corresponding wave function structures drawn GNR much longer than the interlobe period.

The dominant modulations of the intensity extracted from the dI/dV maps point to wave functions of the type of bright spots every $p = 3 \cdot a$ (Ψ_{L1}) and $p = 2 \cdot a$ Ψ_{L2} for *L1* and *L2* states respectively. Attending to the order of appearance of the peaks for increasing bias we assign these wave functions to the peak energies observed by STS in shorter (3,1,4)-GNRs (N $<$ 6) where periodicities are not distinguishable. In Figure 4.16, we represent all the states energy values respect to the L2 energy state, to highlight the gradual closing of the gaps as the length of the ribbon increases. Note that in an infinite ribbon without armchair terminations, these wave functions must become quasiparticle like (eq. 4.2) and the gaps between consecutive allowed energies of the conduction band, in very long ribbons, should tend to zero. In the bottom panel of Figure 4.16, we show a sketch of the LDOS repetition pattern of long but finite (3,1,4)-GNRs, as derived from the dominant periodicities observed in dI/dV maps (Table 4.2). Figure 4.16 also shows with bars a variation in energy of *L2* state around the Fermi level. This fluctuation is not related with N and we ascribe it to variations in the charge transfer that are sensitive to ribbon adsorption geometry.

4.3.2 Electronic structure of (3,1,8)-GNRs

Following the same methodology described in the previous section, we have characterized the electronic properties of defect free (3,1,8)-GNRs on Ag(001) by recording STS point spectra on ribbons with lengths between N = 3 and N = 16, together with dI/dV maps at bias voltages of interest.

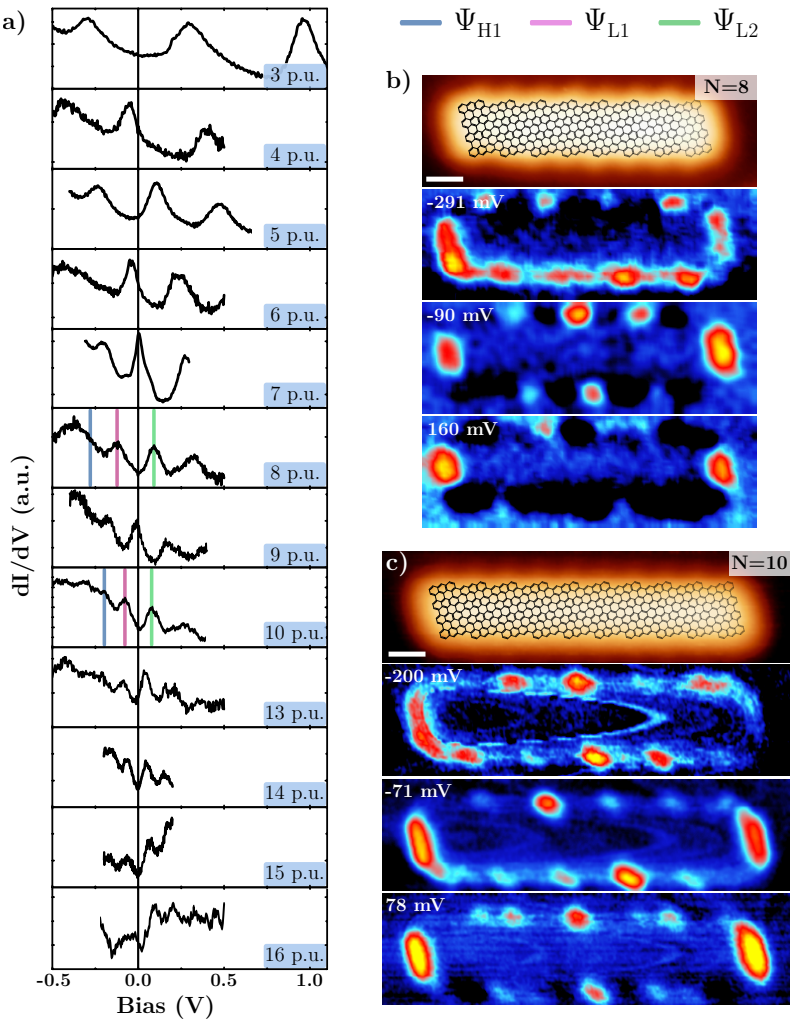

Figure 4.17: Electronic characterization of (3,1,8)-GNRs. a) Representative STS point spectra recorded on (3,1,8)-GNRs of lengths between N= 3 and N = 16. STM topography images of N = 8 (b) and N = 10 (c) monomers long (3,1,8)-GNRs together with simultaneous differential conductance maps recorded at the bias voltages of the spectroscopy peaks (colored lines in a). STM and STS set point: 0.5 V, 100 pA. White scale bars: 1 nm.

In Table 4.3 we summarize all the energy values of the peaks found in STS spectra, together with the energy differences between them. We define Δ_{HL} as $|E_{L1} - E_{H1}|$ and Δ_{L12} as $|E_{L2} - E_{L1}|$. An overview of the point spectra STS recorded on defect-free (3,1,8)-GNRs of different lengths is shown in Figure 4.17a.

N p.u.	**Energy (eV)**			Δ_{HL}	Δ_{L12}
	Ψ_{H1}	Ψ_{L1}	Ψ_{L2}		
2	-0.96	-0.09	1.00	0.87	1.09
3	-0.30	0.30	0.97	0.59	0.67
4	-0.43	-0.05	0.39	0.38	0.44
5	-0.25	0.11	0.41	0.38	0.30
6	-0.35	-0.04	0.23	0.31	0.27
7	-0.16	0.05	0.21	0.17	0.20
8	-0.08	0.07	0.22	0.15	0.16
9	-0.17	0.00	0.16	0.17	0.16
10	-0.17	-0.03	0.16	0.14	0.15
11	-0.15	-0.02	0.12	0.13	0.15
13	-0.09	0.04	0.16	0.13	0.12
14	-0.12	-0.04	0.12	0.11	0.12
15	-0.08	0.04	0.15	0.11	0.11
16	-0.14	-0.03	0.07	0.11	0.10

Table 4.3: Peak energies of the states observed in STS spectra recorded on (3,1,8)-GNRs and energy differences between them designated as Δ_{HL} and Δ_{L1} gaps (see text). To compose this table *L1* has been taken as the central peak of our point spectroscopy curves in Fig. 4.17.

When we compare the point spectra and the $\mathrm{d}I/\mathrm{d}V$ maps (Figure 4.17b-c) with the data obtained on (3,1,4)-GNRs (Figure 4.12), we notice three similarities: the presence of at least three peaks around the Fermi level, the strong LDOS intensity at the armchair edges of certain occupied states and the periodic modulations along the chiral edges in the $\mathrm{d}I/\mathrm{d}V$ maps. To illustrate this point, we show in Figure 4.17b-c the $\mathrm{d}I/\mathrm{d}V$ maps recorded on N = 8 and N = 10 (3,1,8)-GNRs. We distinguish clear modulations of the intensity along the chiral edge of the GNRs with periodicity values of $p_{exp} \approx 2 \cdot a$ and $p_{exp} \approx 3 \cdot a$. These periodicities are recurrent for all GNRs with N > 6. There are, nonetheless, stark differences with respect to the phenomenology in (3,1,4)-GNRs which are already noticeable by comparing Figures 4.17b-c and 4.12b-c.

The first fully occupied peak below the Fermi level (labelled *H1*) does no longer display enhanced intensity at the armchair edges. According to the TB calculations in ref [126] (see Fig. 4.13) this is characteristic of the HOMO and HOMO-n states of the charge neutral ribbons. Consequently, we took the notation of *H1* for this lowest energy state in (3,1,8)-GNRs. Furthermore, we observe that the next two peaks display the same periodicity modulations of $p = 2a$ and $p = 3a$ as peaks *L1* and *L2* in (3,1,4)-GNRs, but they appear in the reverse order as a function of energy. The periodicity $p = 2a$ appears in the wave form of the central peak labelled *L1* (next peak after *H1* state), and the highest energy peak shows the $p = 3a$ modulation (labelled *L2*).

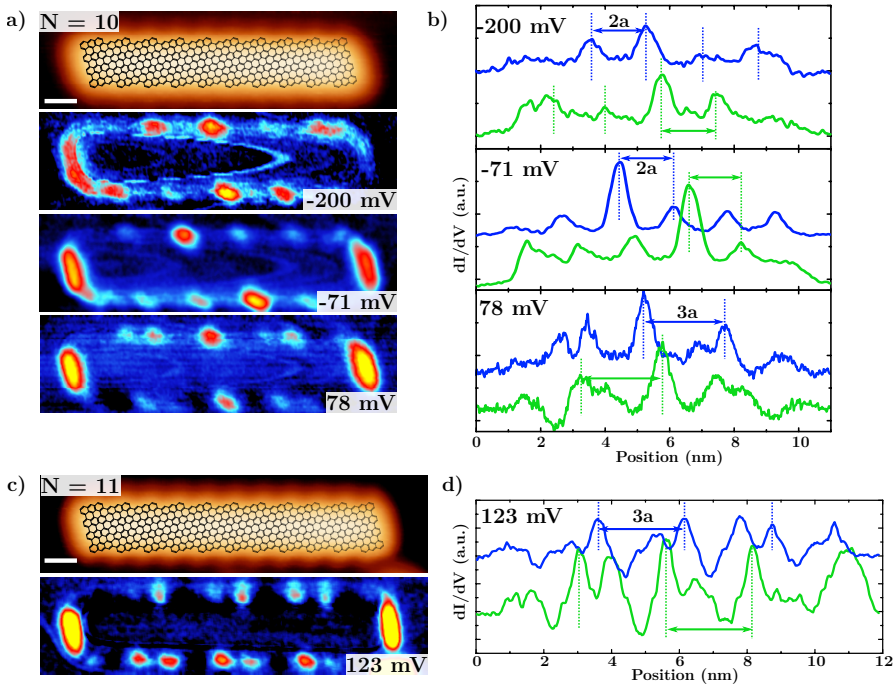

Figure 4.18: Differential conductance maps recorded on N = 10 (a) and N = 11 (c) (3,1,8)-GNRs with the corresponding intensity profiles along the bottom (green) and top (blue) chiral edges (b and d).

Figure 4.18 shows a quantitative analysis of the longitudinal profiles of the $\mathrm{d}I/\mathrm{d}V$ maps recorded on the N = 10 and N = 11 (3,1,8)-GNR along both chiral edges. We distinguish indeed the modulation periodicity $p_{exp} \approx 2 \cdot a$ in the lowest energy conductance maps of the N = 10, corresponding to *H1* and *L1* states. The spatial distribution in these two states (Ψ_{H1} and Ψ_{L1}) exhibits two significant differences. First, the intensity localized at the armchair edges is only evident for Ψ_{L1} (-71 mV and -90 mV $\mathrm{d}I/\mathrm{d}V$ maps for N = 10 and

N = 8 respectively). Second, the p_{exp} observed on the dI/dV maps show complementary nodal plane structures (the bright lobes in one dI/dV map come without intensity in the other). These differences also exists between the dI/dV maps recorded at -90 and -291 mV on a N = 8 GNR (Figure 4.17b).

In Figure 4.18 the dI/dV maps of assigned *L2* energy peaks recorded on N = 10 and N = 11 GNRs at 78 and 123 mV respectively show a common periodicity of $p_{exp} \approx 3 \cdot a$. In contrast to periodicities found on LDOS of *H1* and *L1* states, we observe in Ψ_{L2} two precursors involved in the periodic fluctuation of the intensity. This characteristic wave form is intrinsic of the *L2* states, but it is only noticeable in long ribbons, such us, N $\geq$ 8 (3,1,8)-GNRs. The dI/dV map recorded at 160 mV on the N = 8 (3,1,8)-GNR included in Figure 4.17b shows similar features, but the length of the ribbon is clearly not enough to properly appreciate the wave form.

In Table 4.4 we summarize all the periodicities found in dI/dV maps of (3,1,8)-GNRs.

N p.u.	**7**	**8**	**9**	**10**	**11**	**14**
Ψ_{H1} p_{exp} (a)		1.94	1.97	2.02	1.98	1.97
Ψ_{L1} p_{exp} (a)		1.99		1.97	1.96	1.91
Ψ_{L2} p_{exp} (a)	3.01	3.11	3.09	2.94	3.05	2.86

Table 4.4: Intensity periodicities extracted from dI/dV maps recorded at corresponding Ψ energy values obtained in STS point spectra (Figure 4.17). Estimated error $\pm$ 0.03 a.

In Figure 4.19 we represent the *H1*, *L1* and *L2* energies relative to *L1* as a function of the (3,1,8)-GNRs length, to highlight the smooth decrease of the energy gaps between the states as the length of the GNR increases, as occurred for narrower GNRs (Figure 4.16). The duplicated periodicities found in dI/dV maps recorded at *H1* and *L1* peaks are in agreement with our previous assignment of states based on the armchair intensities of their corresponding wave functions.

To sum up, we conclude that for all the lengths explored we have access to three states of (3,1,8)-GNRs which correspond to an HOMO state of the charge neutral ribbon (*H1*), and two unoccupied states of the neutral ribbon (LUMO) labelled as *L1* and *L2*, which feature the characteristic armchair brightness of LUMO states (Figure 4.2). The different periodicities found in the dI/dV maps of each state allow us to describe their wave form (Ψ). This assignment procedure for the states of (3,1,8)-GNRs can be extrapolated to

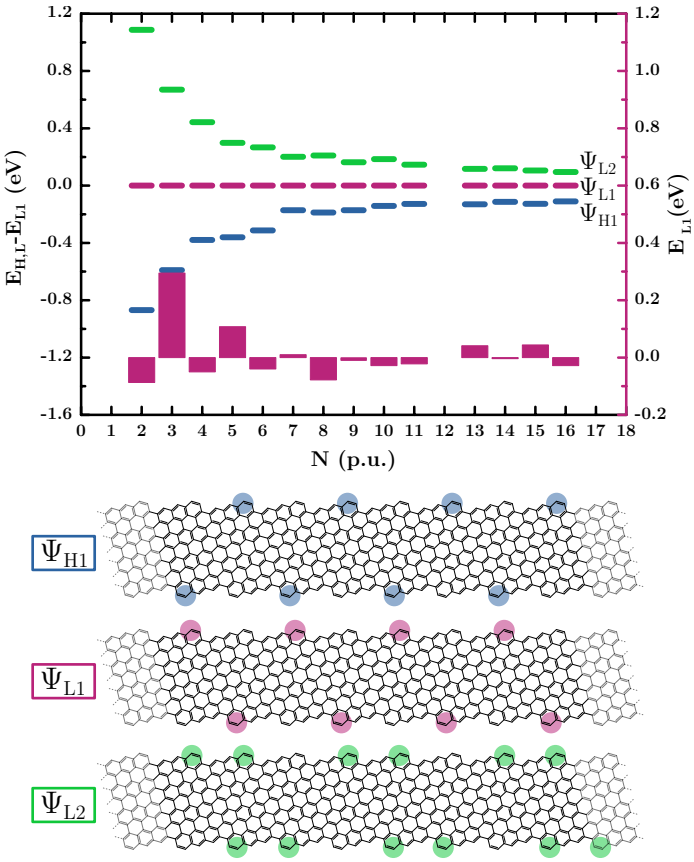

Figure 4.19: Energies of the *H1*, *L1* and *L2* states respect to *L1* as a function of the (3,1,8)-GNRs length. At the bottom panel we include the corresponding wave function structures drawn on (3,1,8)-GNR much longer than the interlobe periodicity.

other substrates. We will make use of this assignment to describe the electronic structure of (3,1,8)-GNRs adsorbed on MgO (Chapter 5).

4.4 Conclusions

Chiral graphene nanoribbons are promising graphene structures easier to synthesize than pure zig-zag edge GNRs, and at the same time, preserve the most interesting electronic property of these last ones: the presence of a localized 1D metallic edge state. In this chapter, we have reported the successful synthesis of (3,1)-GNRs on Ag(001) with $c = 4$ and $c = 8$, and lengths between N = 2 and N = 16; and their electronic characterization to unveil the correlation between the length of the ribbon and its electronic structure resulting from the discretization of the metallic edge state. In Figure 4.20 we represent the energy differences between states as a function of the length. This figure determine the potential applications of ch-GNRs in nanoelectronic devices. We find that longer ribbons with N > 10 display discretization gaps around Fermi level of about 0.1 eV, enclosed by electronic states with a typical full width at a half maximum (FWHM) of 0.05 eV, which means that for applications at room temperature ($k_B T = 0.025$ eV) they could be used mainly as 1D metallic wires. On the other hand, shorter ribbons present a more semiconducting character with wider gaps, which makes them excellent candidates to behave as atomic scale transistors provided that their charge state can be tuned by an external gate voltage (this will be the focus of section 6.3 in Chapter 6).

We have observed that (3,1,c)-GNRs are charged by the Ag(001) substrate, and, in the case of $c = 4$ GNRs we obtain a shift in energy of ≈ 0.50 eV to match with TB calculations of free standing ribbons. This increase is in agreement with the value reported for charge transfer from silver substrate to similar GNRs [54] and justifies the fact that most of the differential conductance maps show characteristic spatial distributions of discretized conduction band states [126]. The new alignment of the (3,1,c)-GNRs orbitals with respect to the Fermi level facilitates the study of states emerging from the conduction band of continuous ribbons, which is not possible on substrates with higher work function values.

From our results we can conclude that for both widths $c = 4$ and $c = 8$, all the gaps between molecular orbitals close asymptotically as the length of the GNR increases. Due to the fact that (3,1,c)-GNRs are charged by the Ag(001) substrate, we access to LUMO states. In the case of (3,1,4)-GNRs we access to *L1*, *L2* and *L3* states, and in the case of (3,1,8)-GNRs, to *H1*, *L1*, *L2* states. This difference comes from the fact that, for long ribbons, we find a LUMO-type state for (3,1,4)-GNRs at an energy of -0.1 eV, whereas in the same energy region a HOMO-type appears for (3,1,8)-GNRs. This suggests that the charge transfer depends on the width of the GNR, and then, for wider

ribbons the induced energy shift is smaller.

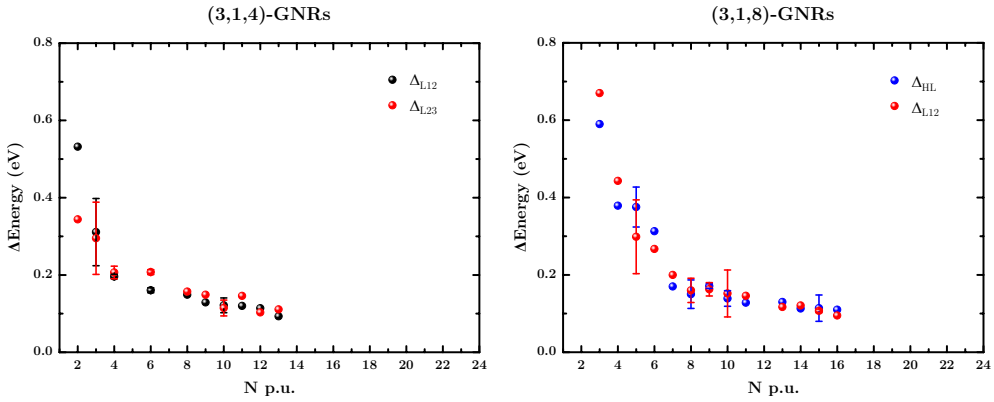

Figure 4.20: Evolution of Δ_{HL}, Δ_{L1} and Δ_{L2} gaps versus (3,1,c)-GNRs length (Tables 4.1 and 4.3). Error bars are obtained for same ribbons on different samples.

The tendency of Δ_{HL}, Δ_{L12} and Δ_{L23} gaps is shown in Figure 4.20. All of them have an asymptotic behaviour for which best fits are obtained for a limit of $\Delta = 0$, although longer GNRs need to be studied to confirm rigously this result. Particularly, asymptotic fits with limits $\Delta_{L12} = 0.09$ eV for (3,1,4)-GNRs and $\Delta_{HL} = 0.03$ eV for (3,1,8)-GNRs, provide a similar quality to the case of constraining to a gapless limit.

Note that the spatial distribution Ψ_{L2} along the edge (3,1,4)-GNRs (*L2* state, the second observable LUMO state) coincides with that of Ψ_{L1} for (3,1,8)-GNRs (*L1* state, the first observable LUMO). Therefore, Δ_{L23} gap of (3,1,4)-GNRs and Δ_{L12} gap of (3,1,8)-GNRs represent the same energy gap, corresponding to the difference between the state with periodicity $p = 2a$ and the next LUMO state. The differences between these gaps can then be attributable to their different width. We find that these differences are significant in shorter ribbons, showing smaller gap for (3,1,4)-GNRs than for (3,1,8)-GNRs, but became negligible in longer ribbons with N $>$ 8 (within our uncertainty of 0.01 eV). The asymptotic fits towards zero gap are in agreement with the electronic structure expected for infinitely long (3,1,c)-GNRs shown in Figure 4.2, for which all the Bloch states are allowed and, consequently, the gap between consecutive eigenstates in the conduction band tends to zero as the length of the GNR increases. As regard the HOMO-LUMO gap for width $c = 8$ discussed above, from our data it is hard to discern between a small band gap ($\Delta_{HL} << 0.1$ eV) and a gapless conduction band ($\Delta_{HL} = 0$) for ribbons long enough as to represent the 1D solid infinite crystal (N $>$ 30).

On the other hand, the Δ_{HL} gap of (3,1,c)-GNRs has been predicted to

be zero by Yazyev *et al.* for $c = 12$ in ref. [18], while for $c = 8$ Li *et al.* in ref. [27] propose a small topologically protected gap of 0.02 eV. The key point here is that the metallic character of the zig-zag edges is preserved down to very narrow ribbons, and therefore, this could explain the tendency of our experimental values of Δ_{HL} gap of (3,1,8)-GNRs to very small values below 0.03 eV.

The modulation of the tunneling conductance observed along the chiral edges of longer ribbons (N > 6), provides a map of the wave function distribution, Ψ, for the corresponding discretized states allowed in the finite ribbon. Apparently due to the geometry of the chiral and armchair edges in (3,1,c)-GNRs, the 1D edge states cannot behave as electron-like quasiparticles confined inside the ribbon (PIB model). Instead, (3,1,c)-GNRs wave functions follow a different discretization law that requires an optimized model Hamiltonian to explain our experimental observations of the states in finite and charged (3,1,c)-GNRs on Ag001.

Chapter 5

Graphene nanoribbons on MgO

Electronic devices require the presence of a decoupling layer between the active element and any supporting metal. In microelectronic devices, this role is nowadays played by thick oxide layers like SiO_x, Al_2O_3, SnO... This oxide is the substrate, the isolating layer of electronic elements and, below it, the active gate electrode can be found. In this chapter, we evaluate the suitability of an atomic layer of MgO to play the role of gating oxide in atomic scale devices built with functional organic molecules. Firstly, we describe the optimized method to grow ordered ultra-thin films of MgO on the Ag(001) substrate. Then, we discuss the transfer of (3,1,8)-GNRs from Ag(001) substrate to the oxide islands by atomic manipulation. Comparing the electronic characterization of (3,1,8)-GNRs with lengths between N = 3 and N = 12 on Ag(001) (Chapter 4) and on MgO_{ML}/Ag(001), we will provide a comprehensive report on the effects of MgO_{ML} in the electronic structure of organic molecules that are placed on top.

5.1 Preparation and characterization of MgO monolayer islands

For the sample preparation of MgO_{ML} islands on Ag(001), we start with the calibration of the commercial Knudsen cell manufactured by CreaTec. After degassing the pure pellets of Mg loaded on the cell at 150 °C, we proceed to find the sublimation temperature of Mg under UHV conditions. We tried a first deposition of Mg after monitoring a minimal rise of the basal pressure in the preparation chamber when the temperature of the Knudsen cell exceeds

310°C (sample 1 in Table 5.1). The presence of Mg islands cover approximately 4% of the surface. In addition to the square islands we also distinguish bright dots on the surface that resemble the surface of an amorphous Mg-Ag alloy.

Previous works on MgO preparation affirm that MgO islands grow on Ag(001) during the sublimation of pure magnesium under an O_2 atmosphere [133–135]. From the available bibliography we can state beforehand that the morphology of the MgO structures obtained depends on the following parameters: the temperature of the substrate (T_{Ag}), the deposition rate controlled by the temperature of the Mg evaporator (T_{Mg}) and the implementation of different post-treatments.

Sample	**T_{Ag} (°C)**	**T_{Mg} (°C)**	**Time (min)**
1	r.t.	310	0.5
2	220	315	3
3	220	340	3
4	375	310	6
5	350	315	3

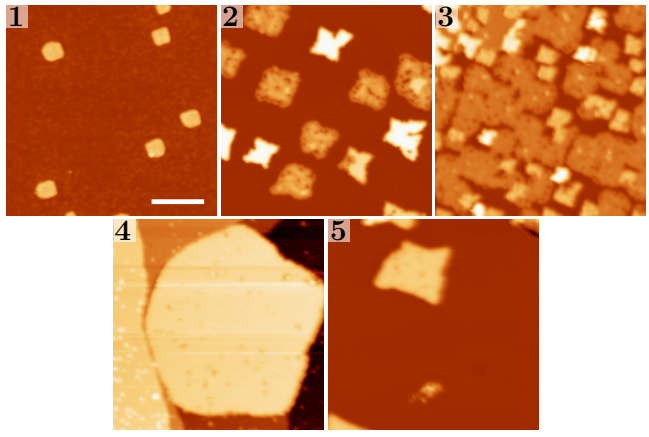

Table 5.1: Parameters employed to grow MgO/Ag(001) samples. The samples 2-5 are prepared with $p_{O_2} = 1 \cdot 10^{-6}$ mbar. STM images of representative surveys of samples 1-5. Scale bar: 20 nm. SP_1: 1 V, 100 pA, SP_{2-5}: 3 V, 20 pA.

At this point, we should explain the characteristic differences observed in MgO islands on Ag(001) that provide a measure of the target quality of the MgO islands of our samples. We will now focus in how to differentiate, in optimized samples, multilayer and bilayer (MgO_{BL}) from embedded monolayer MgO (MgO_{ML}) islands. In Figure 5.2a we identify three islands of MgO with similar topography appearance and Figure 5.2b shows their representative STS

spectra recorded inside the colored squares indicated in the STM image. The violet and red spectra show a common peak around 2.6 V, an energy in good agreement with reported values of the surface state of a monolayer of MgO [136, 137]. However, the green spectra do not show the feature at 2.6 V. Instead, its characteristic peak appears at higher energy (2.8 V), and can be related with a thicker MgO structures.

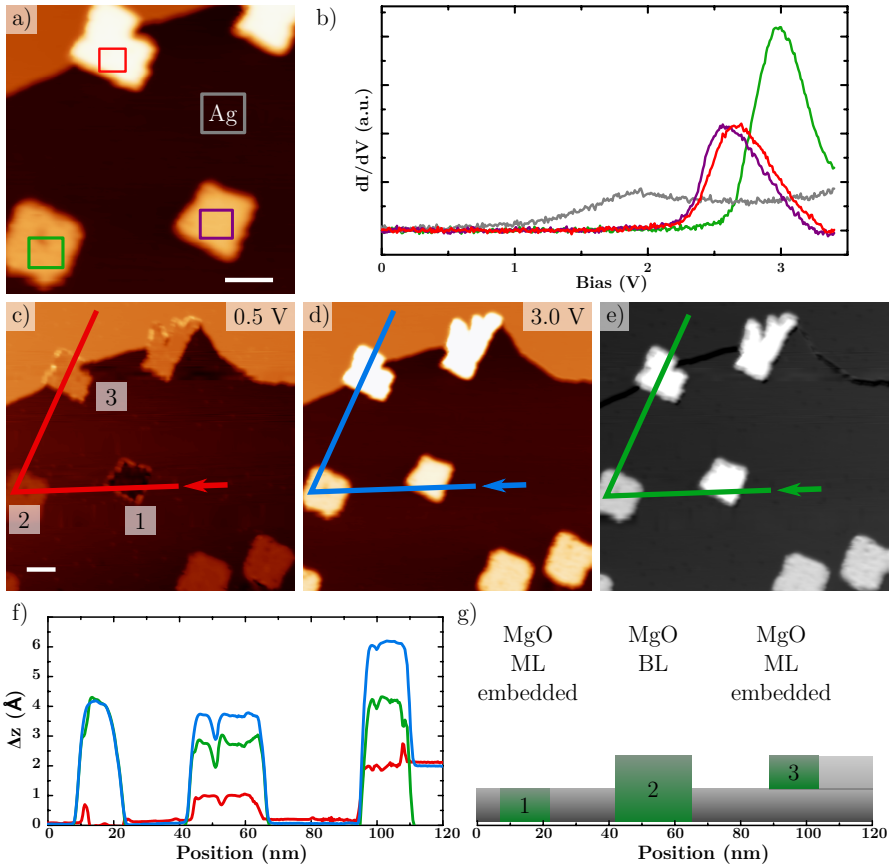

Figure 5.2: a) STM image of different kind of MgO islands on Ag(001) (3 V, 30 pA). b) STS spectra recorded on the islands shown in (a) (SP.) c-d)STM images of the same zone recorded at 0.5 and 3.0 V to show the apparent height differences. e) Difference between the 3 and 0.5 V images. f) Height profiles of islands 1, 2 and 3 taken at the lines included in b-e images. g) Schematic cross section of the surface. Scale bars in (a) and (c): 10 nm.

A combined STM and AFM study of MgO/Ag(001) solved the discrepancy in the apparent height of the MgO islands between both methods when STM images are recorded at 3 V [136]. The STM operating at voltages above the MgO surface state reveals larger apparent height than AFM images. This al-

lows us to differentiate the MgO_{ML} from other MgO structures by recording STM images at different voltages and analysing the topography height differences between them. The comparison between apparent heights at 3 V and 0.5 V turned out particularly useful. This is because the monolayer is the only thickness for which the peak associated to the surface state is fully integrated in the tunneling current. In Figure 5.2c-d we show the same MgO islands included in Figure 5.2a recorded at 0.5 an 3 V. While the STM image recorded at 0.5 V is more similar to the expected topography of embedded MgO_{ML} islands (the same height as silver surface), the STM image recorded at 3 V shows these islands with 0.4 nm in height. In Figure 5.2e we show the difference image between those STM images taken at scanning voltages where the MgO_{ML} islands display the same characteristic brightness. This method provides a quick and simple way to find MgO_{ML} islands in the surface. For the sake of clarity, Figure 5.2f shows the height profiles recorded in the images of panels c-d and Figure 5.2g the associated schematic representation of the surface, as concluded from the difference image (Figure 5.2e).

In Table 5.1 we summarize the optimization of MgO_{ML} islands. We include representative STM images of the samples obtained. T_{Mg} determines the Mg flux that reaches the surface. While in sample 2 we distinguish both individual monolayer and bilayer MgO islands, in sample 3 we only observe irregular structures originated from the combination of different heights on the same island. This means that if the flux is too high (high T_{Mg}) the new MgO structure prefers to grow on the already deposited MgO. In our system, an optimal flux of Mg is obtained with Mg cell temperatures closer to 315 °C, which is slightly above of the base sublimation temperature in UHV (determined in sample 1). On the other hand, to preferentially obtain MgO_{ML} islands, the temperature of the substrate needs to be high enough so the Ag atoms have enough mobility to allow the diffusion of new Mg and O atoms, allowing the lateral growth of the embedded island. Comparing the samples 2, 4 and 5 we can monitor the effect of substrate temperature in the morphology of the islands. Sample 2, prepared with the lowest T_{Ag}, contains small monolayer and bilayer islands. On the other hand, sample 4, prepared with the highest T_{Ag}, exhibits bigger islands where monolayer structures appear attached at the edge of the silver terraces. Between 220 and 400 °C we find the optimal temperature of the substrate around 350 °C, that allows us to generate MgO_{ML} islands embedded on the silver surface with sufficiently large area. The optimum T_{Mg} and T_{Ag} parameters are those of sample 5 in Table 5.1.

We observed that the apparent roughness of the islands improved after a post-annealing of the sample at the deposition temperature under UHV con-

ditions. It is important to perform this post-treatment under UHV conditions because the presence of oxygen during the post-annealing produces rougher MgO_{ML} islands. The Figure 5.3 shows the difference in apparent roughness between a sample obtained after post-annealing processes in an O_2 atmosphere (a) and under UHV conditions (b).

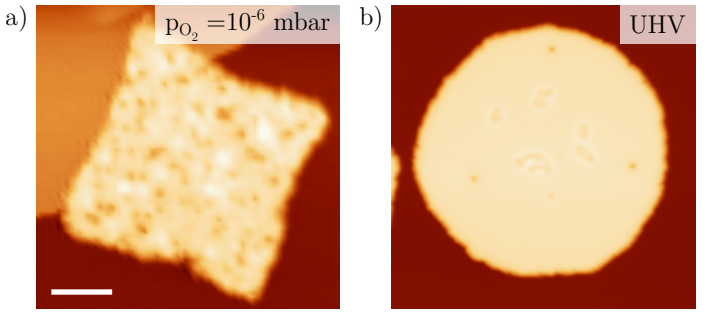

Figure 5.3: Effect of post-annealing in O_2 atmosphere and under UHV conditions (3V, 50 pA). Scale bar 10 nm.

With the aim of evaluating the shift in the local work function of the Ag(001) due to the presence of an ultra-thin MgO film, we recorded STS spectra in constant current mode in the field emission regime. This was done on MgO_{ML} islands and on bare Ag(001) surface. In Figure 5.4 we show representative field emission resonances (FER) obtained on Ag(001) and on MgO_{ML} embedded, together with a stack plot of spectra recorded across the interface between them. The yellow dotted line in Figure 5.4c marks the position of the physical border between the silver and the oxide. At this position, a gradual shift of the bare Ag(001) spectra develops, tending towards lower energy peak values and smaller inter-peak energy gaps. This is the typical behavior ascribed to the lowering of the work function. To quantify this effect in Figure 5.4d we provide a detailed analysis of the value of the local work functions ϕ_{Ag} and ϕ_{MgO} by means of eq. 2.10 (see section 2.3) [59, 61]. The relative decrease of the work function amounts to $\Delta\phi_{exp} = 0.84 \pm 0.07$ going from 4.03 eV on Ag(001) to 3.33 eV on MgO_{ML}/Ag(001). These values are in very good agreement with the reported theoretical work function of MgO_{ML}/Ag(001) [138, 139].

The dramatic lowering of the work function due to the presence of ultra-thin MgO films on Ag(001) has been attributed to electrostatic compression of the spilled out charge of the metal by the insulating layer [56]. It has been shown for pentacene molecules deposited on MgO_{BL}/Ag(001), that the decrease of the work function induce integer charge transfer [56]. In the following sections we

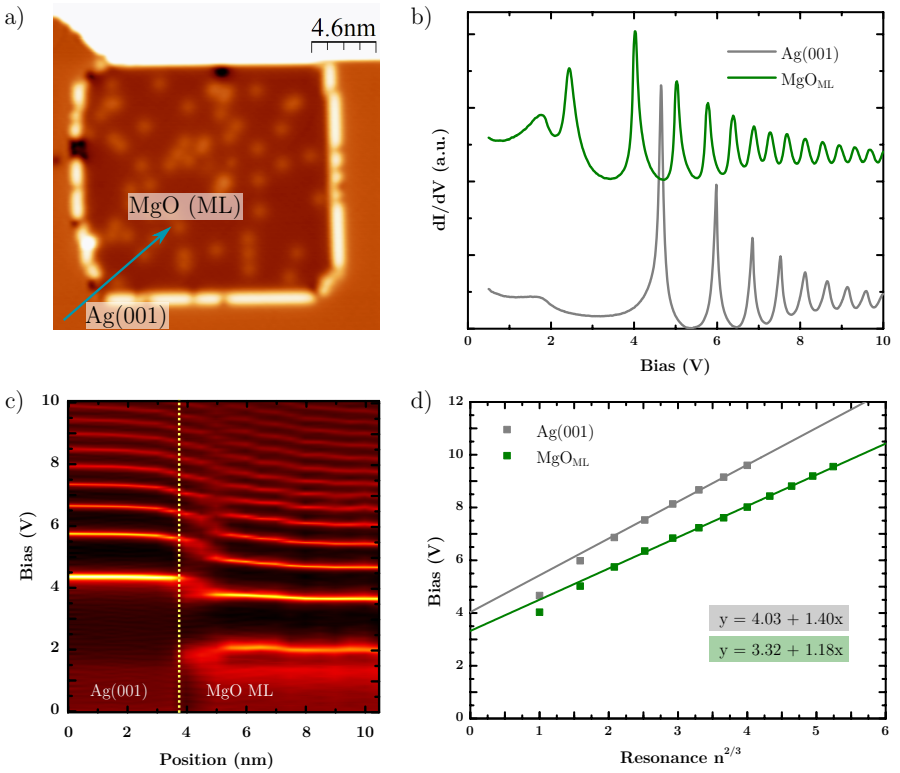

Figure 5.4: a) STM image of a MgO_{ML} island embedded in Ag(001). b) FER measurements recorded on Ag(001) and MgO_{ML} island. c) Stack plot of dI/dV spectra recorded along the blue arrow in a). The dotted yellow line corresponds to the Ag-MgO intersection in STM images. d) Peak voltages of FER shown in b) plotted against $n^{2/3}$. The intersect of the linear fits with the y axis gives the ϕ values (see equation 2.10).

will study how to place (3,1,8)-GNRs on embedded MgO_{ML} islands. We will also give a full description of the concomitant energy level rearrangement due to the charge transfer from the MgO_{ML}/Ag(001) system, as well as profound impact of the electronic decoupling from the silver substrate provided by the MgO spacer.

5.2 Positioning of ch-GNRs on MgO islands

The most common decoupling strategy for small organic molecules is to directly sublimate them on top of ultra-thin insulator films (1-3 atomic layers). This is the method used in the seminal work of characterization of pentacene molecules on ultrathin films of NaCl on Cu(100) [69] or in the previously mentioned study of pentacene on MgO_{BL}/Ag(001) [56]. However, this approach is not plausible for bigger organic structures. To have the (3,1,8)-GNRs placed on top of MgO_{ML} islands, we have attempted two alternative strategies: the intercalation of MgO under the GNRs; and their lateral transfer from the metal surface onto embedded MgO_{ML} by atomic manipulation.

5.2.1 Study of MgO intercalation in (3,1,8)-GNR/Ag(001)

Decoupling graphene structures from metal substrates is a well-known topic and aims at modifying its interaction with the substrate to enable applications in electronics. The oxygen and metal intercalation to decouple graphene have been extensively studied on different substrates such as Ru(0001) [140], Ir(111) [141] or Ni(111) [142]. The high mobility of silver atoms in Ag(001) crystals and the similar conditions to prepare both the (3,1,8)-GNRs and good quality MgO_{ML}, led us towards this methodology.

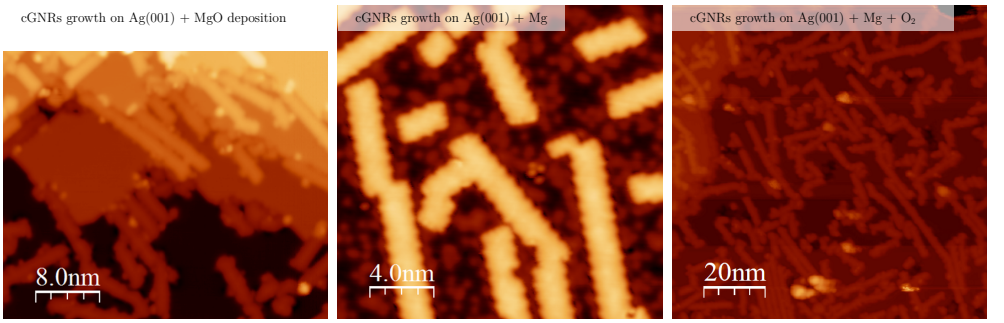

Figure 5.5: Study of MgO intercalation in (3,1,8)-GNR/Ag(001). a) STM image of a GNR/Ag(001) sample exposed to MgO deposition (0.5 V, 30 pA). b) STM image of a GNR/Ag(001) sample after Mg deposition (0.1 V, 0.5 nA). c) STM image of a GNR/Ag(001) sample after Mg deposition and then exposed to an oxygen atmosphere (0.5 V, 80 pA).

After the growth of (3,1,8)-GNRs on clean Ag(001), as described in section 4.2.2, we directly deposit the MgO on this sample held at 210°C, a temperature low enough to preserve the GNRs integrity. In Figure 5.5a we show a

representative STM image of the obtained sample. The irregular shape of the GNRs indicate the presence of atoms (Mg and/or O) decorating their chiral edges. To better understand the appearance of these defects, we then studied the exposure to Mg. The Figure 5.5b shows a STM image of the samples obtained after the deposition of Mg onto the GNR/Ag(001) sample held at 210°C. We distinguish around the GNRs a surface that resembles the alloy obtained after Mg deposition onto clean Ag(001) (sample 1 in Table 5.1), but the GNRs are defect free. After the exposition of this sample heated at 300°C to an oxygen atmosphere ($p_{O_2} = 1\times10^{-6}$ mbar) we obtain again the decorated chiral edges. The defective GNRs are distinguishable in Figure 5.5c. As occurs with (3,1,4)-GNRs [143], the high reactivity of the zig-zag parts along the chiral edges in (3,1,8)-GNRs are susceptible to react under oxidizing conditions and the intercalation is therefore incompatible with our objectives.

5.2.2 Atomic manipulation of ch-GNR into MgO

Our second strategy consists in preparing optimized MgO/Ag(001) samples to obtain embedded MgO_{ML} islands, to grow subsequently the (3,1,8)-GNRs over the remaining Ag surface as described in section 4.2.2. Then, the GNRs can be moved across different positions of the surface by lateral manipulation. As mentioned in section 2.2, the lateral manipulation of molecules can be performed in constant height or constant current mode. In the case of (3,1,8)-GNRs along the silver surface, the manipulation can be performed in both modes, being safer the constant current mode where the feedback allows the tip to adapt to the inherent fluctuations of the manipulation procedure. However, the insertion of GNRs into MgO islands requires to carry out the manipulation in constant height mode to avoid the sharp approach of the tip to the surface as a response to the electronic differences between both regions.

In Figure 5.6 we show schematically how is the GNR manipulation under both feedback conditions, together with corresponding experimental manipulation traces of GNRs. In constant current mode (feedback ON) the tip is approached with low bias and high current (SP: 3 mV, 10-20 nA) to the armchair edge of the ribbons, which appears to be the preferred zone to stick the metallic tip apex. At this short distance, the interaction between the ribbon and the final atoms of the tip provides enough lateral force as to produce the displacement of the GNR following the movement of the tip to the new position. Once the ribbon is close to the border of the island, the last manipulations to enter into the MgO_{ML} island are performed in constant height mode. With a similar set point (SP: 3 mV, 10 nA) the tip is located close to the armchair

edge of the ribbon and then moved into the MgO_{ML} island keeping the height constant during the entire path. When the GNRs follows the movement of the tip into the island, its manipulation trace shows how the ribbon hops over the insulating surface in the tunneling current channel.

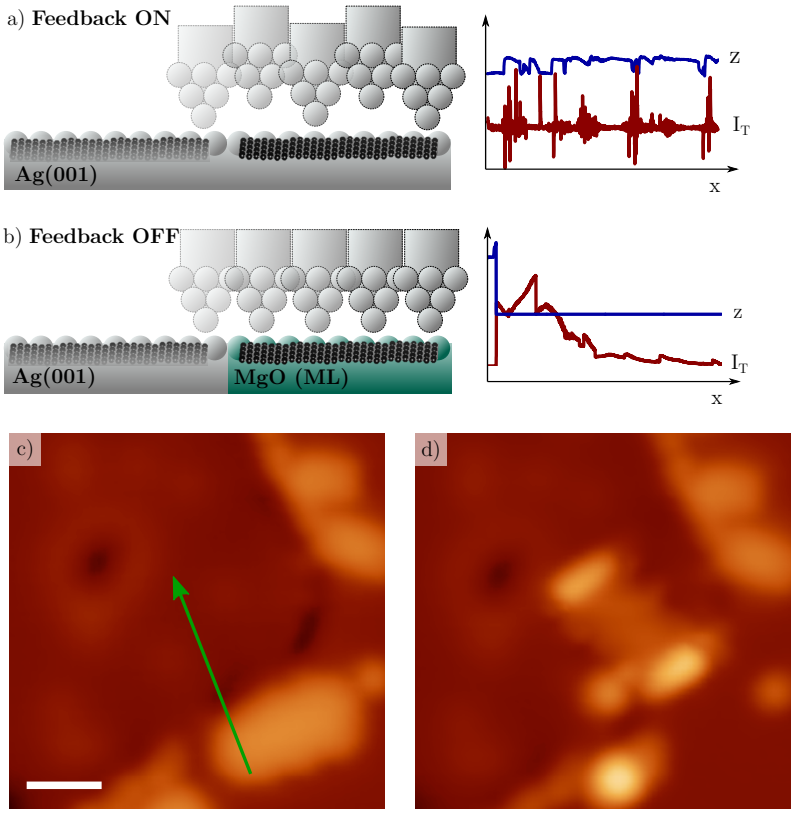

Figure 5.6: Schematic illustration of the atomic manipulation of a GNR together with manipulation traces recorded in constant current mode (a) and in constant height mode (b). First manipulation of a GNR to transfer it to MgO. STM image before (c) and after (d) atomic manipulation of a N = 3 (3,1,8)-GNR.

In Figures 5.6c and 5.6d we show the STM images recorded before and after introducing the first (3,1,8)-GNR into an embedded MgO_{ML} island. The manipulation trace shown in Figure 5.6b corresponds to this first successful repositioning of a ch-GNR on MgO_{ML}.

5.3 The effect of a MgO monolayer

5.3.1 Increased life time of tunneling electrons

When the (3,1,8)-GNRs are introduced in the embedded MgO_{ML} islands, two remarkable modifications of the single point spectroscopy curves take place: the reduction of the full width at half maximum (FWHM) of the peaks and the emergence of additional resonances. In Figure 5.7a we show the STS spectra recorded on (3,1,8)-GNRs of different lengths (N = 3, 5, 6, 8 and 12) placed on top of MgO_{ML} islands where both phenomena are evident.

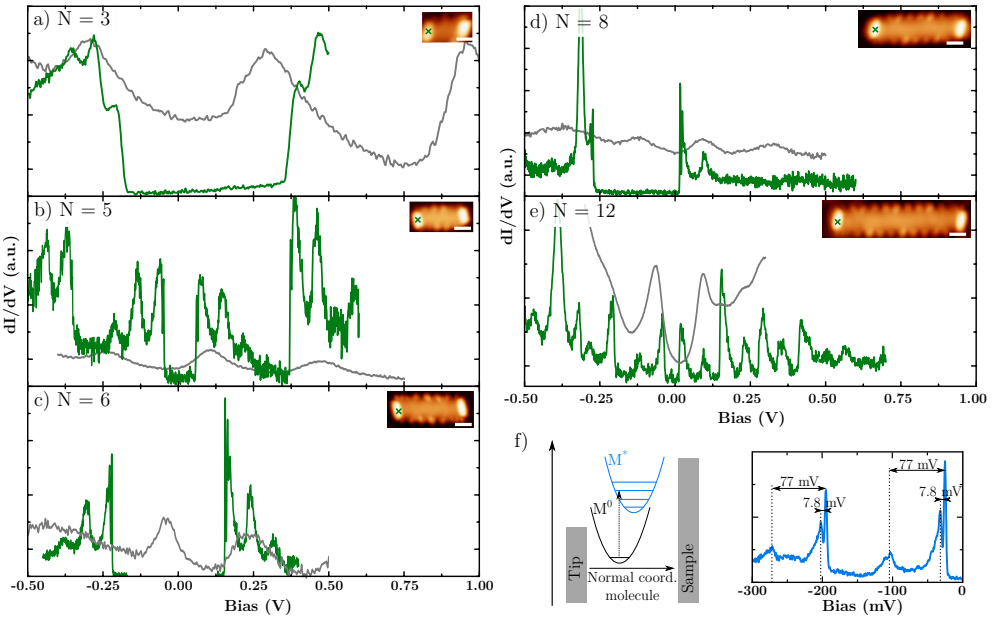

Figure 5.7: Electronic characterization of (3,1,8)-GNRs. a-e) STS point spectra recorded on (3,1,8)-GNRs of lengths between N= 3 and N = 12 on Ag(001) (grey spectra) and on MgO_{ML} (green spectra). The STM topography images show the (3,1,8)-GNRs/MgO_{ML} where STS was recorded. Set point: 0.5 V, 100 pA. White scale bars: 1.6 nm.V_{mod} = 4 to 1 mV. f) Sketch of Franck-Condon mechanism in an STM junction (adapted from ref. [144]) and example of STS spectra with satellite resonances recorded on N = 12 (3,1,8)-GNR.

The Heisenberg principle relates the sharpness of a spectroscopic peak to the lifetime of the corresponding state in an inversely proportional manner, which indicates that the lifetime of the states is increased with the presence of a monolayer of MgO. To determine the intrinsic FWHM of the states we recorded high resolution STS spectra on a N = 5 GNR at different modulation voltages

between 0.065 and 1 meV at a stable temperature of 1.1 K. As mentioned in section 2.4.1, at this temperature the energy resolution of the JT-STM in dI/dV mode is 0.10 meV. Figure 5.8 shows five STS spectra and the obtained FWHM values as a function of the modulation voltage. From this analysis we conclude that the intrinsic FWHM of the the states is 1.6 meV, obtained from the STS spectra recorded operating at V_{mod} = 0.065 mV. This FWHM value is five times lower than the width of features observed by us on Ag(001) in Chapter 4, and is much lower than the 113 meV of FWHM reported for (3,1,4)-GNR/$NaCl_{BL}$ [126]. As shown in Figure 5.8c, the energy values are not affected by the reduction of the modulation bias, and hence we can operate with 1 meV as modulation voltage for the electronic characterization of (3,1,8)-GNRs, which allows us to reduce the measuring times up to 5 times with respect to modulations below 0.2 mV.

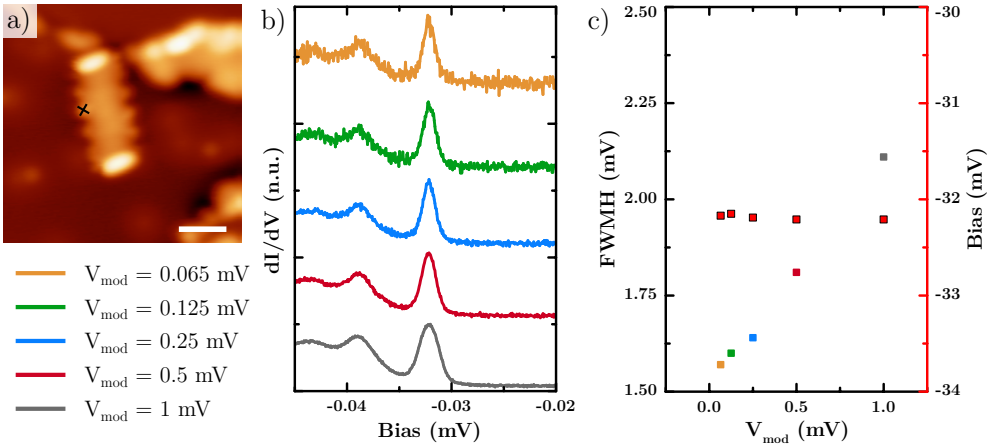

Figure 5.8: a) STM topography image of a N = 5 (3,1,8)-GNRs on MgO_{ML} (0.5 V, 200 pA, T = 1.1 K, scale bar = 2 nm). b) STS point spectra recorded on the position of the cross included in (a), with different V_{mod} between 1 and 0.065 mV. c) Experimental FWHM and bias voltage values of the peaks versus V_{mod}.

The sharpening of the peaks in the STS spectra recorded on GNRs/MgO_{ML}, and the concomitant increase in the tunneling electron lifetime in the ribbon, allow us to observe new phenomena that appear blurred in the broad peaks of GNRs on Ag(001). First, satellite resonances spaced from the intrinsic states (characterized by sharp peaks) by 7.8 and 77 meV are visible in STS spectra in both bias polarities. We identify them as Franck-Condon (FC) resonances. This kind of resonant side peaks are vibronic excitations of the positive or negative ion molecule that conserve atomic coordinates and momentum of the neutral specimen. In other words, the electron/hole tunnels to a molecular

orbital and remains there time enough as to populate higher energy states of the ionized molecule that are simultaneously vibrationally excited. An sketch of the FC mechanism is represented in Figure 5.7f. This resonant transitions have been reported in electrically isolated molecules by tunneling spectroscopy [144], but also in weakly coupled graphene nanoribbons [145]. Since the excitation is triggered by electrons tunneling into a molecular orbital, the way to distinguish FC resonances from other molecular orbitals is to look at their spatial distribution.

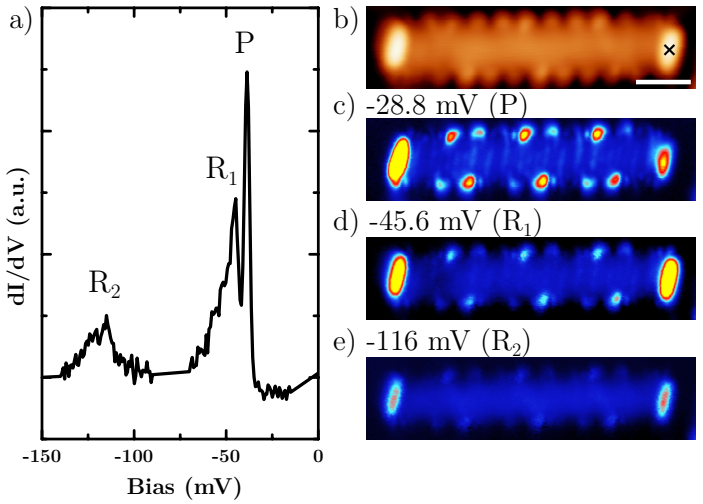

Figure 5.9: Franck-Condon resonances observed on GNRs/MgO_{ML}. a) STS spectra recorded on a N = 12 (3,1,8)-GNR including peak labels for the main peak (P) and satellite peaks (R_1 and R_2). STS SP: 0.5 V, 200 pA, V_{mod} = 1 mV. b) STM topography image of the N = 12 (3,1,8)-GNR including a cross where STS spectrum shown in (a) is recorded (0.5 V, 200 pA). c-e) Constant height dI/dV maps recorded at the corresponding energies of the main and satellite peaks observed in (a). SP: 0.5 V, 200 pA, V_{mod} = 4 mV.

Figure 5.9 shows the STS spectra recorded on a N = 12 (3,1,8)-GNR together with corresponding dI/dV maps at the main and satellite peak energies. The spatial distributions of the dI/dV maps recorded at P, R_1 and R_2 energies show the same features but with higher contrast and corrugation in the LDOS map recorded at the P energy, which agrees with the hypothesis that P is the main peak and R_1 and R_2 correspond to vibrational FC resonances. The spacing between the resonances corresponds to the energy of the elementary excitation of a given vibrational mode. Therefore, the two satellite resonance found for each molecular orbital must correspond to either two different charged states or two different vibrational modes. The spacing of the

FC resonances were also studied for N = 5 (3,1,8)-GNR obtaining the same values, which indicates that the detected vibrational modes are characteristic of the 1D ribbon lattice.

A second striking observation on GNRs/MgO_{ML} is a rigid shift in the energy of the states along the ribbon's axis. Note that without the energy sharpening of molecular states caused by the MgO electronic decoupling, this kind of shifts would not be resolved. We attribute this shift to a gating of the GNR states due to the underlying electric polarization profile, which is in turn caused by punctual defects on the MgO_{ML} island. The detailed study of the effect is included in section 6.3. The straightforward consequence of this varying electric polarization below the ribbon is that STS spectra recorded at different points along the chiral edge exhibit a variation in the energy value at which the state is found. This phenomenon is observed in all the GNRs, being more evident in the longer ones. Figure 5.10 shows the exemplifying case of N = 12 (3,1,8)-GNR. Here the shift of the energy value of the main peak goes from -22 mV in the center of the ribbon to -36 mV at the armchair edges. This variation of the energy is rigid for all the features (see Fig. 5.10c).

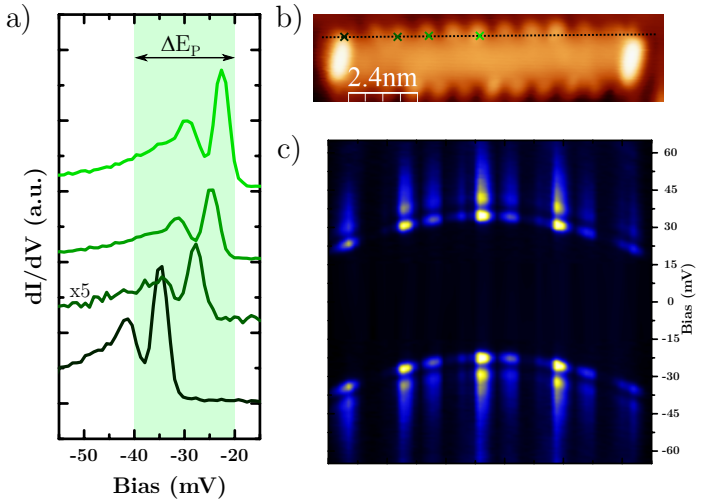

Figure 5.10: Shift in energy along the chiral edge. a) STS spectra recorded at different positions of the chiral edge on N = 12 (3,1,8)-GNR. b) STM topography image of the N = 12 (3,1,8)-GNR including crosses where STS spectra shown in (a) are recorded (0.5 V, 100 pA). c) Stack plot of dI/dV versus position recorded on the chiral edge of the N = 12 (3,1,8)-GNR shown in b (dotted line). STS SP: 0.5 V, 200 pA, V_{mod} = 1 mV.

These energy shifts give rise to undesired artefacts in dI/dV maps of the GNRs. To obtain representative spatial distributions of the local density of the

states (Ψ) it is necessary to measure and piece all together a set of dI/dV maps recorded in the energy window span of the shift along the GNR. In Figure 5.11 we show the example of the N = 12 (3,1,8)-GNR. The dI/dV maps recorded at different energies between -20 to -30 mV show the rearrangement of the intensity from the center to the armchair edges as the tunneling bias decreases. To obtain the approximate real spatial distributions of the corresponding orbital, these dI/dV maps are normalized to the intensity at the center of the ribbon and averaged. Figure 5.11b shows the resulting map. Note that, although the intensity is dominated by the main peak, at certain positions the intensity is also contributed by the FC resonance inside the energy range of interest.

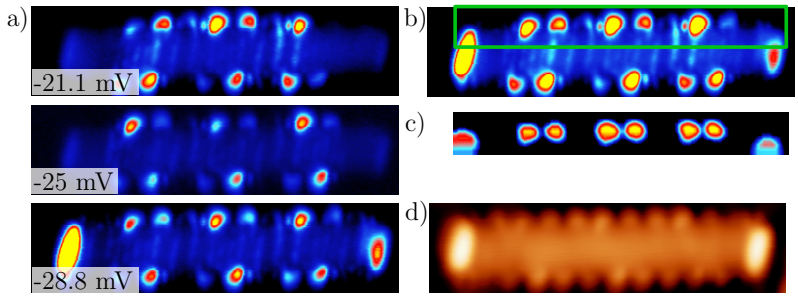

Figure 5.11: Reconstruction of the spatial distribution of LDOS peaks observed in Figure 5.10. a) dI/dV maps recorded at different energies between -20 to -30 mV. (SP: 0.5V, 100 pA, V_{mod} = 1 mV) b) Reconstructed dI/dV map obtained from merging the dI/dV maps shown in a (see reconstruction details in the main text). c) Feature distribution map for the main peak shown in Figure 5.10a obtained with the FD-STS algorithm. The spatial position corresponds to the green square included in b.

To evaluate how much affects the resonance contribution in the reconstruction of Ψ wave forms, we have also analyzed our data with the Feature Detection Scanning Tunneling Spectroscopy (FD-STS) algorithm recently developed by Martínez-Castro *et al.* at the Research Center Juelich GmbH [146]. The FD-STS method allows to find all the positions where a spectroscopic feature (in our case a peak) is present in a range of energy previously set. First, STS point spectra are recorded at every (x, y) position of a grid containing the GNR. Then, we select a peak by its shape and intensity and, lastly, a feature distribution map (FDM) is obtained with intensity values representing the number of times that the peak is found at certain (x, y) point. Figure 5.11d shows the example of a FDM of the main peak obtained in the energy window from -20 to -40 mV, represented as ΔE_P in Figure 5.10a. Comparing Figure 5.11b and 5.11c we can conclude that both reconstruction methods allow us to discern the spatial distribution of the main peak, aside of the contributions of the 7.8 mV FC resonance and the position dependent energy shifts.

5.3.2 Electron doping

The reduction of the work function observed from Ag(001) to MgO_{ML}/ Ag(001) (see section 5.1) suggests that (3,1,8)-GNRs laid on top of MgO_{ML} islands will be negatively charged and hence, a new level alignment of its molecular orbitals (referred as *H1*, *L1* and *L2* in Chapter 4) will be likely to occur.

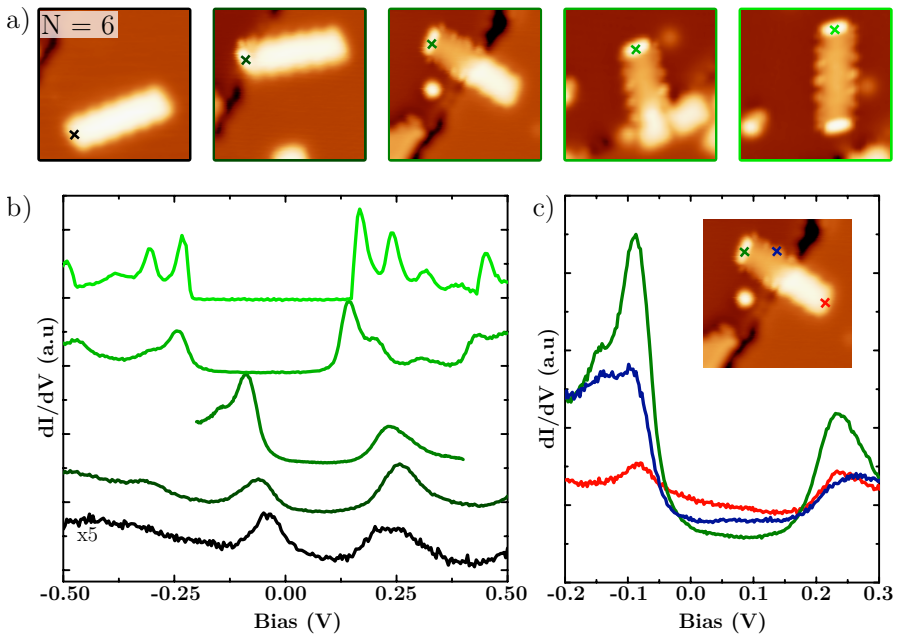

Figure 5.12: a) Series of STM images of the manipulation of N = 6 (3,1,8)-GNR from Ag(001) to a MgO_{ML} island. b) STS spectra recorded at the positions marked by the crosses in (a) during the GNR manipulation. c) STS spectra recorded at the positions marked by the crosses in the inset. STM images and STS SP: 0.5 V, 200 pA, V_{mod} = 8 mV. Images size 8×8 nm^2.

To identify the shift of the previously found states on Ag(001) (Figure 4.17 and Table 4.3 in section 4.3.2) we have characterized several GNRs at different positions during the insertion process into the MgO_{ML} islands. Figure 5.12 shows a series of STM images and STS spectra recorded on a N = 6 (3,1,8)-GNR during its manipulation from Ag(001) surface into an embedded MgO_{ML} island. The peaks of the STS spectra recorded on Ag(001) display a FWHM of 0.07 and 0.12 eV that gradually decrease as the GNR is introduced in the MgO_{ML} island. The STM images reveal an abrupt change in the topography appearance between precursor units that are inside and outside the MgO_{ML} island, which is also visible at intermediate stages. Those precursor units inside the island show a characteristic brightness at the armchair edges rather

similar to the one observed in the conductance maps recorded on Ag(001) (see Fig. 4.18 in section 4.3.2). In addition, the shift to lower energy values of the peaks due to the new electron transfer flow from the substrate to the GNR, is evident comparing the spectra of Figure 5.12b, which corroborates that GNRs are negatively charged. Hence, we can conclude unambiguously that the MgO decoupling monolayer has the counterintuitive effect of promoting charge transfer towards the adsorbed GNRs, in agreement with previous studies of pentacene molecules [56].

Comparing the STS spectra included in Figure 5.12b, we can conclude that the shift in energy is produced when a significant number of precursor are inside of the MgO_{ML} island. This allowed us to track down the orbital assignment (*H*, *L1* or *L2*) of some GNRs spectroscopic features for which detailed LDOS imaging on Ag(001) could not be retrieved in the course of this thesis. Figure 5.12c shows the STS spectra recorded at different positions along the N = 6 (3,1,8)-GNR when half of the ribbon is introduced to the MgO island. We observe that the energy of the peaks remains intact, whilst their intensity is smaller on STS spectra recorded on the section of the ribbon that remains on the Ag(001). This observation corroborates that the doping of the ribbon is not local, and the charge gets distributed along the whole ribbon, as is expected for delocalized edge states.

5.3.3 Electronic structure of ch-GNR on MgO

In section 5.3.1 we have explained different analysis techniques developed to unveil the spatial distribution of ribbon's orbitals that are practically discrete states, and very sensitive to the electrostatic energy landscape. This is important in order to assign the already known states on GNR/Ag(001) (section 4.3.2) to the main peaks of the STS spectra recorded on GNR/MgO_{ML}. For instance, te double lobe structure with periodicity of $p = 3a$ shown in Figure 5.11 corresponds to the wave function Ψ_{L2} of *L2* state (see Fig. 4.18 in section 4.3.2), which appears now in the occupied energy region as a consequence of the electron doping.

The assignment of known states becomes more straightforward when we perform $\mathrm{d}I/\mathrm{d}V$ maps in intermediate stage of the manipulation, with the ribbon only partially laid over the MgO_{ML}. In the case of the N = 6 (3,1,8)-GNR we obtain common spatial distributions of LDOS at energies that follow the shift of the peaks displayed by Figure 5.12. Figure 5.13a shows an example of the spatial distribution Ψ_{L1} and Ψ_{L2} of the *L1* and *L2* states (see Table

4.3 in section 4.3.2) recorded at the time when GNR is on Ag(001), half and completely inserted in the MgO_{ML} island. In the case of other GNRs whose manipulation is performed without characterization of the intermediate positions, the assignment of known states to the STS peaks should be done comparing the spatial distribution of LDOS on both substrates.

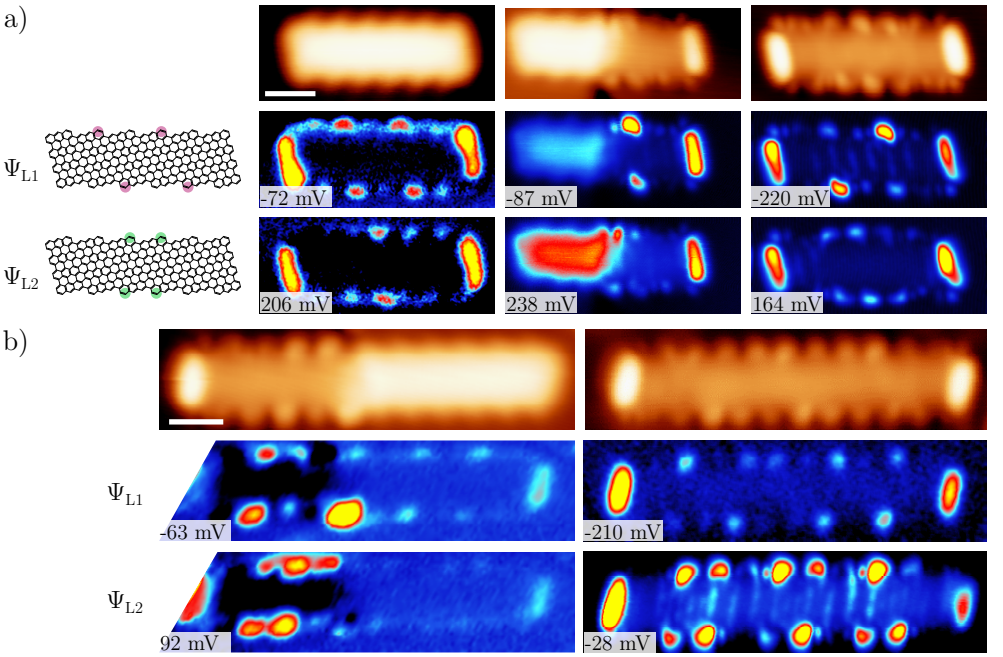

Figure 5.13: Spatial distributions of the Ψ_{L1} and Ψ_{L2} states of N = 6 (a) and N = 12 (b) (3,1,8)-GNR recorded at the time when GNRs are on Ag(001), half and completely inserted in the MgO_{ML} islands. Scale bar: 1.5 nm.

In Figure 5.13b we show the case of the N = 12 (3,1,8)-GNR, whose characterization on Ag(001) is missing. We observe an excellent agreement between spatial distribution Ψ_{L1} and Ψ_{L2} (see Figure 4.19 in Chapter 4) and the intensity in the recorded dI/dV maps when the GNR is at the intermediate position and completely inserted in the MgO_{ML} island. This allows us to directly assign the *L1* and *L2* states to the STS peaks of this ribbon on MgO.

5.4 Conclusions

In this chapter we have reported the relocation of chiral GNRs on top of MgO_{ML} islands. First, we present the optimized MgO growth on Ag(001). The sample preparation was optimized to obtain MgO_{ML} islands embedded in the upper atomic layer of Ag(001). Then, we report the manipulation protocol that allowed us to move ch-GNRs of different lengths from the metallic substrate to oxide islands. Finally, we study the electronic characterization of ch-GNRs during and after the manipulation to the MgO_{ML} island.

The presence of an atomic layer of MgO between the GNR and the metal produces an extraordinary increment of the life-time of the GNR's states. Comparing with the states that we studied in Chapter 4 on Ag(001), we observe in the STS spectra a reduction of the FWMH of the peaks and a shift in energy as the GNR is being introduced in MgO. The sharpening of the peaks allows us to observe transitions between vibrational states of the molecule (Franck-Condon resonances) and a rigid shift in energy of molecular states along the axis of the GNR. Both phenomena, interfere and make difficult the characterization of spatial distribution of states (Ψ). To overcome this problem we implement two techniques to reconstruct the true of $\mathrm{d}I/\mathrm{d}V$ maps in the energy range of each state. The combination of maps taking at various energies around the peak of interest, are compared with the output of the Feature Detection STS algorithm, to conclude both methods give us the spatial distribution of the main peak, leaving aside the satellites contribution and the tip position dependent shifts.

Thanks this thorough understanding of MgO_{ML} effects, in Chapter 6 we will focus on the spin splitting of GNR's states and gating effects, which are the breathtaking results observed on the ch-GNRs/MgO_{ML}/Ag(001) system.

Chapter 6

Magnetism and electric polarizability of GNR on MgO

In this chapter we start by a discussion about how magnetism arises in nanographenes to apply these concepts later on to our results in (3,1,8)-GNR structures. The presence of the MgO_{ML} allows us to observe unprecedented experimental evidences of magnetism in nanoribbons with edges composed by a large fraction of zig-zag segments. We finally show how an external electric field can be used to adjust the energy level alignment of the edge states with respect to the Fermi level of the supporting metallic electrode below the MgO barrier.

6.1 Magnetism in nanographenes

The magnetism in finite graphene structures emerges from the interactions among spins in singly occupied molecular orbitals. We will now focus in the study of magnetism in open- or closed-shell structures (see section 1.3), leaving aside the magnetism whose origin is based on the presence of point defects in the graphene structure. The essential principle is that not all p_z electrons of a graphene finite structure can be paired to form π-bonds. This key ingredient can be introduced in our model Hamiltonian through the Hubbard term accounting for electron-electron correlations, weighed by the strength of the Coulomb repulsion U ($U \neq 0$ in eq. 1.6).

In a graphene based nanostructure there are two types of carbons that belong to the two sublattices of graphene (being A and B the number of atoms in each sublattice). Lieb's theorem predicts that the total magnetic moment

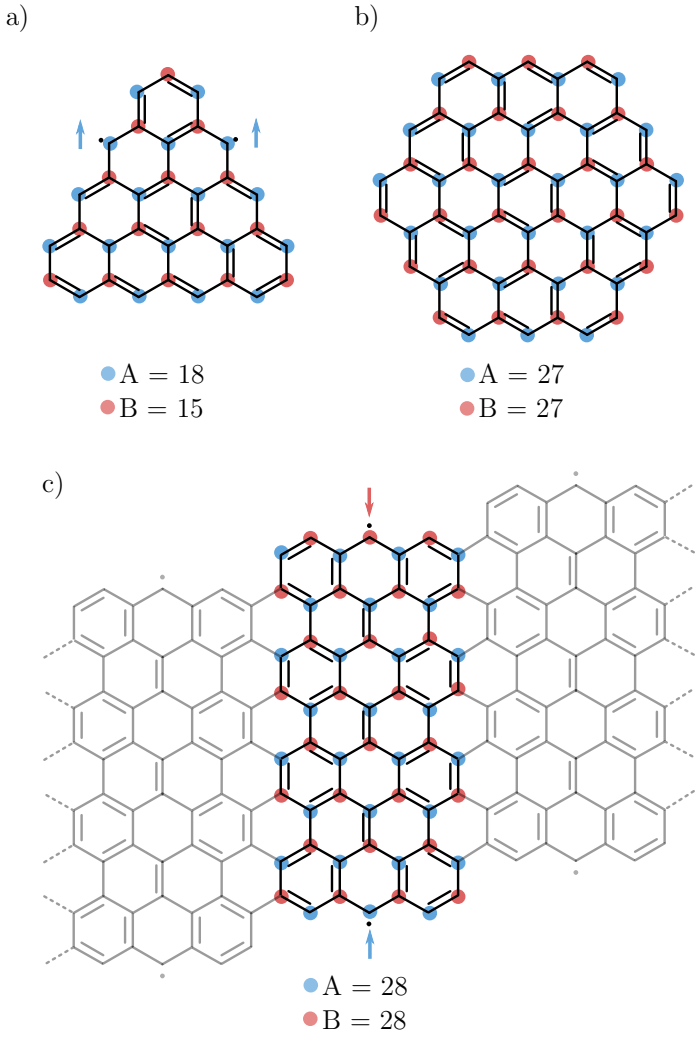

Figure 6.1: Scheme of graphene nanostructures with carbon atoms that belong to the same sublattice colored in red (A) and blue (B) respectively. a) Triangular graphene structure as example of unbalanced structure with S = 1 (a), hexagonal graphene structure example of balanced structure with S = 0 (b) and a (3,1,8)-GNR structure as example of open-shell structure with local magnetization at the radical sites (c).

of the ground state of nanographene structures is given by S = | $A - B$ | /2 [147]. In Figure 6.1a we show a triangular structure as an example of a symmetric structure with a sublattice imbalance ($A \neq B$). For this structure, Lieb's theorem predicts S = 1. This occurs for any triangular shaped graphene structure. Model calculations with $U \neq 0$, together with experiments, have confirmed the parallel spin alignment in the singly occupied orbitals of this kind of imbalanced lattices, fulfilling the prediction of Lieb's theorem to obtain the total magnetic moment S [148, 149]. In the case of balanced structures ($A = B$), Lieb's theorem predicts a total magnetic moment $S = 0$, which is compatible with diamagnetic states or antiferromagnetically arranged spin densities [150]. This is the case of the hexagonal structure shown in Figure 6.1b, even if it is a balanced bipartite lattice, the carbons in opposite sides belong to different sublattices, giving rise to a spontaneous sublattice magnetization [148].

A net local magnetic moment can be also induced by the spin polarization of low energy states that are highly spatially localized, even for the case of balanced sublattices. For open-shell graphene structures, a spontaneous magnetic order is induced due to the interaction among localized unpaired electrons in carbon radicals. This is the case for z-GNRs and ch-GNRs (as in Figure 6.1c), whose ground state is predicted to have a zero total magnetization ($S = 0$), but with the localized states along the edges hosting a magnetic moment with ferromagnetic alignment within the edge and antiferromagnetic coupling between opposite edges [18, 21, 26]. As mentioned in section 1.3 and section 4.1, when electron-electron correlations ($U \neq 0$) are taken into account in theoretical models, the ground state of z-GNRs and ch-GNRs is no longer the metallic state predicted for an infinite graphene sheet with a zig-zag contour, but instead the spin splitting of the state becomes energetically favourable [122]. The (3,1,8)-GNR structure is analyzed in Figure 6.1c as an example of theoretical antiferromagnetic nanographene due to the presence of localized electrons on its chiral edges. The first experimental evidence of spin splitting of localized electrons in this type of longitudinal structures is presented in section 6.2 of this Thesis.

6.2 Spin splitting of edge states

As described in section 5.3.3, we have assigned the spectroscopic features of ch-GNRs on MgO_{ML} to a certain Ψ state by combining three different inputs: (i) tracking the gradual shift of the spectral features as the ribbon is step-

wise introduced into the island; (ii) imaging the orbital spatial distribution in intermediate steps; or (iii) comparing $\mathrm{d}I/\mathrm{d}V$ maps of the different peaks with the known shape of the wave functions on Ag(001) reported in Chapter 4.

Figure 6.2 shows the resulting energy level diagram of Ψ states on Ag(001) and on /MgO_{ML}/Ag(001) for (3,1,8)-GNRs. For N = 12, whose characterization on Ag(001) is missing, the diagram shows the energies obtained from the characterization of the ribbon when it was half and completely inserted in the MgO_{ML} island. Dotted lines represent the shift in energy of Ψ states induced by the charge transfer in the cases in which we can unambiguously assign their orbital character following one of the three methods discussed above. For N = 6, 8 and 12 (3,1,8)-GNRs, we have performed their characterization at intermediate steps, and for N = 3 and 5, we have assigned the corresponding Ψ state on MgO_{ML} by comparing the shape of the wave functions obtained in $\mathrm{d}I/\mathrm{d}V$ maps recorded on both substrates.

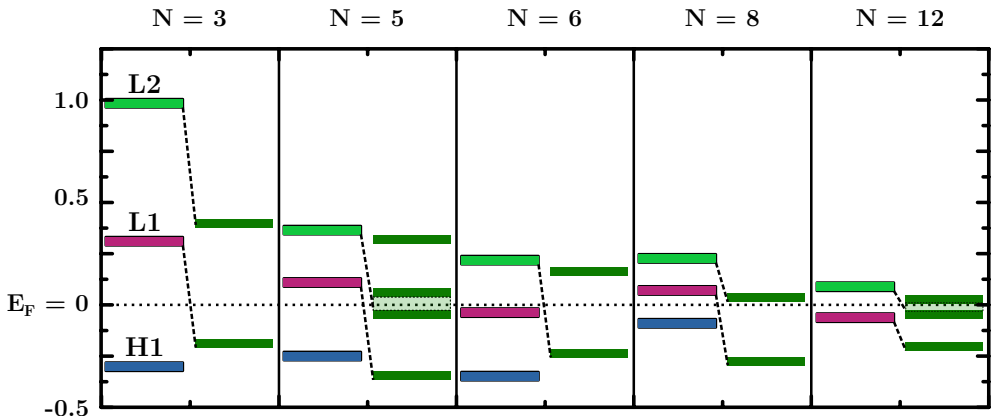

Figure 6.2: Experimentally determined energy levels of (3,1,8)-GNR states on Ag(001) (lines with same colors to the ones used in Figure 4.19) and on MgO_{ML} (dark green lines) and the energy level shifts (dotted lines) determined experimentally (see main text).

In the case of N = 5 and N = 12on MgO_{ML}/Ag(001), we observe peaks at both sides of the Fermi level. The gap between these peaks has a small value that does not correspond to any of the known gaps between molecular orbitals (see Table 4.3 in section 4.3.2). We cannot ascribe these gaps to a vibrational resonances because their value does not correspond with the FC resonance values obtained in section 5.3.1. Indeed, at first sight it seems to be only compatible with the splitting of the Ψ_{L2} state.

In section 6.1 we have explained that the interaction between localized

electrons in open-shell structures can give rise to magnetic ground states, which at T = 0 will tend to antiferromagnetic ordering in the case of balanced number of atoms in both sublattices. The key ingredient is the formation of singly occupied spin states as a consequence of the Coulomb repulsion that imposes an energy cost to the double occupancy of an otherwise degenerated state. Theoretical models include hypothetical values for the Coulomb interaction term (U) (see eq. 1.6) to interpret the interaction between localized electrons on neutral and free standing (3,1,8)-GNRs. However, to obtain accurate U values it is required an experimental set of data to fit the calculations. From experimental data alone we cannot directly obtain U values, but we can extract general conclusions about the electron-electron interaction in (3,1,8)-GNRs.

Attending to Figure 6.2, it is evident that the spin splitting is observed only when the shift in energy of a LUMO state (*L2* for N = 5 and N = 12 (3,1,8)-GNRs) locates this state in the occupied energy region and close to the Fermi level. To evaluate the electron doping required to produce an energy level rearrangement compatible with the spin splitting, we analyzed our data assuming the following two approximations. First, the Fermi level in neutral GNRs is found between *H1* and *L1* states, and second, an infinitely long GNR (N = ∞) will experience a similar electron doping induced shift (ΔD_{MgO}) as the one observed for N = 12 (3,1,8)-GNR. The later assumption is based on the fact that the electronic structure of (3,1,8)-GNRs evolves very slowly for N > 12, as shown in Figure 4.20. With this in mind, we can calculate ΔD_{MgO} from our experimental data obtained for N = 12 as

$$\Delta D_{\mathrm{MgO}} = E_{L1(\mathrm{MgO})} - \frac{\Delta E_{LH(\mathrm{Ag}(001))}}{2} = -200 - \frac{130}{2} = -265 \text{ meV} \qquad (6.1)$$

This estimation of ΔD_{MgO} allows us to guess the energy of the states of long GNRs when these are placed on $\mathrm{MgO_{ML}}$ just by measuring them on Ag(001) substrate. Figure 6.3 schematically illustrates the effect of a monoatomic layer of MgO and the cases when *L2* crosses the Fermi level and ends up (or not) spin split. Here, Δ_s is the energy increase of the global wave function caused by the double occupancy of each p_z state at the edge ($U \neq 0$). This way, we can predict if the spin splitting will take place by evaluating the necessary condition:

$$E_{L2(\mathrm{MgO})} + \Delta_s > 0 \qquad (6.2)$$

where $\mathrm{E}_{L2(\mathrm{MgO})}$ can be estimated as $\mathrm{E}_{L2(\mathrm{Ag}(001))} + \Delta D_{\mathrm{MgO}}$. When this come true, the system gains energy by emptying one of the two spin states of a given orbital, *L2* in this case. In our data, this condition only occurs for N = 5 and

N = 12 (3,1,8)-GNRs. The experimentally retrieved Δ_s values for them are 110 meV and 50 meV respectively (see Fig. 6.4b-c). In the case of N = 3, N = 6, N = 8 (3,1,8)-GNRs, their first state below the Fermi level remain fully occupied because, in terms of energy, this state is further down than Δ_s.

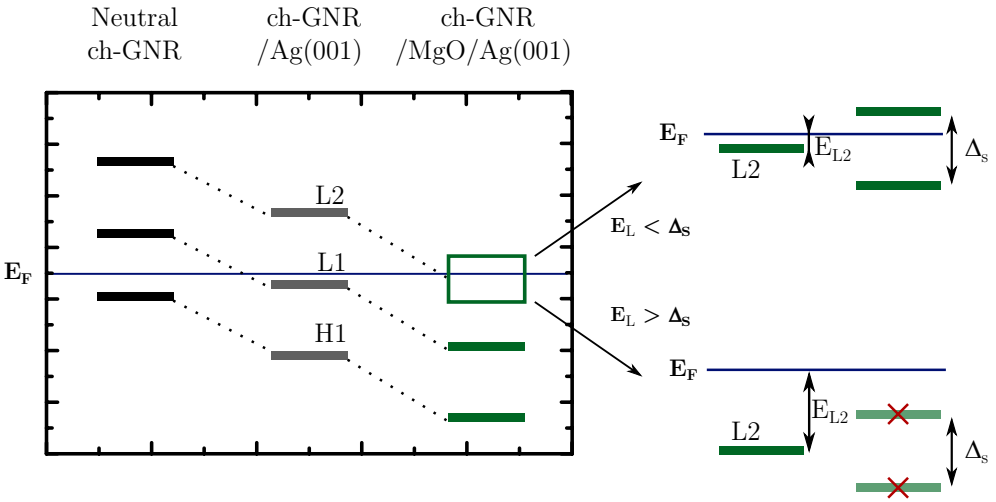

Figure 6.3: a) Scheme of the energy of the states of neutral and negatively charged (3,1,8)-GNRs by Ag(001) and MgO_{ML}/Ag(001) substrates. As discussed in the main-text, the *L2* spin splitting on MgO_{ML} depends on *L2* energy (E_L in the sketch).

In the case of the N = 8 (3,1,8)-GNR, it is expected that Δ_s takes an intermediate value between those of N = 5 and N = 12. Both of them are significantly smaller than E_{L1}, the first occupied orbital for N = 8 on MgO. Thereby, spin splitting should not occur. Note that if the electron doping were high enough as to shift the energy of *L2* state below the Fermi level (see STS spectra in Figure 6.4a), one would expect again a spin split doublet also for N = 8. Insets in Figure 6.4a display the dI/dV maps for N = 8 (3,1,8)-GNR at energies determined by the peaks found in STS spectra at both sides of the Fermi level. The spatial distribution of the LDOS is different from each other, which is in agreement with the absence of spin splitting. By comparing these dI/dV maps with the ones recorded for N = 8 (3,1,8)-GNR on Ag(001) (Figure 4.17b), we confirm that the spatial distributions correspond with the wave functions of *L1* and *L2* states respectively.

On the other hand, Figure 6.4b-c shows the dI/dV maps representative of the frontier orbitals of N = 5 and N = 12 (3,1,8)-GNRs. The wave functions of these states are identical with a periodicity of a double lobe structure $p = 3a$, which coincides with the wave function of Ψ_{L2} states on Ag(001) (see Fig.

4.19). The fact that the energy gap between these states is lower than the observed gaps between orbital states and, more importantly, the fact that the $\mathrm{d}I/\mathrm{d}V$ maps recorded at energy peaks found at both sides of the Fermi level show identical wave functions, are sound proofs of the spin splitting due to electron-electron interactions. The increased lifetime, together with the spatial localization of *L2* state, are responsible for the observed splitting in a singly occupied molecular orbital (SOMO, below E_F) and a singly unoccupied orbital (SUMO, above E_F) on $\mathrm{MgO_{ML}}$/Ag(001). This suggest that the spin resolved LDOS, which could be accessed by means of spin polarized STM (SP-STM), will exhibit the predicted magnetic ground state with parallel local spin alignment along the same edge and antiparallel between opposite edges.

It is important to remark here that our experimental Δ_s gap does not correspond with predicted magnetic gap between HOMO-LUMO states (or CV-BV bands at $k = 0$) of chiral graphene nanoribbons [27]. On the contrary, here we demonstrate that magnetism in graphene finite structures is not restricted to the weakly dispersing bands near the Fermi level of the neutral band structure and it may appear for any other spatially localized state.

6.3 Controllable gating of ch-GNR on MgO

In section 5.3.1 we have presented the energy shift of the molecular states in a N = 12 (3,1,8)-GNR (Figure 5.10) as a function of the lateral tip position. This shift is rigid for all the Ψ states regardless of their bias sign, which suggest that it arises from a an electric field driven gating effect. Actually, we have observed this effect varying the tip position in x, y or z direction. In the following sections we differentiate the origin of the energy shift due to the presence of point defects (gating when the tip moves in (x,y) plane) and to the controlled variation of tip-substrate distance (gating when the tip moves in z direction).

6.3.1 Local electric polarization around point defects

The quality of the MgO islands in the optimized samples is evaluated in terms of morphology of the islands to obtain embedded $\mathrm{MgO_{ML}}$ islands. However, these islands are not necessarily stoichiometric MgO. The $\mathrm{MgO_{ML}}$ islands present point defects related with the atomic vacancies or substitutional defects in the MgO lattice. These defects are easily visible in atomically resolved STM images. Figure 6.5 shows an example of this. The STM image recorded

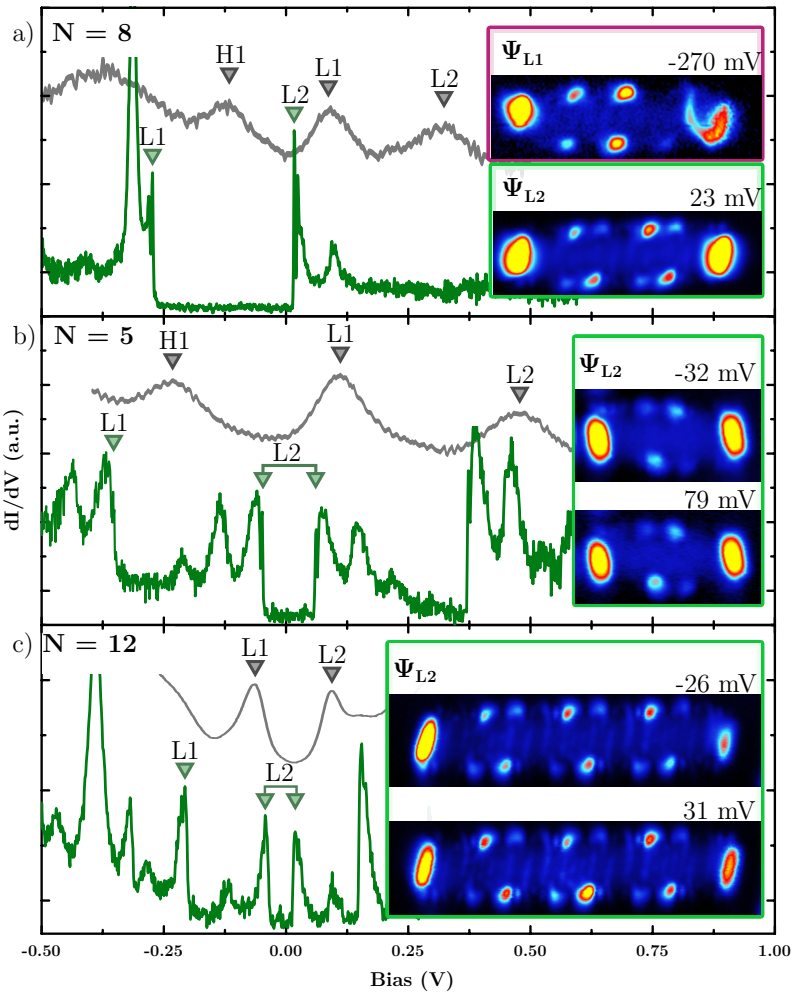

Figure 6.4: STS spectra and corresponding dI/dV maps recorded at Ψ_{L1} and Ψ_{L2} states energy of a N = 8 (a) N = 5 (b) and N = 12 (c) (3,1,8)-GNRs.

at 0.5 V shows bright protrusions that become two paired bright dots when the zone is imaged at low bias with atomic resolution (Figure 6.5b). This feature could be tentatively assigned to a divacancy negatively charged defect [151], although there are other candidate defects such us oxygen vacancies occupied by one or two electrons, which are not sufficiently well characterized in the literature [152]. For instance, another type of defect is shown in Figure 6.5d-f. Here the protruded appearance at 0.5 V turns into a missing atom in the atomically resolved image, which could be assigned to an individual oxygen vacancy. These point defects appear in the islands regardless of the growth parameters or post-annealing treatments of the samples, so it is of crucial importance to

study their effect on the electronic level alignment of ch-GNR/MgO_{ML}. Their common property is that they are charged defects, and thus, are prone to induce drastic variations in the local electric polarization of polar insulators like MgO [153].

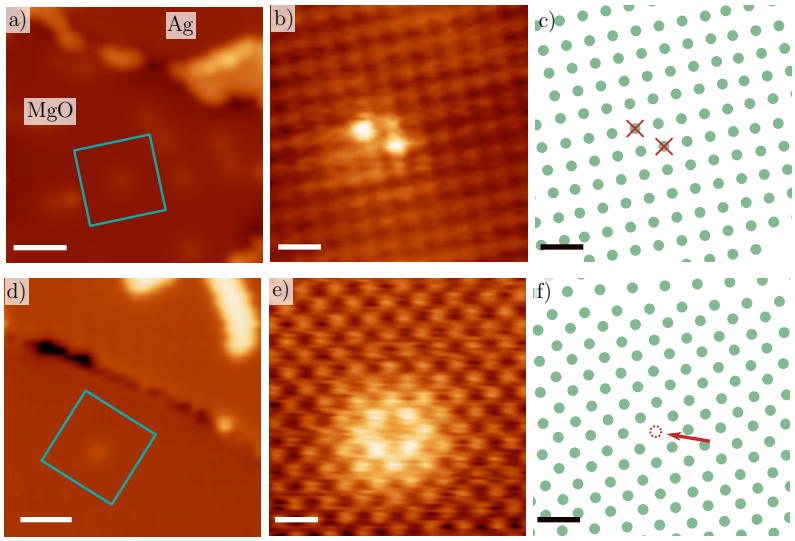

Figure 6.5: a) MgO_{ML} island with bright dots (0.5 V, 50 pA, scale bar 2 nm.) b) Zoom in the MgO_{ML} island shown in (a) with atomic resolution (-5 mV, 1 nA, scale bar 0.5 nm). c) Atomic scheme with green dots representing the visualized atoms in (b) and red crosses pointing out the position of the point defects (scale bar 0.5 nm). d) MgO_{ML} island with bright dot (0.5 V, 200 pA, scale bar 2 nm.). e) Zoom in the MgO_{ML} island shown in (d) with atomic resolution (2 mV, 5 nA, scale bar 0.5 nm). f) Atomic scheme with green dots representing the visualized atoms in (e) and red crosses pointing out the position of the point defects (scale bar 0.5 nm).

Variations in the tunneling current or the bias voltage used as set point are not expected to alter the peak energy of intrinsic states of GNRs. However, the total electric field contributed by the tip-sample gap voltage drop and the substrate's electric polarization, can tune the potential energy of the GNR's states, specially close to oxygen vacancies [153]. This is the origin of the gating effect observed in the (3,1,8)-GNRs adsorbed close to point defects. First we would like to settle the presence of charged defects. Bright elliptic rings centered in the defect have to appear in the GNR $\mathrm{d}I/\mathrm{d}V$ maps, since this is the archetypal signature of electronic charge/discharge of localized states [64]. The size of these rings, as well as their charging threshold bias voltage, can be tuned by changing the electrostatic tip induced potential (the electric field in a 1D model would follow eq. 2.11). This is confirmed in our test ribbons by

recording a series of dI/dV maps at various tip height distances, as shown in Figure 6.6 on a N = 12 (3,1,8)-GNR. While the central position of the elliptical contour that fits the charging ring remains constant, the area of the ellipses increases linearly with the logarithm of tunneling current set point that fixes the tip-sample distance before opening the feedback loop (Figure 6.6f-g). Since the current depends exponentially on the tip-sample distance, the fit in Figure 6.6g simply yields a linear dependence of the size of the charging ring with the z coordinate of the tip, as expected for a band bending effect near the point defect driven by the 1D electric field of eq. 2.11. The nanoscale termination of the tip apex is found to affect the shape of the charging rings, from oval ellipses to perfect circles, while the atomic scale resolution and topographic appearance of the ribbons retrieved with such tips are indistinguishable.

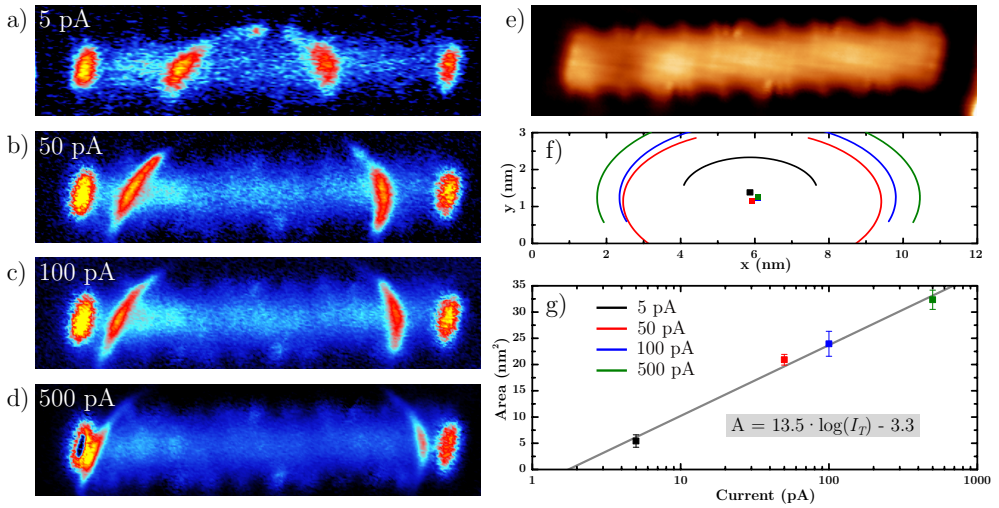

Figure 6.6: a-d) Series of constant height dI/dV maps recorded at 0.5 V with tunneling current set points from 5 to 500 pA at the time of feedback opening over the ribbon centre ($V_{mod} = 4mV$). e) In-gap constant height STM image of the N = 12 (3,1,8)-GNR shown in a-d (SP: -2.5 mV). f) Fits (lines) and centers (squares) of the ellipses extracted from the dI/dV maps. g) Area of the ellipses as a function of set point tunneling current.

The charge/discharge of the defect is a sharp transition between two electrostatic environments that cannot be gradually controlled. As a consequence, it prevents us from characterizing the GNR electronic structure in the two defect charge states, because the transition is extremely sensitive to the tip position and bias. In exchange, it allows uss to unambigously determine the presence and position of the defect. However, next to the point defects and at bias voltages well below the charging threshold, we can still probe the variation of

the MgO electric polarization caused by the presence of bound charges. When the electric polarization underneath the ribbon as a function of the probe point varies, the energy of the molecular states shifts accordingly as a function of the (x, y) coordinates. This effect was shown for a N = 12 (3,1,8)-GNR in Figure 5.10 in section 5.3.1, and it is further confirmed in several other GNRs near defects. Note that in the 1D model for the electric field as the one sketched in Figure 2.6, the tip lateral movement cannot change the electrostatic potential felt by the MgO layer. However, if we allow for finite (x, y) gradients in the tip electrostatic potential, we cannot discern between a tip induced variation of the MgO electric polarization or an intrinsic variation of the MgO as a function of the distance to the defect.

This local gating effect ought to manifest as well by tracking the evolution of molecular orbital as the ribbon is displaced with respect to the defect by atomic manipulation. Figure 6.7 shows the shift in energy of Ψ states of a N = 5 (3,1,8)-GNR by modifying its position in the island with respect to a nearby defect. The defect reported in Figure 6.5a-c is visualized here through a set of images of the charging ring at constant bias and different regulation currents. In Figures 6.7a-b we show these images recorded at two different positions to study the ring variation with the distance. The white squares in Figure 6.7c-d represent the average of the centers observed in the aforementioned data set, while the dotted green circles show the position where the point defect was observed in the atomically resolved image of the island (Figure 6.5a-c). The blue curves in Figures 6.7a-b represent the fits of the charging rings measured at the same regulation set point (0.5 V, 20 pA) in the two different GNR positions. Both rings have a common area of 4.43 ± 0.03 nm^2, which is in agreement with our assumption about the area dependency on the tip regulation distance (Figure 6.6). The STS spectra shown in Figure 6.7e are recorded on the same GNR position, but with the GNR located at different distances from the defect. A rigid shift in energy of 12 ± 4 mV is found for the SOMO and SUMO states (see section 6.2) when the GNR is moved 2.4 nm towards the defect, which points to a clear local gating of the GNRs in the presence of atomic scale defects in the MgO.

The same comes true for the type of defect analyzed in Figures 6.5d-f. When another N = 5 (3,1,8)-GNR is moved in the proximity of this defect its electronic characterization shows significant changes depending on the distance between them relative to the point defect. Figure 6.8 illustrates this issue. For this study, the GNR has been characterized on the MgO_{ML} island at two different positions. The STS spectra shown in Figure 6.8b are recorded at the same armchair edge of the GNR, and yet they show different features. At

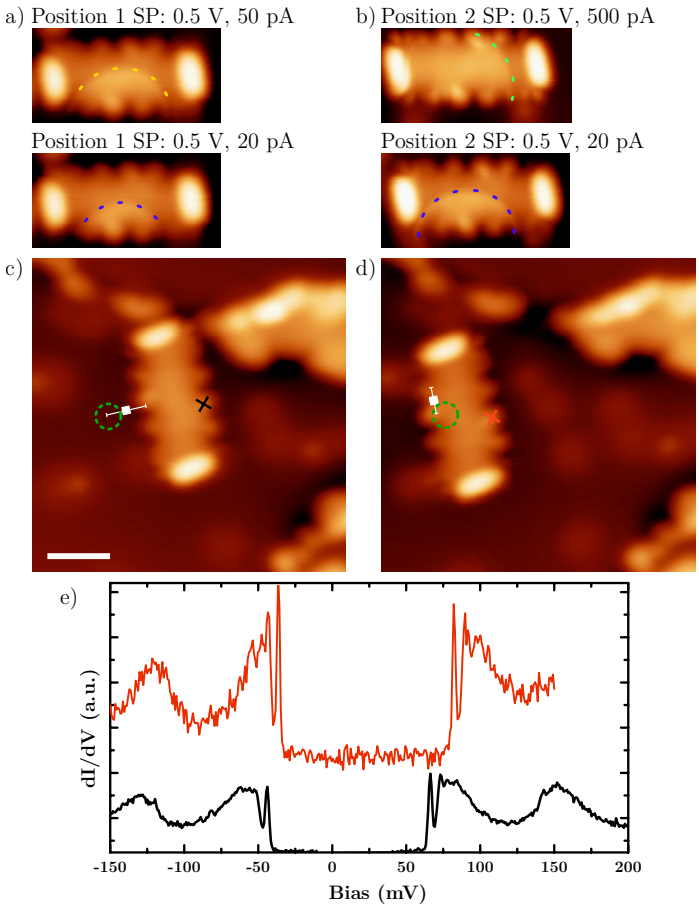

Figure 6.7: a-b) STM images of the charging ring at constant bias and different regulation currents, recorded on a N = 5 (3,1,8)-GNR in different positions. c-d) STM images of the N = 5 (3,1,8)-GNR on MgO at two position. The white squares represent the centers of rings observed in a set of images of the charging ring. The blue line is the fit of the ring in the images shown in (a) and (b) recorded at 0.5 V, 20 pA. The green dotted circle represents the position of the point defect observed in atomic resolution images (Figure 6.5. e) STS spectra recorded at the cross positions in a-b.

position 1, the STS spectrum shows the *L2* peak at 35 mV ($\Delta_{L12} = 270$ mV), and a feature at around -0.13 V. The peak width and shape of the latter correspond to a charging ring that crosses the GNR at position 1. Figure 6.8 also illustrates the enlargement of the elliptic ring as the recording bias decreases in absolute value from -360 to -290 mV, and how the wave function of *L1* state cannot be imaged because the electrostatic potential of the charged defect produces a strong gating effect in the states. However, moving the GNR

to the position 2, the charging feature does not appear in the STS spectrum within the energy range of interest. But, more importantly, we observe a rigid shift the observed molecular orbitals that amounts to 50 mV ± 3 mV. This shift, together with the absence of defect charging phenomena in the negative bias range, enables the recovery of the electronic features previously found in N = 5 (3,1,8)-GNR. Comparing the STS spectra of Figure 6.8b, we find that *L2* at position 2 is now split into two peaks that appear at both sides of the Fermi level. The energy distance between these peaks is 105 mV, which agrees perfectly with the Δ_s gap observed in another N = 5 (3,1,8)-GNR (see Figs. 6.4b or 6.7c). By moving the GNR away from the defect we have restored the splitting of the *L2* state in a SOMO and a SUMO.

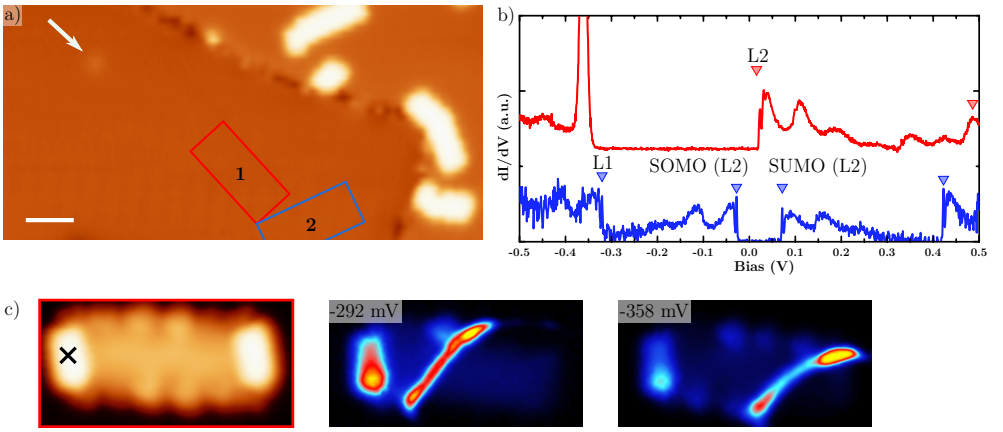

Figure 6.8: Induced spin splitting by atomic manipulation. a) STM image of a MgO_{ML} island. SP: 0.5 V, 200 pA. The red and blue squares represent the place of the N = 5 (3,1,8)-GNR that we named in the text position 1 and position 2 respectively. b) STS spectra recorded at the armchair edge of the GNR at position 1 (red) and at position 2 (blue). SP: 0.5 V, 200 pA, V_{mod} = 1 mV. c) STM topography image of the GNR located in position 1 and two constant height dI/dV maps recorded the bias specified in each map. SP: 0.5 V, 200 pA, Δz = -50 pm.

6.3.2 Tunable backgating using electric fields

STM-based techniques are frequently used to observe the effect of external electric fields on molecules, atoms or atom clusters. The electric fields existing at the tip-sample junction have been reported to produce molecular diffusion [154, 155] or induce electric polarization switching [60]. Here we report the viability ch-GNR/MgO_{ML}/Ag(001) system as a three terminal device where (3,1,8)-GNRs play the role of active element with electric conductance highly

sensitive to a gate voltage. Figure 6.9a shows an scheme of the STM junction during STS measurements in constant height mode. The tip and sample contacts are represented as the drain and the source terminals of the transistor, while the tip-sample distance acts as the gate electrode. In Figure 6.10a we include the STS spectra of a N = 12 (3,1,8)-GNR recorded for various tip-sample distances (z). The obtained energies of SOMO and SUMO states are represented as a function of Δz in Figure Figure 6.10b. Equivalent measurements on a N = 5 (3,1,8)-GNR are summarized in Figure 6.10c.

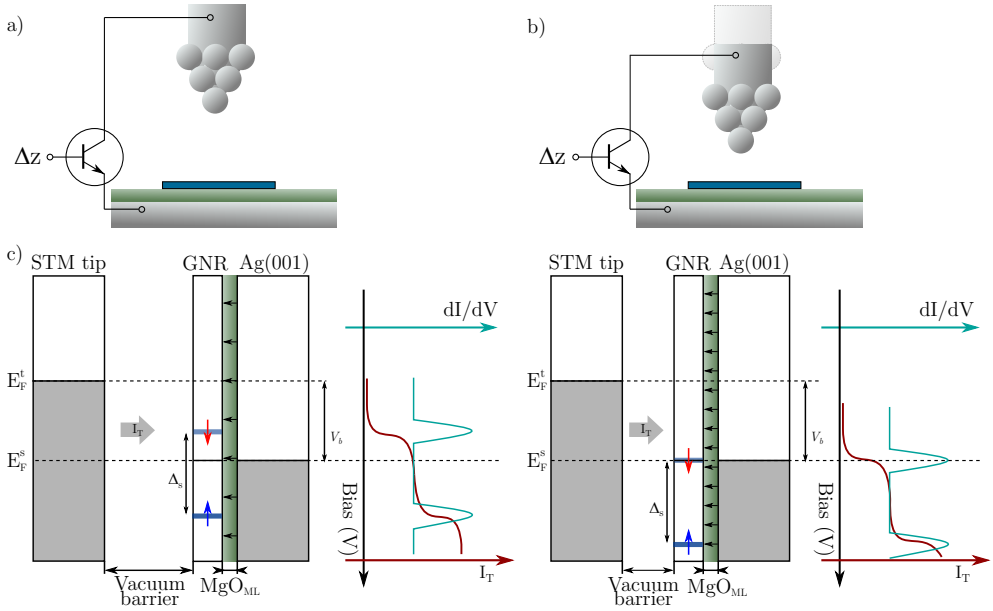

Figure 6.9: Scheme of the STM junction during STS measurements in constant height mode at z (a) and z - Δz (b). The gating when the tip is located closer (b) shifts the GNR states which produce the shift of the peaks in STS spectra. The energetic alignments between the STM tip, the GNR and the substrate are shown at the bottom with the resulted jumps in I-V and peaks in dI/dV curves.

A clear trend in the data is that the approach of the tip results in a shift of the Ψ states of the GNR determined by the value of z. This shift in energy is observed in the same direction at both sides of the Fermi level, regardless of the bias sign, with an average value of -50 meV/nm. For both GNRs lengths in Figure 6.10, the spin splitting (Δ_s) is conserved during the whole experiment, which corroborates the rigid energy shift of the GNR's molecular orbitals in response to an external electric field which is controlled by the width of the tip-sample gap.

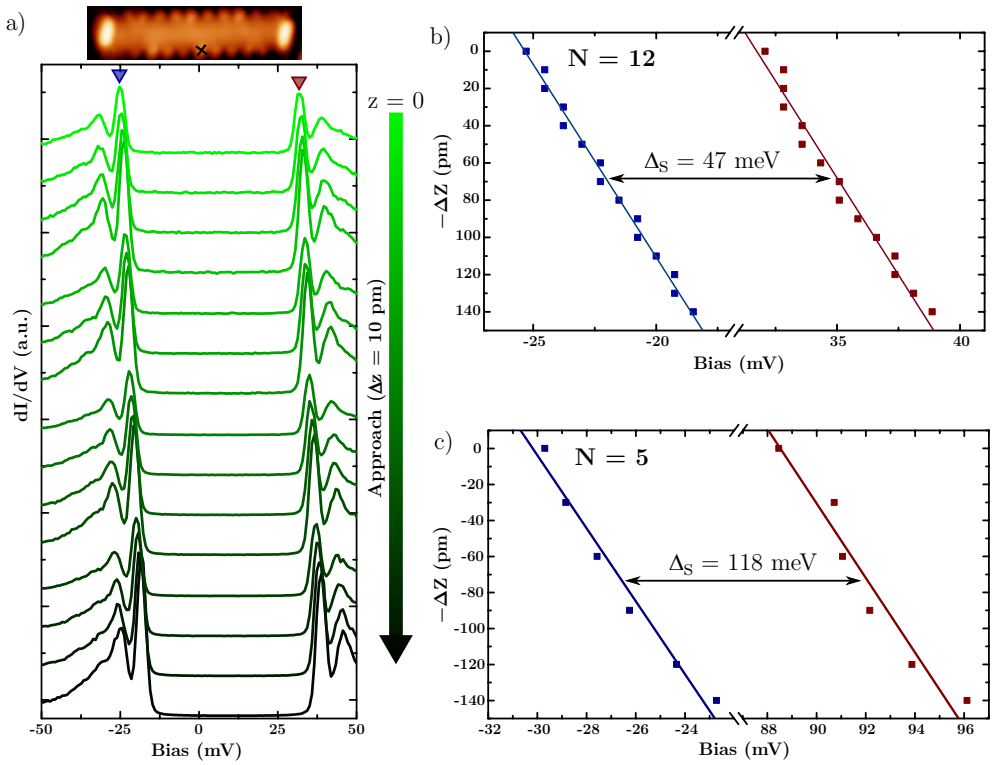

Figure 6.10: a) STS spectra recorded on a N = 12 (3,1,8)-GNR in constant height mode with different tip-sample distance at starting set point. STS SP: 0.5 V, z. All the STS spectra are recorded at the position of the cross shown in the STM image. b) Tip-sample distance as a function of found peak energies of SOMO (blue triangle in (a)) and SUMO (red triangle in (a)) states of N = 12 (3,1,8)-GNR. c) Tip-sample distance as a function of found peak energies of SOMO and SUMO states of N = 5 (3,1,8)-GNR in equivalent measurements to (a).

The effects of the presence of insulating layers between metallic substrates and molecules are commonly described with the double tunnel barrier model in the STM junction (vacuum gap and MgO_{ML}) [156]. However, the double tunnel barrier model predicts that the reduction of the vacuum barrier tunneling resistance ($\Delta z < 0$ variation) causes and energy shift to higher values for $V_{bias} > 0$ or lower values for $V_{bias} < 0$ (i.e., to higher absolute values of the bias in both cases). This is a major discrepancy with the observed behaviour in our system. Therefore, our data should be interpreted within a more realistic model than the double tunnel barrier.

Figure 6.9b shows an scheme of the proposed model to explain the tendency of the data shown in Figures 6.10c and 6.10d. The electrostatic potential

energy of the Ψ states is modified by a constant value (δU) that only depends on the size of the vacuum barrier (z). This shift in energy (δU) is quite small (5 mV/A), but the increase in lifetime of Ψ states due to the presence of the atomic layer of MgO gives us the chance to evaluate the effect of this electrostatic gating. U_e represents the variation of electrostatic energy of an electron tunneling across the MgO towards the tip (or viceversa). This energy is the work necessary to move the electron from the sample to the GNR and its value, depends on the thickness of the insulating MgO, since it is required to invest energy to travel through the tip-sample electric field. Furthermore, MgO is a polar insulator, and thus it is expected to exhibit an out of plane electric polarization (P_{MgO}) caused by the rumpling of Mg and O atoms on a surface [60]. P_{MgO} is schematically represented in Figure 6.9c with arrows from the Ag(001) to the GNR. Consequently, there will be another contribution to electrostatic energy due to the dipolar moments inside the MgO. It is this latter contribution to U_e the one which makes possible the gating effect by means of a virtual Δz knob. As Figure 6.9c shows, the electric polarization of the MgO change sin response to the electric field inside the vacuum gap, which in a first approximation depends inversely proportional to Δz (see eq. 2.11). This change in the electric polarization between two configurations with tip-sample distances induces a potential energy shift of the electron residing in the GNR's orbital of exactly ΔU_e. Considering the tendency in the experiments shown in Figure 6.10b and 6.10c, reducing the tip-sample distance by 0.4 additional nanometers, the Ψ_{L2} state would then be aligned with the substrate's Fermi level. This means that the previously proposed device (Figure 6.9a) would experience a sudden raise of the device conductance, presumably made up by fully spin polarized charge carriers (Figure 6.9b), which is the defining characteristic of ones occupying the SUMO state.

If only the sample bias applied in the STM junction determines the electrostatic energy, the sign of the electric field should be determined by the sign of the bias, and thus one would expect shifts in opposite directions for different bias polarities, just as it occurs in the double tunnel barrier case. And also, MgO can be considered as a linear isotropic dieletric whose electric polarization variation follows the sign of the electric field. However, in a STM junction the potential drop is not only contributed by the sample bias. There is always a contact potential difference (CPD) responsible for the chemical and charge contrast in many SPM applications. In order to explain our energy shift insensitivity to the bias sign, we should consider the total gap voltage drop in eq. 2.11 as the sum of the bias voltage plus the CPD. When CPD $> V_b$, the electric field variations as a function of z would be the same independently of the bias

sign, with an absolute value much smaller than the CPD value. Note that the CPD is not required in potential atomic scale spin polarized transistors, but in our case it gives us the chance to ascertain the origin of the energy shift to electrostatic gating effect, as opposed to the variable voltage drop expected in a double tunnel barrier model.

6.4 Conclusions

The interaction between localized unpaired electrons in open-shell graphene structures induces spontaneous magnetic order in the structure. Theoretical calculations that include electron-electron correlations, predict for (3,1,8)-GNRs a spin splitting of the edge states. In this chapter, we report experimental evidences of the spin splitting of localized LUMO states in (3,1,8)-GNRs and we evaluate the requirements to observe this effect.

To observe the spin splitting, two conditions are met. First, the electron doping ΔD_{MgO} of the substrate should shift an unoccupied orbital above the Fermi level. From the electronic characterization of GNRs with different lengths, we observed that ΔD_{MgO} to shift the *L2* state of N = 5 an N = 12 (3,1,8)-GNRs above the Fermi level, but for other lengths is not enough. For longer (N > 12) (3,1,8)-GNRs, we have estimated that the electron doping of the $\mathrm{MgO_{ML}}$ has a value of -265 meV from the neutral GNR states. The second requirement is that the energy of the shifted state (E_{L2} in our data) should be lower than the energy increase caused by a double occupancy of p_z states. This energy gap (Δ_s) is found to decrease as a function of the GNR's length, with values of 118 and 47 meV for N = 5 and N = 12 respectively.

Finally, we evaluated the energy shift of Ψ states due to the presence of point defects and by inducing an electric field at the STM junction. We demonstrate that both gating effects enable the adjustment of Ψ states with respect to the Fermi level, which reveals the potential of the ch-GNR/$\mathrm{MgO_{ML}}$/Ag(001) system as an atomic scale spin polarized transistor.

Chapter 7

Summary and conclusions

Electronics is always on the road to miniaturize existing electronic devices to improve their efficiency. However, semiconductor based integrated circuits are reaching their physical limit, and the manufacturing costs of reducing their size below 10 nm is nowadays unfeasible for companies. To overcome this limitation, other materials are currently being developed to fabricate equivalent electronic circuits with smaller dimensions. In this context, molecular electronics propose the use of the smallest components: functional molecules. Designing molecules with electronic functionalities is the key point to create devices at the nanoscale. The diversity of organic chemical structures together with the low manufacturing costs of the synthetic processes involved, are the main advantages of molecular electronics above silicon based circuits. On-surface synthesis (OSS) is a bottom-up manufacturing strategy based on the reaction of molecules to achieve a well-defined organic structure. The atomic precision of OSS allows to create functional organic molecules for molecular electronic devices. As this technique is based on linking precursor molecules, the design of the precursors determines the shape and composition of the final structures. The characterization of atomically precise structures, requires then, atomic resolution. Scanning probe microscopy techniques based on a physical probe to scan the surface and observe physical properties down to the atomic scale, are the most common microscopy techniques used to analyze OSS structures. In this thesis, we present the synthesis of organic structures designed to have different electronic functionalities, and their characterization by scanning tunneling microscopy and spectroscopy techniques. These characterization techniques allow us to study the suitability of the structures as key components in molecular electronic devices.

After a first introduction into electronic devices at the nanoscale and an overview of OSS as manufacturing technique, in **Chapter 1** we review the predicted electronic and magnetic properties of graphene based nanoribbon structures depending on the geometry of the edges and the width of the ribbon. Next, in **Chapter 2** we survey the principles of Scanning Tunneling Microscopy technique (SPM) focusing on the most relevant techniques employed in this thesis, such as scanning tunneling spectroscopy (STS) and atomic manipulation. A description of the experimental equipment employed and an overview of sample preparation methods in ultra-high vacuum environment are also included.

In **Chapter 3** we present the synthesis of manganese phthalocyanines (MnPc) on Ag(111) by OSS. The synthesized MnPc includes four diarylethylene moieties (DAE) in the phthalocyanine ring. The DAE moiety is an optically active group. When UV light is applied to a solution of a derivative that includes a DAE moiety, its structure changes from the open ring configuration to the closed ring configuration. On a surface, a couple of previous studies reveal that the switchability of DAE moieties is preserved, and that it can be directly induced and characterized by STM and STS techniques. As MnPc are known to have a robust and readable magnetic state by STS techniques, an organo-metallic complex including optically active groups and the Mn in its structure could work as a magneto-optical transducer. We have first studied by STS technique the fingerprint of the different branches observed on the MnPc. The assignment of a configuration to the observed branches has been corroborated by DFT calculations. Then, we have concluded that there is no coupling between the branch configurations in the phthalocyanine ring and the magnetic fingerprint of the metallic center (Kondo resonance). We propose corrective measures to reduce the strong interaction of the phthalocyanine ring with the substrate, which will promote the coupling. Finally, we have successfully induced reversible switches with the STM tip between the assigned open and closed configurations of DAE moiety.

The other organic structures synthesized by OSS studied in this thesis are graphene nanoribbons. When the graphene infinite sheet is limited by a pair of parallel edges, the 2D structure of the graphene turns into a 1D structure, and the electronic structure is then expected to be insulating, semiconducting or metallic depending on the edge geometry and the width of the ribbon.

In **Chapter 4** we present the synthesis of atomically precise chiral graphene nanoribbons (ch-GNRs) on Ag(001). The structures of the synthesized ch-GNRs contain identical edges and differ in the width. Combining STM and

STS techniques we have characterized both structures to study the evolution of the electronic structure of ch-GNRs depending on their width and length. We observe the predicted localization of electronic states at the edges of the GNRs and an alignment of ch-GNRs orbitals with respect to the substrate's Fermi level that facilitates the study of conduction band states (LUMOs). These detailed characterization of the LUMO states is not possible on other substrates whose work function values are higher than Ag(001) substrate. We have also characterized the ch-GNRs on top of MgO islands grown on the Ag(001) substrate.

In **Chapter 5** we demonstrate that a single atomic layer of MgO is effective to electronically decouple organic structures from the metallic substrate. We have developed an optimization of MgO/Ag(001) samples to obtain embedded MgO monolayer islands where the ch-GNRs can be placed on by lateral atomic manipulation. Finally, by STM and STS techniques we have characterized ch-GNRs of different lengths where we observe the effects of the presence of a MgO monoatomic layer between the ch-GNR and the supporting metal. We unambiguously demonstrate the electron doping to the organic structure and the unprecedented increment of the life-time of the intrinsic GNR molecular orbitals, which corroborate the viability of MgO monolayer as decoupling spacer for organic based electronics.

The magnetism in finite graphene structures emerges from the interactions among spins in singly occupied molecular orbitals. This occurs when the p_z electrons are not paired in equivalent π-bonds in the structure due to the presence of defects in the structure (absent or substitution of carbons) or when there is a sublattice imbalance in the structure. Local magnetic moments can also be induced by spin polarization of highly spatially localized low energy states. When the ch-GNRs are placed on MgO, their highly localized edge states experience an energy shift due to electron doping that can accommodate a spin splitting caused by electron-electron correlations in the frontier orbitals.

In **Chapter 6** we unveil the first experimental evidences of this exciting ground state in zig-zag longitudinal edges of nanographenes. We also study the electrostatic gating produced by the presence of local electric fields. Within this context, we investigate the gating produced due to the presence of point defects near the ch-GNR, and the gating produced with controlled variations of the distance between the tip and the sample, to evaluate the suitability of ch-GNR/MgO/Ag(001) system as a spin polarized transistor.

Resumen y conclusiones

La miniaturización de los dispositivos electrónicos ya existentes es la mejor forma para aumentar su eficacia. Sin embargo, los circuitos integrados basados en semiconductores han alcanzado ya su límite físico, ya que reducir su tamaño por debajo de 10 nm es económicamente inviable para las empresas. Para salvar esta limitación, se están desarrollando nuevos materiales para fabricar circuitos electrónicos equivalentes a los de la tecnología CMOS con dimensiones más reducidas. En ese contexto, la electrónica molecular propone el uso de los componentes más pequeños: moléculas funcionales. El diseño de moléculas con aplicaciones electrónicas es el punto clave para crear dispositivos en la nanoescala. La amplia variedad de estructuras químicas orgánicas, junto con los bajos costes que suponen los procesos de síntesis asociados, son las principales ventajas de la electrónica molecular frente a los circuitos basados en semiconductores. La síntesis en superficie (OSS) es una técnica de fabricación de tipo *bottom-up*, basada en la reacción entre moléculas para conseguir una estructura orgánica atómicamente precisa. La precisión atómica de la OSS permite crear moléculas orgánicas funcionales para dispositivos electrónicos moleculares. Como esta técnica se basa en la unión de moléculas precursoras, el diseño de estas moléculas determina la forma y la composición de la estructura final. La caracterización de estructuras atómicamente perfectas, requiere, por tanto, de resolución atómica. Las técnicas de microscopía de barrido basadas en una sonda física para escanear la superficie y observar propiedades físicas en la escala atómica, son las técnicas de microscopía más utilizadas para caracterizar las estructuras sintetizadas mediante OSS. En esta tesis, presentamos la síntesis y caracterización mediante técnicas de microscopía de efecto túnel (STM) de estructuras orgánicas diseñadas para tener distintas aplicaciones electrónicas. Estas técnicas de STM nos permiten evaluar la idoneidad de las estructuras como componentes clave en dispositivos electrónicos moleculares.

Tras una breve introducción a los dispositivos electrónicos en la nanoescala y una visión general de la OSS como técnica de fabricación, en el **Capítulo 1** exploramos las propiedades electrónicas y magnéticas predichas para nanoestructuras de grafeno con forma de tira (GNR) en función de la geometría de los bordes y la anchura de la tira. A continuación, en el **Capítulo 2** se repasan los principios de la microscopía de efecto túnel (STM) centrándonos en las técnicas más relevantes empleadas en esta tesis, como son la espectroscopía de efecto túnel (STS) y la manipulación atómica. También se incluye una descripción del equipo experimental empleado y una visión general de los métodos de preparación de muestras en entornos de ultra-alto vacío.

En el **Capítulo 3** presentamos la síntesis de ftalocianinas de manganeso (MnPc) sobre Ag(111) mediante OSS. La MnPc sintetizada incluye cuatro grupos diarileno (DAE) en el anillo de ftalocianina. El DAE es un grupo ópticamente activo. Cuando se aplica luz UV a una solución de un derivado que incluye el grupo DAE, su estructura cambia de una configuración de anillo abierto a una de anillo cerrado. En superficie, existen un par de estudios que revelan la conmutabilidad de los grupos DAE en la superficie, y que ésta puede inducirse y caracterizarse directamente mediante técnicas de STM y STS. Además, se sabe que las MnPc tienen un estado magnético robusto y legible por técnicas STS cuando están adsorbidas en la superficie. Por tanto, un complejo organometálico que incluya grupos ópticamente activos y Mn en su estructura podría funcionar como un transductor magneto-óptico. En primer lugar, hemos estudiado mediante STS las señales propias de las diferentes ramas observadas en la MnPc. La asignación de una configuración a los tipos de ramas observadas se ha corroborado mediante cálculos de DFT. A continuación, hemos concluido que no existe un acoplamiento entre las configuraciones de las ramas en el anillo de ftalocianina y la señal magnética del centro metálico (resonancia Kondo). Para solventarlo, proponemos reducir la interacción del anillo de ftalocianina con el sustrato, lo que favorecerá el acoplamiento entre los cambios estructurales y el estado magnético observable en el centro metálico. Por último, hemos inducido con éxito usando la punta del STM reacciones reversibles entre las configuraciones del grupo DAE asignadas como abierta y cerrada.

Las otras estructuras orgánicas sintetizadas mediante OSS estudiadas en esta tesis son las nanotiras de grafeno. Cuando la hoja infinita de grafeno se limita con dos bordes paralelos, la estructura bidimensional del grafeno se convierte en una estructura unidimensional, y la estructura electrónica resultante se espera que sea aislante, semiconductora o metálica en función de la geometría de los bordes y la anchura de la tira. En el **Capítulo 4** presentamos la sín-

tesis con precisión atómica de nanotiras de grafeno quirales (ch-GNRs) sobre Ag(001). Las estructuras de las ch-GNRs sintetizadas tienen bordes idénticos y difieren en su anchura. Combinando técnicas de STM y STS hemos caracterizado las nanotiras para estudiar la evolución de la estructura electrónica de las ch-GNRs en función de su anchura y longitud. Hemos observado la localización de estados electrónicos en los bordes de los GNRs predicha teóricamente, y una alineación de los orbitales de los ch-GNRs con respecto al nivel de Fermi del sustrato que facilita el estudio de los orbitales moleculares provenientes de la discretización de la banda de conducción (LUMOs). Esta caracterización detallada de los estados LUMOs no es posible en otros sustratos que tienen una función de trabajo con un valor superior a la de la Ag(001).

Las ch-GNRs también se han caracterizado sobre islas de MgO crecidas en Ag(001). En el **Capítulo 5** demostramos que una sola capa atómica de MgO es suficiente para desacoplar electrónicamente las estructuras orgánicas del sustrato metálico. Hemos optimizado la preparación de muestras MgO/Ag(001) para obtener islas monocapa de MgO incrustadas en la plata, sobre las que se pueden colocar los ch-GNRs mediante manipulación atómica lateral. Finalmente, mediante técnicas de STM y STS hemos caracterizado las ch-GNRs de diferentes longitudes. De esta forma hemos caracterizado los efectos asociados a la presencia de una monocapa de MgO entre la ch-GNR y el sustrato metálico. Además, demostramos sin género de dudas que se produce un dopaje de electrones hacia la estructura orgánica y un enorme incremento del tiempo de vida de los orbitales moleculares intrínsecos de la ch-GNR. Todo ello corrobora la viabilidad de una monocapa de MgO como espaciador aislante para desacoplar dispositivos electrónicos moleculares.

El magnetismo en las estructuras finitas de grafeno surge de la interacción de los espines en orbitales moleculares ocupados por un solo electrón. Esto se produce cuando los electrones p_z no están emparejados en enlaces π equivalentes en la estructura, bien debido a la presencia de defectos en la estructura (ausencia o sustitución de carbonos) o porque existe un desequilibrio entre las dos subredes dentro de la estructura. También puede aparecer un momento magnético local inducido por la polarización de espín de estados de baja energía muy localizados en el espacio. Cuando los ch-GNRs se colocan sobre islas de MgO, sus estados de borde, que están altamente localizados, modifican su energía debido al dopaje de electrones, haciendo al sistema compatible con un desdoblamiento de espín causado por las interacciones electrón-electrón. En el **Capítulo 6** mostramos la primera evidencia experimental de este interesante estado fundamental en los bordes longitudinales zig-zag de los nanografenos. También estudiamos el *gating* producido por la presencia de campos eléctricos

locales. En este contexto, hemos estudiado el *gating* producido por la presencia de defectos puntuales cerca del ch-GNR, así como el producido mediante variaciones controladas de la distancia punta-muestra, para evaluar la idoneidad del sistema ch-GNR/MgO/Ag(001) como transistor polarizado en espín.

Bibliography

(1) Lu, W.; Lee, Y.; Murdzek, J.; Gertsch, J.; Vardi, A.; Kong, L.; George, S. M.; del Alamo, J. A. In *2018 IEEE International Electron Devices Meeting (IEDM)*, 2018, pp 39.1.1–39.1.4.

(2) Jia, C. et al. *Science* **2016**, *352*, 1443–1445.

(3) Osorio, H. M.; Catarelli, S.; Cea, P.; Gluyas, J. B. G.; Hartl, F.; Higgins, S. J.; Leary, E.; Low, P. J.; Martín, S.; Nichols, R. J.; Tory, J.; Ulstrup, J.; Vezzoli, A.; Milan, D. C.; Zeng, Q. *Journal of the American Chemical Society* **2015**, *137*, 14319–14328.

(4) Perrin, M. L.; Galán, E.; Eelkema, R.; Thijssen, J. M.; Grozema, F.; Zant, H. S. J. v. d. *Nanoscale* **2016**, *8*, Publisher: The Royal Society of Chemistry, 8919–8923.

(5) Moreno, C.; Vilas-Varela, M.; Kretz, B.; Garcia-Lekue, A.; Costache, M. V.; Paradinas, M.; Panighel, M.; Ceballos, G.; Valenzuela, S. O.; Peña, D.; Mugarza, A. **2018**, 199–203.

(6) Lafferentz, L.; Ample, F.; Yu, H.; Hecht, S.; Joachim, C.; Grill, L. *Science* **2009**, *323*, Publisher: American Association for the Advancement of Science, 1193–1197.

(7) Shulaker, M. M.; Hills, G.; Patil, N.; Wei, H.; Chen, H.-Y.; Wong, H.-S. P.; Mitra, S. *Nature* **2013**, *501*, 526–530.

(8) Hills, G.; Lau, C.; Wright, A.; Fuller, S.; Bishop, M. D.; Srimani, T.; Kanhaiya, P.; Ho, R.; Amer, A.; Stein, Y.; Murphy, D.; Arvind; Chandrakasan, A.; Shulaker, M. M. *Nature* **2019**, *572*, 595–602.

(9) Grill, L.; Dyer, M.; Lafferentz, L.; Persson, M.; Peters, M. V.; Hecht, S. *Nature Nanotechnology* **2007**, *2*, 687–691.

(10) Hla, n.; Bartels, n.; Meyer, n.; Rieder, n. *Physical Review Letters* **2000**, *85*, 2777–2780.

(11) Clair, S.; de Oteyza, D. G. *Chemical Reviews* **2019**, *119*, 4717–4776.

(12) Hernández-López, L.; Piquero-Zulaica, I.; Downing, C. A.; Piantek, M.; Fujii, J.; Serrate, D.; Ortega, J. E.; Bartolomé, F.; Lobo-Checa, J. *Nanoscale* **2021**, 5216–5223.

(13) Cai, J.; Ruffieux, P.; Jaafar, R.; Bieri, M.; Braun, T.; Blankenburg, S.; Muoth, M.; Seitsonen, A. P.; Saleh, M.; Feng, X.; Müllen, K.; Fasel, R. *Nature* **2010**, *466*, 470–473.

(14) Nakada, K.; Fujita, M.; Dresselhaus, G.; Dresselhaus, M. S. *Physical Review B* **1996**, *54*, 17954–17961.

(15) Fujita, M.; Wakabayashi, K.; Nakada, K.; Kusakabe, K. *Journal of the Physical Society of Japan* **1996**, *65*, 1920–1923.

(16) Talirz, L.; Pignedoli, C. A. In *Handbook of Materials Modeling: Applications: Current and Emerging Materials*, Andreoni, W., Yip, S., Eds.; Springer International Publishing: Cham, 2020, pp 685–719.

(17) Wakabayashi, K.; Sasaki, K.-i.; Nakanishi, T.; Enoki, T. *Science and Technology of Advanced Materials* **2010**, *11*, 054504.

(18) Yazyev, O. V.; Capaz, R. B.; Louie, S. G. *Physical Review B* **2011**, *84*, 115406.

(19) Río, E. C.-d.; Lado, J. L.; Cherkez, V.; Mallet, P.; Veuillen, J.-Y.; Cuevas, J. C.; Gómez-Rodríguez, J. M.; Fernández-Rossier, J.; Brihuega, I. *Advanced Materials* **2021**, *33*, 2008113.

(20) Clar, V. E. *Zeitschrift für Chemie* **1973**, *13*, 200–200.

(21) Son, Y.-W.; Cohen, M. L.; Louie, S. G. *Physical Review Letters* **2006**, *97*, 216803.

(22) Carvalho, A. R.; Warnes, J. H.; Lewenkopf, C. H. *Physical Review B* **2014**, *89*, 245444.

(23) Ruffieux, P.; Wang, S.; Yang, B.; Sánchez-Sánchez, C.; Liu, J.; Dienel, T.; Talirz, L.; Shinde, P.; Pignedoli, C. A.; Passerone, D.; Dumslaff, T.; Feng, X.; Müllen, K.; Fasel, R. *Nature* **2016**, *531*, 489–492.

(24) Hubbard, J.; Flowers, B. H. *Proceedings of the Royal Society of London. Series A. Mathematical and Physical Sciences* **1963**, *276*, 238–257.

(25) Golor, M.; Wessel, S.; Schmidt, M. J. *Physical Review Letters* **2014**, *112*, 046601.

(26) Tao, C.; Jiao, L.; Yazyev, O. V.; Chen, Y.-C.; Feng, J.; Zhang, X.; Capaz, R. B.; Tour, J. M.; Zettl, A.; Louie, S. G.; Dai, H.; Crommie, M. F. *Nature Physics* **2011**, *7*, 616–620.

(27) Li, J.; Sanz, S.; Merino-Díez, N.; Vilas-Varela, M.; Garcia-Lekue, A.; Corso, M.; de Oteyza, D. G.; Frederiksen, T.; Peña, D.; Pascual, J. I. *Nature Communications* **2021**, *12*, 5538.

(28) Binnig, G.; Rohrer, H.; Gerber, C.; Weibel, E. *Physical Review Letters* **1982**, *49*, 57–61.

(29) Binnig, G.; Rohrer, H.; Gerber, C.; Weibel, E. *Physical Review Letters* **1983**, *50*, 120–123.

(30) Bardeen, J. *Physical Review Letters* **1961**, *6*, 57–59.

(31) Gottlieb, A. D.; Wesoloski, L. *Nanotechnology* **2006**, *17*, R57–R65.

(32) Tersoff, J.; Hamann, D. R. *Physical Review Letters* **1983**, *50*, 1998–2001.

(33) Tersoff, J.; Hamann, D. R. *Physical Review B* **1985**, *31*, 805–813.

(34) Chen, C. J., *Introduction to Scanning Tunneling Microscopy: Second Edition*; Monographs on the Physics and Chemistry of Materials; Oxford University Press: Oxford, 2007.

(35) Becker, R. S.; Golovchenko, J. A.; Swartzentruber, B. S. *Physical Review Letters* **1985**, *55*, 987–990.

(36) Eigler, D. M.; Schweizer, E. K. *Nature* **1990**, *344*, 524–526.

(37) Crommie, M. F.; Lutz, C. P.; Eigler, D. M. *Science* **1993**, *262*, 218–220.

(38) Slot, M. R.; Gardenier, T. S.; Jacobse, P. H.; van Miert, G. C. P.; Kempkes, S. N.; Zevenhuizen, S. J. M.; Smith, C. M.; Vanmaekelbergh, D.; Swart, I. *Nature Physics* **2017**, *13*, 672–676.

(39) Chen, W.; Jamneala, T.; Madhavan, V.; Crommie, M. F. *Physical Review B* **1999**, *60*, R8529–R8532.

(40) Moro-Lagares, M.; Korytár, R.; Piantek, M.; Robles, R.; Lorente, N.; Pascual, J. I.; Ibarra, M. R.; Serrate, D. *Nature Communications* **2019**, *10*, 2211.

(41) Morgenstern, K.; Lorente, N.; Rieder, K.-H. *physica status solidi (b)* **2013**, *250*, 1671–1751.

(42) Wolter, B.; Yoshida, Y.; Kubetzka, A.; Hla, S.-W.; von Bergmann, K.; Wiesendanger, R. *Physical Review Letters* **2012**, *109*, 116102.

(43) Meyer, G. *Review of Scientific Instruments* **1996**, *67*, 2960–2965.

(44) Neu, B.; Meyer, G.; Rieder, K.-H. *Modern Physics Letters B* **1995**, *09*, 963–969.

(45) Moresco, F.; Meyer, G.; Rieder, K.-H.; Tang, H.; Gourdon, A.; Joachim, C. *Applied Physics Letters* **2001**, *78*, 306–308.

(46) Gross, L.; Moresco, F.; Ruffieux, P.; Gourdon, A.; Joachim, C.; Rieder, K.-H. *Physical Review B* **2005**, *71*, 165428.

(47) Mielke, J.; Selvanathan, S.; Peters, M.; Schwarz, J.; Hecht, S.; Grill, L. *Journal of Physics: Condensed Matter* **2012**, *24*, 394013.

(48) Hla, S.-W.; Braun, K.-F.; Wassermann, B.; Rieder, K.-H. *Physical Review Letters* **2004**, *93*, 208302.

(49) Wigner, E.; Bardeen, J. *Physical Review* **1935**, *48*, 84–87.

(50) Lang, N. D.; Kohn, W. *Physical Review B* **1971**, *3*, 1215–1223.

(51) Leung, T. C.; Kao, C. L.; Su, W. S.; Feng, Y. J.; Chan, C. T. *Physical Review B* **2003**, *68*, 195408.

(52) Prada, S.; Martinez, U.; Pacchioni, G. *Physical Review B* **2008**, *78*, 235423.

(53) Jaouen, T.; Aebi, P.; Tricot, S.; Delhaye, G.; Lépine, B.; Sébilleau, D.; Jézéquel, G.; Schieffer, P. *Physical Review B* **2014**, *90*.

(54) Corso, M.; Menchón, R. E.; Piquero-Zulaica, I.; Vilas-Varela, M.; Ortega, J. E.; Peña, D.; Garcia-Lekue, A.; de Oteyza, D. G. *arXiv:2107.13276 [cond-mat]* **2021**.

(55) Greiner, M. T.; Helander, M. G.; Tang, W.-M.; Wang, Z.-B.; Qiu, J.; Lu, Z.-H. *Nature Materials* **2012**, *11*, 76–81.

(56) Hollerer, M.; Lüftner, D.; Hurdax, P.; Ules, T.; Soubatch, S.; Tautz, F. S.; Koller, G.; Puschnig, P.; Sterrer, M.; Ramsey, M. G. *ACS Nano* **2017**, *11*, 6252–6260.

(57) Fowler, R. H.; Nordheim, L. *Proceedings of the Royal Society of London. Series A, Containing Papers of a Mathematical and Physical Character* **1928**, *119*, 173–181.

(58) Bono, J.; Good, R. H. *Surface Science* **1987**, *188*, 153–163.

(59) Kolesnychenko, O. Y.; Kolesnichenko, Y. A.; Shklyarevskii, O. I.; van Kempen, H. *Physica B: Condensed Matter* **2000**, *291*, 246–255.

(60) Martinez-Castro, J.; Piantek, M.; Schubert, S.; Persson, M.; Serrate, D.; Hirjibehedin, C. F. *Nature Nanotechnology* **2018**, *13*, 19–23.

(61) Binnig, G.; Frank, K. H.; Fuchs, H.; Garcia, N.; Reihl, B.; Rohrer, H.; Salvan, F.; Williams, A. R. *Physical Review Letters* **1985**, *55*, 991–994.

(62) Stetsovych, O.; Mutombo, P.; Švec, M.; Šámal, M.; Nejedlý, J.; Císařová, I.; Vázquez, H.; Moro-Lagares, M.; Berger, J.; Vacek, J.; Stará, I. G.; Starý, I.; Jelínek, P. *Journal of the American Chemical Society* **2018**, *140*, 940–946.

(63) Gross, L.; Schuler, B.; Mohn, F.; Moll, N.; Pavliček, N.; Steurer, W.; Scivetti, I.; Kotsis, K.; Persson, M.; Meyer, G. *Physical Review B* **2014**, *90*, 155455.

(64) Song, C.-L.; Jiang, Y.-P.; Wang, Y.-L.; Li, Z.; Wang, L.; He, K.; Chen, X.; Ma, X.-C.; Xue, Q.-K. *Physical Review B* **2012**, *86*, 045441.

(65) Gross, L.; Mohn, F.; Liljeroth, P.; Repp, J.; Giessibl, F. J.; Meyer, G. *Science* **2009**, *324*, 1428–1431.

(66) Mohammed, M. S. G.; Colazzo, L.; Robles, R.; Dorel, R.; Echavarren, A. M.; Lorente, N.; de Oteyza, D. G. *Communications Physics* **2020**, *3*, 159.

(67) Zhang, L.; Miyamachi, T.; Tomanić, T.; Dehm, R.; Wulfhekel, W. *Review of Scientific Instruments* **2011**, *82*, 103702.

(68) Giessibl, F. J. *Applied Physics Letters* **2000**, *76*, 1470–1472.

(69) Repp, J.; Meyer, G.; Stojković, S. M.; Gourdon, A.; Joachim, C. *Physical Review Letters* **2005**, *94*, 026803.

(70) Kichin, G.; Weiss, C.; Wagner, C.; Tautz, F. S.; Temirov, R. *Journal of the American Chemical Society* **2011**, *133*, 16847–16851.

(71) Hapala, P.; Kichin, G.; Wagner, C.; Tautz, F. S.; Temirov, R.; Jelínek, P. *Physical Review B* **2014**, *90*, 085421.

(72) Chiang, C.-l.; Xu, C.; Han, Z.; Ho, W. *Science* **2014**, *344*, 885–888.

(73) Sun, Z.; Boneschanscher, M. P.; Swart, I.; Vanmaekelbergh, D.; Liljeroth, P. *Physical Review Letters* **2011**, *106*, 046104.

(74) Gross, L.; Mohn, F.; Moll, N.; Liljeroth, P.; Meyer, G. *Science* **2009**, *325*, 1110–1114.

(75) Kahn, O.; Martinez, C. J. *Science* **1998**, *279*, 44–48.

(76) Dediu, V. A.; Hueso, L. E.; Bergenti, I.; Taliani, C. *Nature Materials* **2009**, *8*, 707–716.

(77) Naber, W. J. M.; Faez, S.; van der Wiel, W. G. *arXiv:cond-mat/0703455* **2007**.

(78) Gottfried, J. M. *Surface Science Reports* **2015**, *70*, 259–379.

(79) Li, L.-L.; Diau, E. W.-G. *Chemical Society Reviews* **2012**, *42*, 291–304.

(80) Martínez-Díaz, M. V.; Torre, G. d. l.; Torres, T. *Chemical Communications* **2010**, *46*, 7090–7108.

(81) Walter, M. G.; Rudine, A. B.; Wamser, C. C. *Journal of Porphyrins and Phthalocyanines* **2010**, *14*, 759–792.

(82) Rakow, N. A.; Suslick, K. S. *Nature* **2000**, *406*, 710–713.

(83) Mochida, I.; Tsuji, K.; Suetsugu, K.; Fujitsu, H.; Takeshita, K. *The Journal of Physical Chemistry* **1980**, *84*, 3159–3162.

(84) Mochida, I.; Suetsugu, K.; Fujitsu, H.; Takeshita, K. *Journal of the Chemical Society, Chemical Communications* **1982**, 166–167.

(85) Sorokin, A. B. *Chemical Reviews* **2013**, *113*, 8152–8191.

(86) Gimzewski, J. K.; Jung, T. A.; Cuberes, M. T.; Schlittler, R. R. *Surface Science* **1997**, *386*, 101–114.

(87) Gao, L.; Ji, W.; Hu, Y. B.; Cheng, Z. H.; Deng, Z. T.; Liu, Q.; Jiang, N.; Lin, X.; Guo, W.; Du, S. X.; Hofer, W. A.; Xie, X. C.; Gao, H.-J. *Physical Review Letters* **2007**, *99*, 106402.

(88) Tsukahara, N.; Noto, K.-i.; Ohara, M.; Shiraki, S.; Takagi, N.; Takata, Y.; Miyawaki, J.; Taguchi, M.; Chainani, A.; Shin, S.; Kawai, M. *Physical Review Letters* **2009**, *102*, 167203.

(89) Franke, K. J.; Schulze, G.; Pascual, J. I. *Science* **2011**, *332*, 940–944.

(90) Kügel, J.; Karolak, M.; Krönlein, A.; Serrate, D.; Bode, M.; Sangiovanni, G. *npj Quantum Materials* **2018**, *3*, 53.

(91) Li, R.; Li, N.; Wang, H.; Weismann, A.; Zhang, Y.; Hou, S.; Wu, K.; Wang, Y. *Chemical Communications* **2018**, *54*, 9135–9138.

(92) Zhao, A. *Science* **2005**, *309*, 1542–1544.

(93) Stróecka, A.; Soriano, M.; Pascual, J. I.; Palacios, J. J. **2012**.

(94) Nacci, C.; Kanisawa, K.; Fölsch, S. *Journal of Physics: Condensed Matter* **2012**, *24*, 394004.

(95) Isvoranu, C.; Wang, B.; Ataman, E.; Schulte, K.; Knudsen, J.; Andersen, J. N.; Bocquet, M.-L.; Schnadt, J. *The Journal of Chemical Physics* **2011**, *134*, 114710.

(96) Wäckerlin, C.; Tarafder, K.; Girovsky, J.; Nowakowski, J.; Hählen, T.; Shchyrba, A.; Siewert, D.; Kleibert, A.; Nolting, F.; Oppeneer, P. M.; Jung, T. A.; Ballav, N. *Angewandte Chemie* **2013**, *125*, 4666–4669.

(97) Alemani, M.; Peters, M. V.; Hecht, S.; Rieder, K.-H.; Moresco, F.; Grill, L. *Journal of the American Chemical Society* **2006**, *128*, 14446–14447.

(98) Cai, L.; Cabassi, M. A.; Yoon, H.; Cabarcos, O. M.; McGuiness, C. L.; Flatt, A. K.; Allara, D. L.; Tour, J. M.; Mayer, T. S. *Nano Letters* **2005**, *5*, 2365–2372.

(99) Choi, B.-Y.; Kahng, S.-J.; Kim, S.; Kim, H.; Kim, H. W.; Song, Y. J.; Ihm, J.; Kuk, Y. *Physical Review Letters* **2006**, *96*, 156106.

(100) Liljeroth, P.; Repp, J.; Meyer, G. *Science (New York, N.Y.)* **2007**, *317*, 1203–1206.

(101) Katsonis, N.; Kudernac, T.; Walko, M.; van der Molen, S. J.; van Wees, B. J.; Feringa, B. L. *Advanced Materials* **2006**, *18*, 1397–1400.

(102) Snegir, S. V.; Yu, P.; Maurel, F.; Kapitanchuk, O. L.; Marchenko, A. A.; Lacaze, E. *Langmuir* **2014**, *30*, 13556–13563.

(103) Dela Cruz Calupitan, J. P.; Galangau, O.; Nakashima, T.; Kawai, T.; Rapenne, G. *ChemPlusChem* **2019**, *84*, 564–577.

(104) Nickel, F.; Bernien, M.; Herder, M.; Wrzalek, S.; Chittas, P.; Kraffert, K.; Arruda, L. M.; Kipgen, L.; Krüger, D.; Hecht, S.; Kuch, W. *Journal of Physics: Condensed Matter* **2017**, *29*, 374001.

(105) Fu, Y.-S.; Ji, S.-H.; Chen, X.; Ma, X.-C.; Wu, R.; Wang, C.-C.; Duan, W.-H.; Qiu, X.-H.; Sun, B.; Zhang, P.; Jia, J.-F.; Xue, Q.-K. *Physical Review Letters* **2007**, *99*, 256601.

(106) Liu, L.; Yang, K.; Jiang, Y.; Song, B.; Xiao, W.; Li, L.; Zhou, H.; Wang, Y.; Du, S.; Ouyang, M.; Hofer, W. A.; Castro Neto, A. H.; Gao, H.-J. *Scientific Reports* **2013**, *3*, 1210.

(107) Kügel, J.; Karolak, M.; Krönlein, A.; Senkpiel, J.; Hsu, P.-J.; Sangiovanni, G.; Bode, M. *Physical Review B* **2015**, *91*, 235130.

(108) Momma, K.; Izumi, F. *Journal of Applied Crystallography* **2008**, *41*, 653–658.

(109) Piantek, M.; Serrate, D.; Moro-Lagares, M.; Algarabel, P.; Pascual, J. I.; Ibarra, M. R. *The Journal of Physical Chemistry C* **2014**, *118*, 17895–17899.

(110) Koudia, M.; Abel, M. *Chemical Communications* **2014**, *50*, 8565–8567.

(111) Arunan, E.; Desiraju, G. R.; Klein, R. A.; Sadlej, J.; Scheiner, S.; Alkorta, I.; Clary, D. C.; Crabtree, R. H.; Dannenberg, J. J.; Hobza, P.; Kjaergaard, H. G.; Legon, A. C.; Mennucci, B.; Nesbitt, D. J. *Pure and Applied Chemistry* **2011**, *83*, 1637–1641.

(112) Reecht, G.; Lotze, C.; Sysoiev, D.; Huhn, T.; Franke, K. J. *ACS Nano* **2016**, *10*, 10555–10562.

(113) Reecht, G.; Lotze, C.; Sysoiev, D.; Huhn, T.; Franke, K. J. *Journal of Physics: Condensed Matter* **2017**, *29*, 294001.

(114) Chen, Y.-C.; de Oteyza, D. G.; Pedramrazi, Z.; Chen, C.; Fischer, F. R.; Crommie, M. F. *ACS Nano* **2013**, *7*, 6123–6128.

(115) Carbonell-Sanromà, E.; Brandimarte, P.; Balog, R.; Corso, M.; Kawai, S.; Garcia-Lekue, A.; Saito, S.; Yamaguchi, S.; Meyer, E.; Sánchez-Portal, D.; Pascual, J. I. *Nano Letters* **2017**, *17*, 50–56.

(116) Huang, H.; Wei, D.; Sun, J.; Wong, S. L.; Feng, Y. P.; Neto, A. H. C.; Wee, A. T. S. *Scientific Reports* **2012**, *2*, 983.

(117) Deniz, O.; Sánchez-Sánchez, C.; Dumslaff, T.; Feng, X.; Narita, A.; Müllen, K.; Kharche, N.; Meunier, V.; Fasel, R.; Ruffieux, P. *Nano Letters* **2017**, *17*, 2197–2203.

(118) Ruffieux, P.; Cai, J.; Plumb, N. C.; Patthey, L.; Prezzi, D.; Ferretti, A.; Molinari, E.; Feng, X.; Müllen, K.; Pignedoli, C. A.; Fasel, R. *ACS Nano* **2012**, *6*, 6930–6935.

(119) Talirz, L.; Ruffieux, P.; Fasel, R. *Advanced Materials* **2016**, *28*, 6222–6231.

(120) Basagni, A.; Sedona, F.; Pignedoli, C. A.; Cattelan, M.; Nicolas, L.; Casarin, M.; Sambi, M. *Journal of the American Chemical Society* **2015**, *137*, 1802–1808.

(121) Sun, K.; Ji, P.; Zhang, J.; Wang, J.; Li, X.; Xu, X.; Zhang, H.; Chi, L. *Small* **2019**, *15*, 1804526.

(122) Wang, S.; Talirz, L.; Pignedoli, C. A.; Feng, X.; Müllen, K.; Fasel, R.; Ruffieux, P. *Nature Communications* **2016**, *7*, 11507.

(123) De Oteyza, D. G.; García-Lekue, A.; Vilas-Varela, M.; Merino-Díez, N.; Carbonell-Sanromà, E.; Corso, M.; Vasseur, G.; Rogero, C.; Guitián, E.; Pascual, J. I.; Ortega, J. E.; Wakayama, Y.; Peña, D. *ACS Nano* **2016**, *10*, 9000–9008.

(124) Sánchez-Sánchez, C.; Dienel, T.; Deniz, O.; Ruffieux, P.; Berger, R.; Feng, X.; Müllen, K.; Fasel, R. *ACS Nano* **2016**, *10*, 8006–8011.

(125) Schulz, F.; Jacobse, P. H.; Canova, F. F.; van der Lit, J.; Gao, D. Z.; van den Hoogenband, A.; Han, P.; Klein Gebbink, R. J.; Moret, M.-E.; Joensuu, P. M.; Swart, I.; Liljeroth, P. *The Journal of Physical Chemistry C* **2017**, *121*, 2896–2904.

(126) Jacobse, P. H.; Mangnus, M. J. J.; Zevenhuizen, S. J. M.; Swart, I. *ACS Nano* **2018**, *12*, 7048–7056.

(127) Han, P.; Akagi, K.; Federici Canova, F.; Mutoh, H.; Shiraki, S.; Iwaya, K.; Weiss, P. S.; Asao, N.; Hitosugi, T. *ACS Nano* **2014**, *8*, 9181–9187.

(128) Merino-Díez, N.; Li, J.; Garcia-Lekue, A.; Vasseur, G.; Vilas-Varela, M.; Carbonell-Sanromà, E.; Corso, M.; Ortega, J. E.; Peña, D.; Pascual, J. I.; de Oteyza, D. G. *The Journal of Physical Chemistry Letters* **2018**, *9*, 25–30.

(129) Jiang, Z.; Song, Y. *Physica B: Condensed Matter* **2015**, *464*, 61–67.

(130) Suda, S.; Oshiyama, A. *Journal of the Physical Society of Japan* **2015**, *84*, 024704.

(131) Wakabayashi, K.; Takane, Y.; Yamamoto, M.; Sigrist, M. *Carbon* **2009**, *47*, 124–137.

(132) Chen, Y.-C.; Cao, T.; Chen, C.; Pedramrazi, Z.; Haberer, D.; de Oteyza, D. G.; Fischer, F. R.; Louie, S. G.; Crommie, M. F. *Nature Nanotechnology* **2015**, *10*, 156–160.

(133) Wollschläger, J.; Erdös, D.; Schröder, K. .-M. *Surface Science* **1998**, *402-404*, 272–276.

(134) Wollschl, J.; Viernow, J.; Tegenkamp, C.; Erdo, D.; fu, I. **1999**, 6.

(135) Altieri, S.; Tjeng, L. H.; Sawatzky, G. A. *Physical Review B* **2000**, *61*, 16948–16955.

(136) Baumann, S.; Rau, I. G.; Loth, S.; Lutz, C. P.; Heinrich, A. J. *ACS Nano* **2014**, *8*, 1739–1744.

(137) Schintke, S.; Messerli, S.; Pivetta, M.; Patthey, F.; Libioulle, L.; Stengel, M.; De Vita, A.; Schneider, W.-D. *Physical Review Letters* **2001**, *87*, 276801.

(138) Tosoni, S.; Pacchioni, G. *The Journal of Physical Chemistry C* **2020**, 20960–20973.

(139) Giordano, L.; Baistrocchi, M.; Pacchioni, G. *Physical Review B* **2005**, *72*, 115403.

(140) Starodub, E.; Bartelt, N. C.; McCarty, K. F. *The Journal of Physical Chemistry C* **2010**, *114*, 5134–5140.

(141) Grånäs, E.; Knudsen, J.; Schröder, U. A.; Gerber, T.; Busse, C.; Arman, M. A.; Schulte, K.; Andersen, J. N.; Michely, T. *ACS Nano* **2012**, *6*, 9951–9963.

(142) Varykhalov, A.; Sánchez-Barriga, J.; Shikin, A. M.; Biswas, C.; Vescovo, E.; Rybkin, A.; Marchenko, D.; Rader, O. *Physical Review Letters* **2008**, *101*, 157601.

(143) Berdonces-Layunta, A.; Lawrence, J.; Edalatmanesh, S.; Castro-Esteban, J.; Wang, T.; Mohammed, M. S. G.; Colazzo, L.; Peña, D.; Jelínek, P.; de Oteyza, D. G. *ACS Nano* **2021**, *15*, 5610–5617.

(144) Reecht, G.; Krane, N.; Lotze, C.; Zhang, L.; Briseno, A. L.; Franke, K. J. *Physical Review Letters* **2020**, *124*, 116804.

(145) Van der Lit, J.; Boneschanscher, M. P.; Vanmaekelbergh, D.; Ijäs, M.; Uppstu, A.; Ervasti, M.; Harju, A.; Liljeroth, P.; Swart, I. *Nature Communications* **2013**, *4*, 2023.

(146) Martinez-Castro, J.; Bolat, R.; Fan, Q.; Werner, S.; Arefi, H. H.; Esat, T.; Sundermeyer, J.; Wagner, C.; Gottfried, J. M.; Temirov, R.; Ternes, M.; Tautz, F. S. *arXiv:2110.11449 [cond-mat]* **2021**.

(147) Lieb, E. H. *Physical Review Letters* **1989**, *62*, 1201–1204.

(148) Fernández-Rossier, J.; Palacios, J. J. *Physical Review Letters* **2007**, *99*, 177204.

(149) Mishra, S.; Beyer, D.; Eimre, K.; Liu, J.; Berger, R.; Gröning, O.; Pignedoli, C. A.; Müllen, K.; Fasel, R.; Feng, X.; Ruffieux, P. *Journal of the American Chemical Society* **2019**, *141*, 10621–10625.

(150) Mishra, S.; Beyer, D.; Eimre, K.; Kezilebieke, S.; Berger, R.; Gröning, O.; Pignedoli, C. A.; Müllen, K.; Liljeroth, P.; Ruffieux, P.; Feng, X.; Fasel, R. *Nature Nanotechnology* **2020**, *15*, 22–28.

(151) König, T.; Simon, G. H.; Rust, H.-P.; Pacchioni, G.; Heyde, M.; Freund, H.-J. *Journal of the American Chemical Society* **2009**, *131*, Publisher: American Chemical Society, 17544–17545.

(152) Sterrer, M.; Heyde, M.; Novicki, M.; Nilius, N.; Risse, T.; Rust, H.-P.; Pacchioni, G.; Freund, H.-J. *The Journal of Physical Chemistry B* **2006**, *110*, 46–49.

(153) Ferrari, A. M.; Casassa, S.; Pisani, C. *Physical Review B* **2005**, *71*.

(154) Serrate, D.; Moro-Lagares, M.; Piantek, M.; Pascual, J. I.; Ibarra, M. R. *The Journal of Physical Chemistry C* **2014**, *118*, 5827–5832.

(155) Akimov, A. V.; Kolomeisky, A. B. *The Journal of Physical Chemistry C* **2012**, *116*, 22595–22601.

(156) Warner, B.; El Hallak, F.; Prüser, H.; Sharp, J.; Persson, M.; Fisher, A. J.; Hirjibehedin, C. F. *Nature Nanotechnology* **2015**, *10*, 259–263.